University of Louisville

ThinkIR: The University of Louisville's Institutional Repository

Electronic Theses and Dissertations

5-2023

Drop impact on dry and liquid infused substrates with micro-wells.

Ahmed Nazrul Islam
University of Louisville

Follow this and additional works at: https://ir.library.louisville.edu/etd

Part of the Mechanical Engineering Commons

Recommended Citation

Nazrul Islam, Ahmed, "Drop impact on dry and liquid infused substrates with micro-wells." (2023). *Electronic Theses and Dissertations.* Paper 4045.
https://doi.org/10.18297/etd/4045

DROP IMPACT ON DRY AND LIQUID INFUSED SUBSTRATES WITH MICRO-WELLS

By

Ahmed Nazrul Islam

A Dissertation

Submitted to the Faculty of the

J.B. Speed School of Engineering of the University of Louisville

in Partial Fulfillment of the Requirements

for the Degree of

Doctor of Philosophy

in Mechanical Engineering

Department of Mechanical Engineering

University of Louisville

Louisville, Kentucky

May, 2023

DROP IMPACT ON DRY AND LIQUID INFUSED SUBSTRATES WITH
MICRO-WELLS

By

Ahmed Nazrul Islam

Dissertation approved on

April 13, 2023

by the following Dissertation Committee:

Dissertation Director
Dr. Yongsheng Lian

Dr. Bikram Bhatia

Dr. Robert Cohn

Dr. Stuart Williams

DEDICATION

To my father Mohammed Nazrul Islam and mother Salina Begum, whose endless love and support have guided me through every step of this journey, I dedicate this dissertation to you. Your unwavering belief in my abilities and constant encouragement have been my motivation to persevere through challenges and never give up. To my sisters Hima, Heeba and Shyma, thank you for your love and support, which have been invaluable to me. To my wife Fariha Nasme, your patience, understanding, and support have been my anchor throughout this challenging journey. Your love and dedication have been my source of strength, and I cannot thank you enough. I would also like to sincerely remember and honor the memory of my late father-in-law for his inspirations, and my mother-in-law for her ongoing love and support. Lastly, my sons Idrees Ahmed and Ismaeel Ahmed, every moment of this journey has been for you, and you are the light of my life. I am deeply grateful for all of your love and support in this journey.

ACKNOWLEDGEMENT

ABSTRACT

DROP IMPACT ON DRY AND LIQUID INFUSED SUBSTRATES WITH MICRO-WELLS

Ahmed Nazrul Islam

April 13, 2023

Drop impact on different types of surfaces are important physical concepts that are routinely found in day-to-day life and such studies have immense application for various types of industries. One such important application of drop dynamics is in the field of aviation science which is concerned of very large freezing drizzle drops impacting on airplane wings. Such drops are known as supercooled large droplets (SLD), and they pose a great risk and have been long known to have caused notable accidents in the past. SLDs are liquid drops that can remain in the state of liquid phase and grow into ice after an impact onto a solid body. Sometimes such freezing drizzle can splash and break into multiple daughter or satellite drops, and sometimes they can bounce off the substrate on which the impingement occurs. Due to the importance in aviation safety, researchers over the past decade has studied SLDs, but most of the studies are experimental studies which produced empirical relationship and little numerical simulation that can effectively vary and optimize drop impingement parameters.

In this study, numerical simulation is used to study the dynamics of water drops impacting on various types of substrates. The numerical simulation uses a very sharp interface reconstruction method known as moment-of-fluid method. At the interface between the solid-liquid and liquid-gas, lubricant-gas and lubricant-liquid, adaptive mesh refinement is used to correctly capture the moving interface curvatures and directions. To understand the importance of the underneath substrate surface, drop coalescence study has been done to show that merging drops can benefit from surface energy reduction to propel drops with higher kinetic energy, and the degree of curvature greatly affects the propelling behavior. For dry surface comparison, a drop impacting on a large micro-well cavity is studied and compared to a flat substrate. At different contact angles, and impact velocities, it has been shown that for certain range of speeds and wettability, the drops can only rebound from the micro-well cavity but not from the flat substrate. There has been found a notable difference in kinetic energy, spreading area, and wetting area ratios between the two cases. For the third study, a micro-well substrate is filled with lubricant, and drop impact cases at different velocities is studied. In this study we found that cloaking occurs when both lubricant and water interfacial tensions and impact speeds are low. Furthermore, we have observed that the thickness of the encapsulating lubricant layer changes over time. At moderate impact speeds, the lubricant layer is displaced, generating a lubricant-water jet, as we have demonstrated. However, at high impact speeds, a secondary impingement occurs, displacing a significant amount of lubricant and exposing the underlying substrate, which was not visible at lower impact speeds. Additionally, we conducted simulation on micro-wells infused with lubricant and observed that small spacing between the micro-well walls can limit lubricant drainage and displacement. The use of micro-wells also resulted in less

splashing compared to substrates without micro-wells. Finally, we confirmed that micro-wells are more effective at preserving lubricant than substrates without micro-wells.

TABLE OF CONTENTS

LIST OF FIGURES

LIST OF TABLES

CHAPTER I

GENERAL INTRODUCTION

Water droplet repellency has gained a lot of interest in recent decades due to the emerging needs in various engineering and scientific applications such as spray cooling[1], heat transfer enhancement [2, 3], self-cleaning and anti-corrosion treatments [4-6], inkjet printing[7, 8], etc. While much research has been undertaken to study the drop impingement phenomena at various impact speeds and environmental conditions, critical understanding of bounce-off, splashing and impalement on different types of substrates occurring in the harsh winter for the aviation applications is still very much required. Because of the nature of in-flight icing that involves large freezing droplets approaching at very high speeds, there is a growing need of water droplet repellency study in the field of aviation safety. The large freezing drops, known as supercooled large droplets or SLDs, are typically larger than 40μm and could also form in sizes that are more than 100 times larger than cloud droplets. Unlike cloud droplets, the impingement of SLDs on aircraft surfaces causes breakup into smaller satellite or daughter droplets, bounce/slide off from initial impact position known as rivulet flow and partial freezing that eventually transforms into glaze ice[9-11]. Growth of ice, through means of crystallization of freezing drizzles like SLDs, leads to severe aerodynamics performance losses[12]. There are reports of downwash of SLDs that causes wing flap deflection, causing significant decrease in lift, and increase in stall angle of attack[13], premature stall, increase in drag, loss in lift and

change in pitching moment[14]. Ice accretion and growth due to SLD impact cannot be easily avoided with conventional thermal powered anti-icing system because ridge ice and runback at the back of anti-ice region in long flight times cannot be easily avoided[9, 15-17]. And thus, SLDs are the most hazardous issue for aircrafts flying in winter conditions and have resulted in many aviation accidents to date[9, 14, 18-21]. Many numerical researchers have identified and noted similar observations regarding SLDs which, because of the size in contrast to small droplets, have deformations, ruptures from drop-wall impact that are quite different in nature. The collision event of SLDs produces drops that may partially adhere or partially splash or bounce off from the surface. Others have pointed out that, due to such complexities, wind tunnel research lacks the design and are not sufficient in SLD icing and are therefore highly dependent on numerical simulations[19]. Therefore, this pose difficulty and limitations in existing SLD icing studies, where only empirical corrections based on conventional water droplet models are utilized[19, 20].

While large drops, such like SLDs, have wide range of impact velocity, viscosity, density, and temperature as critical factors that dictates the physical aspects like deformation, receding breakup, partial to full rebound, the lamella formation, etc., the surface structure and morphology on which the drop impact event occurs does also control different variables of droplet mobility. Such drop dynamics could result in complex behaviors like oscillation velocity, kinetic energy, spreading ratio, contact time, and wetting area and are highly dependent on surface features. Therefore, to study such substrates, numerous experimental and numerical studies have considered surfaces that have various types of roughness features. The key in producing water-repellent and anti-wetting substrate is to entrap an immiscible phase material other than the water, such like air or a secondary

liquid, such like a lubricant or oil, within this roughness feature. The immiscible phase material should provide a barrier between the liquid phase (i.e. the water droplet) and the impinging surface, thus becoming an important factor since icing conditions can be avoided on surfaces that have protective layer thwarting the SLDs from recalescence and freezing. To design such surfaces that have roughness to trap air pockets, experimentalists and researchers have come up with designs like micro-pillars, mushrooms[22, 23], ridges[24], hierarchical micro-nano-structures[25], etc.
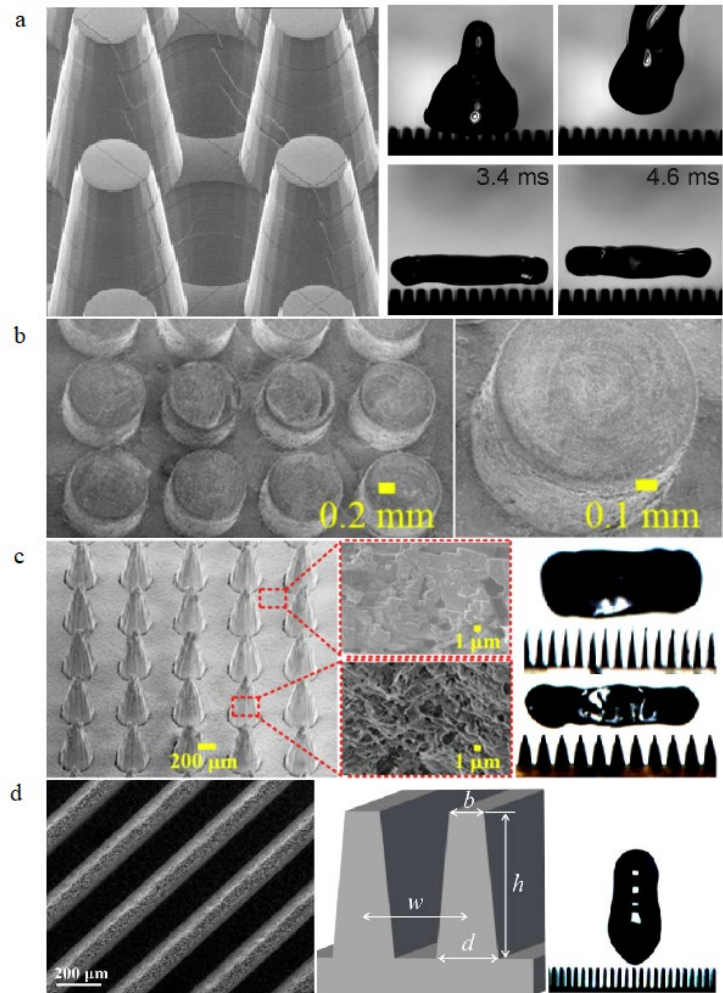
Figure 1: Experimental Studies of Various Surface Structures: a) macro-texture surface with protruding and indenting surface features and droplet bounce off [26] b) Pillar Arrays [27] c) Conical Pillar [28] d) Ridges and bounce off [29]

Such designs of roughness can entrap air pockets, and therefore are of great interest for water repellent superhydrophobic applications. For the anti-icing strategy, superhydrophobic surfaces have long been studied and debated. Many studies have argued favorably for the use of superhydrophobic substrates for anti-icing applications, where many have argued that ice and textured surface can mechanically interlock and thus such surface properties to reduce the ice growth are easily compromised[30, 31]. Some said that the ice-adhesion strength reduces, and frost growth are delayed over the roughness features that are entrapping the air [32-35] while others said the frost nucleation and growth within the rough structures such like micro-posts, enhances ice adhesion by means of higher interfacial bonding strength [36, 37].

Another important design that has gained a lot of interest in recent years for anti-icing strategy and mitigation is to incorporate the liquid-infused surfaces that would act as deterrent to ice-nucleation, adhesion and inter-locking and prolonged accretion. In academic and industrial settings, such surfaces, commonly termed as SLIP (slippery liquid infused porous surfaces) or LIS (lubricant infused surfaces), have been long studied for condensation[38, 39], bio-fouling[40, 41], self-cleaning applications[42-44], and many other applications. And in the sense of aviation icing problem, which occurs when supercooled large droplets (SLDs) impact on the aircrafts body and starts to augment into a crystalline form while thickening and eventually accreting into ice form, water wettability and ice accretion have common surface energy characteristics and thus characteristics of superhydrophobic structures are also applicable in designing ice-phobic structures[45-47]. Therefore, anti-icing strategists have ventured into using lubricant infused substrate instead of air-pockets of superhydrophobic substrates, to show that such lubricants can provide

thermal/mechanical barrier between droplets at very cold temperature and the surfaces on which the drops are residing and that ice-accretion could therefore be slowed [36, 38, 48, 49]. Our study is to focus on pre-icing condition and to delay the stage of SLDs turning into ice-accretion. Very few studies have taken proper numerical simulation technique to understand the jump-off, and breakup of supercooled large droplets on different substrates[50, 51]. For our part of the study, we use a novel Moment-of-Fluid (MOF) algorithm coupled with adaptive mesh refinement to study the impingement of the drops on dry and lubricant impregnated substrate. To study such behavior, we at first understand the implication of a curved surface and study the process of drop coalescence and the catapulting of merged drops to analyze how surface energy can transform into directional kinetic energy in propelling water droplets. Secondly, we present a study of a drop impact on a micro-well structure that properly entraps air to reduce liquid-solid contact. The micro-well structure enhances drop repelling capability due to its non-wetting feature. Thirdly, we incorporate lubricant impregnated micro-well structure, to understand the behavior of the drop mobility upon impact at various speeds. Two critical phenomena of the SLIP/LIS substrate are studied, namely cloaking and formation of wetting ridge and surface tensions are varied to understand the implication of interfacial tensions on the drop mobility. We also explore the high speed impact cases for drops impact on micro-wells with varying pitch holding the different types of lubricants.
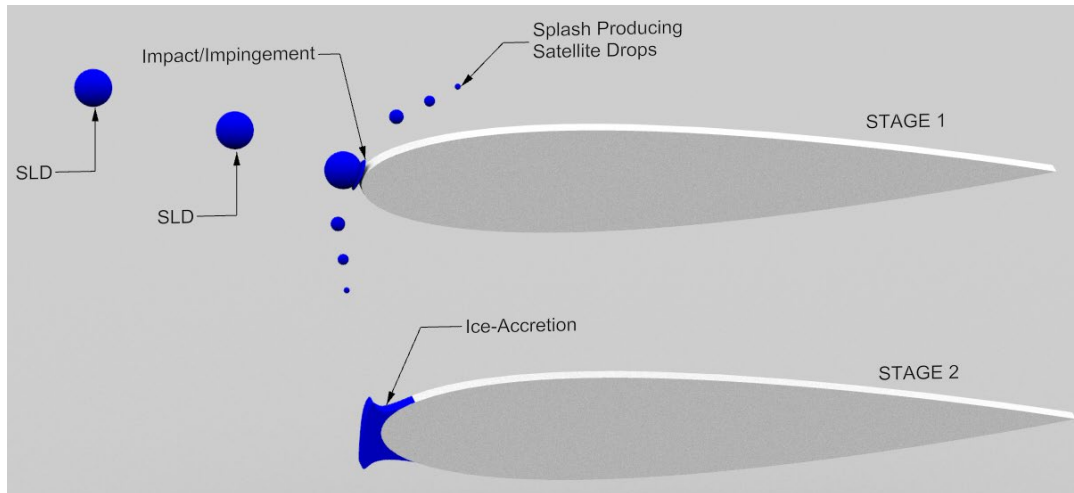
Figure 2: Stage 1 (top): Schematic showing the impingement and breakup of SLDs on a NACA a wing. Stage 2 (bottom): Schematic showing the ice accretion and growth.

CHAPTER II

NUMERICAL METHOD

The gas-liquid multiphase solver used in this study solves the Navier-Stokes equations using the variable density pressure projection algorithm. [52] The discretization of the domain is done using Adaptive Mesh Refinement (AMR) to solve the density and pressure fluxes. The continuity equation solved for the immiscible, incompressible two-phase flows can be written as,

$$\nabla \cdot u = 0 \tag{1}$$

$$\rho(F_m, x^c)\left(\frac{\partial u}{\partial t} + u \cdot \nabla u\right) = -\nabla p + \nabla \cdot (2\mu(F_m, x^c)\varepsilon) - \sigma \kappa \nabla H_m(\phi) + F_{body} \tag{2}$$

where $u = (u, v, w)$ is the velocity vector, $\rho(F_m, x^c)$ is the density, μ is the viscosity, p is the pressure, κ is the curvature, σ is the surface tension, F_m is volume fraction function represented as,

$$F_m = \frac{1}{\Delta x \Delta y \Delta z} \int_{x_{i-0.5}}^{x_{i+0.5}} \int_{y_{j-0.5}}^{y_{j+0.5}} \int_{z_{k-0.5}}^{z_{k+0.5}} H_m(x) dz\, dy\, dx \tag{3}$$

where H_m is the Heaviside function as material indicator,

$$H_m(\phi_m) = \begin{cases} 1 & \phi_m > 0 \\ 0 & \text{otherwise} \end{cases} \tag{4}$$

which is constructed using the level set function ϕ_m,

$$\phi_m(x, t) = \begin{cases} > 0 & \text{for material m} \\ \leq 0 & \text{otherwise} \end{cases} \tag{5}$$

Since in the multi-material-multi-phase algorithm has two or more materials or phases present, the density, and the viscosity particular to gas or liquid in the domain can be identified in the following manner,

$$\rho(F_m, x^c) = \rho_l H(F, x^c) + \rho_g(1 - H(F, x^c)) \tag{6}$$

$$\mu(F_m, x^c) = \mu_l H(F, x^c) + \mu_g(1 - H(F, x^c)) \tag{7}$$

where $\rho_l, \rho_g, \mu_l, \mu_g$ are density of liquid, density of gas, viscosity of liquid, and viscosity of gas, respectively.

Finally, the ε is the deformation tensor given as,

$$\varepsilon = \frac{1}{2}(\nabla U + (\nabla U)^T) \tag{8}$$

And the σ is the surface tension coefficient to account for the interfacial forces in between the material interfaces. κ is the curvature,

$$\kappa = \nabla \cdot \frac{\nabla \phi}{|\nabla \phi|} \tag{9}$$

and the F_{body} for the multiphase flow can be written as,

$$F_{body} = \sigma_{1,2}(\nabla \cdot \mathbf{n})\nabla H \tag{10}$$

where $\mathbf{n}$ is the unit normal of the interface given as,

$$\mathbf{n} = \frac{\nabla H}{|\nabla H|} \qquad (11)$$

Interface Reconstruction Methods: The Origin of Volume and Moment of Fluid Method

For the reconstruction of the Moment of Fluid (MOF), a special centroid function, x^c is employed, and thus it is a little different than the commonly used Volume-of-Fluid (VOF) or Coupled-Level-Set VOF (CLSVOF). But before going to moment of fluid (MOF) reconstruction, we will briefly present the general volume of fluid (VOF) reconstruction method here:

The following are the governing equations for interface reconstruction for Parker and Youngs'[53] PLIC 2D method:

The equation of the interface segment is written to be,

$$n.x = n_x x + n_y y \qquad (12)$$

The normal $\mathbf{n}$ (with n being the unit normal, i.e. n=m/|m|) can be estimated using the following relationship,

$$m = -\nabla_h C \qquad (13)$$

where $\mathbf{C}$ are cells under consideration.

To illustrate the equations of the most used VOF-Scheme by Parker and Young's Method[53], consider the following cell (3×3 stencil) arrangement:

9

$m_{x,i-0.5,j+0.5} = \frac{1}{2h}[C_{i,j} - C_{i-1,j} + C_{i,j+1} - C_{i-1,j+1}]$

$m_{y,i-0.5,j+0.5} = \frac{1}{2h}[C_{i-1,j+1} - C_{i-1,j} + C_{i,j+1} - C_{i,j}]$

$m_{x,i+0.5,j+0.5} = \frac{1}{2h}[C_{i+1,j} - C_{i,j} + C_{i+1,j+1} - C_{i,j+1}]$

$m_{y,i+0.5,j+0.5} = \frac{1}{2h}[C_{i,j+1} - C_{i,j} + C_{i+1,j+1} - C_{i+1,j}]$

A i-1, j+1	B i , j+1	C i+1, j+1
D i-1 , j	E i , j	F i+1 , j
G i-1 , j-1	H i , j-1	I i+1 , j-1

$i-\frac{1}{2}, j+\frac{1}{2}$ $i+\frac{1}{2}, j+\frac{1}{2}$ $i-\frac{1}{2}, j-\frac{1}{2}$ $i+\frac{1}{2}, j-\frac{1}{2}$

$m_{x,i-0.5,j-0.5} = \frac{1}{2h}[C_{i,j} - C_{i-1,j} + C_{i,j-1} - C_{i-1,j-1}]$

$m_{y,i-0.5,j-0.5} = \frac{1}{2h}[C_{i-1,j} - C_{i-1,j-1} + C_{i,j} - C_{i,j-1}]$

$m_{x,i+0.5,j-0.5} = \frac{1}{2h}[C_{i+1,j} - C_{i,j} + C_{i+1,j-1} - C_{i,j-1}]$

$m_{y,i+0.5,j-0.5} = \frac{1}{2h}[C_{i,j} - C_{i,j-1} + C_{i+1,j} - C_{i+1,j-1}]$
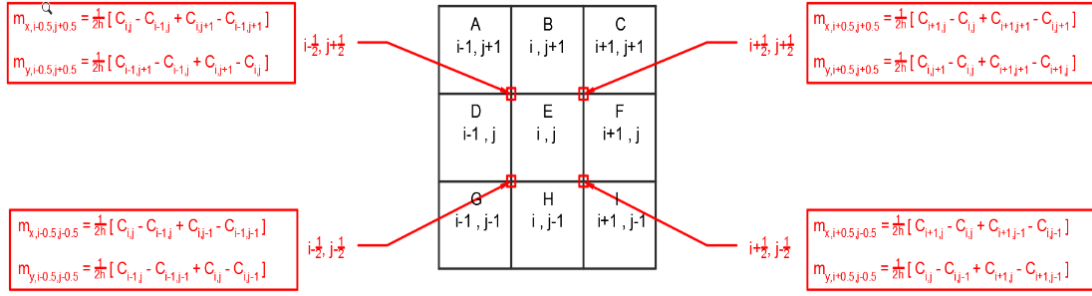
Figure 3: Grid Identification to reconstruct a volume for Parker and Young's Method

And the cell-centered vector is finally obtained by averaging the four cell-corner values[54],

For x-directions:

$$m^{x}_{i,j} = \frac{1}{4}\left(m_{x:i+\frac{1}{2},j+\frac{1}{2}} + m_{x:i+\frac{1}{2},j-\frac{1}{2}} + m_{x:i-\frac{1}{2},j+\frac{1}{2}} + m_{x:i-\frac{1}{2},j-\frac{1}{2}}\right) \tag{14}$$

For y-directions:

$$m^{y}_{i,j} = \frac{1}{4}\left(m_{y:i+\frac{1}{2},j+\frac{1}{2}} + m_{y:i+\frac{1}{2},j-\frac{1}{2}} + m_{y:i-\frac{1}{2},j+\frac{1}{2}} + m_{y:i-\frac{1}{2},j-\frac{1}{2}}\right) \tag{15}$$

Pilliod and Puckett [55] proposed the same equations but illustrated the scheme a little different, which we also present here:

The differential scheme needed to construct the Volume of Fluid Method requires the construction of the artificial interface and should be made to match the original available volume.

Let us consider, that the change in gradient in x-direction and y-direction rows and columns to be as:

∇f could be calculated using the following schemes,

$$\frac{\partial f}{\partial x} = \frac{f_E - f_W}{2} \tag{16}$$

$$\frac{\partial f}{\partial y} = \frac{f_N - f_S}{2} \tag{17}$$

And the slope could be defined as,

$$\tilde{m} = \frac{-\frac{\partial f}{\partial x}}{\frac{\partial f}{\partial y}} \tag{18}$$

The variables f_E, f_W, f_N and f_S are defined by the following expressions,

$$f_E = \frac{1}{2+\alpha}(f_{i+1,j-1} + \alpha f_{i+1,j} + f_{i+1,j+1}) \tag{19}$$

$$f_W = \frac{1}{2+\alpha}(f_{i-1,j-1} + \alpha f_{i-1,j} + f_{i-1,j+1}) \tag{20}$$

$$f_N = \frac{1}{2+\alpha}(f_{i-1,j+1} + \alpha f_{i,j+1} + f_{i+1,j+1}) \tag{21}$$

$$f_S = \frac{1}{2+\alpha}(f_{i-1,j-1} + \alpha f_{i,j-1} + f_{i+1,j-1}) \tag{22}$$

Moment of Fluid Interface Reconstruction:

For the Moment-of-Fluid reconstruction method, along with the $F_m = \nabla f$ from equation, the material centroid is needed.

The centroid, x^c for a liquid material in a given computational cell and can be computed using,

$$x^c = \frac{\int_{x_{i-0.5}}^{x_{i+0.5}} \int_{y_{j-0.5}}^{y_{j+0.5}} \int_{z_{k-0.5}}^{z_{k+0.5}} H_m(x) x \, dz \, dy \, dx}{\int_{x_{i-0.5}}^{x_{i+0.5}} \int_{y_{j-0.5}}^{y_{j+0.5}} \int_{z_{k-0.5}}^{z_{k+0.5}} H_m(x) dz \, dy \, dx} \tag{23}$$

In between the considered material regions, the interface between two materials can be represented as, $\Gamma_{m1,m2}$, and $\mathbf{n}$ as the unit normal vector always pointing away from the cell face, as shown in the following Figure 4.
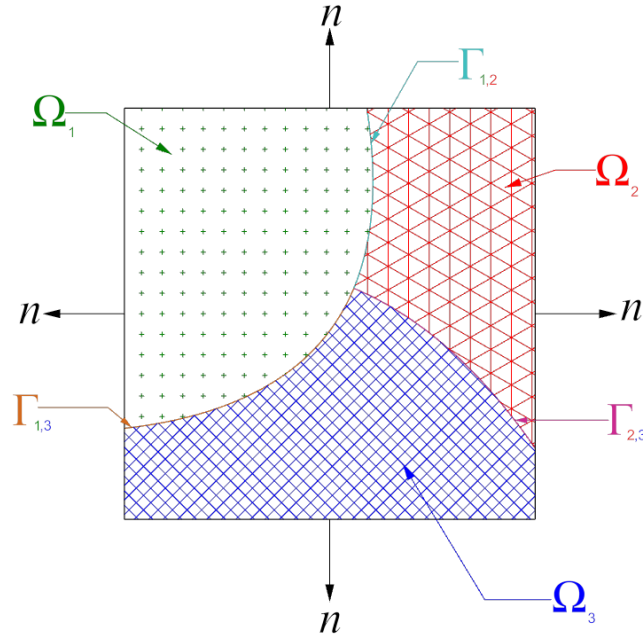
Figure 4: Three Material with Interface

With the piecewise linear multi-material MOF reconstruction[56], the interface in between two materials can be represented as a straight line with a normal $\mathbf{n}$ and a intercept $\mathbf{b}$ and stems from a reference volume, F_{ref} and reference centroid x_{ref}.

Therefore, the interface can be represented as,

$$\Gamma = [(x|n) \cdot (x - x_0) + b = 0] \tag{24}$$
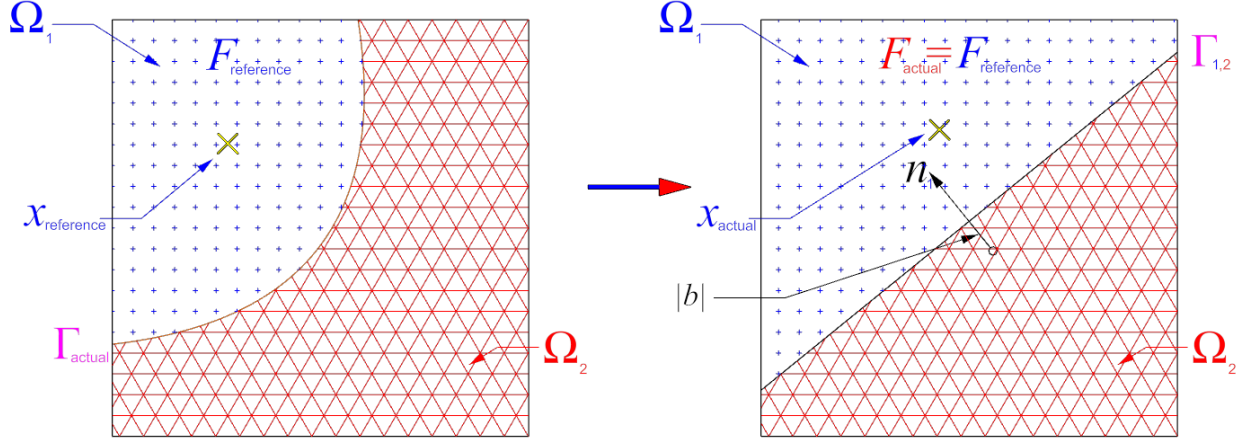
Figure 5: MOF Interface Reconstruction

The normal for each of the cell representing more than one material can be written as following,

$$n = \begin{bmatrix} \sin(n)\cos(b) \\ \sin(n)\cos(b) \\ \cos(n) \end{bmatrix} \tag{25}$$

As shown in Figure 5, with the constrain set to match the actual volume to reference volume,

$$\left| F^c_{reference,m} - F^c_{actual,m}(n,b) \right| = 0 \tag{26}$$

an error minimization criterion is employed with the following condition,

$$(n,b) = \mathrm{argmin}(E_{MOF}) = argmin\ ||x_{reference} - x_{actual}(x,b)|| \tag{27}$$

Gauss-Newton algorithm tolerance for this equation by finding the slope is $\varepsilon_{slope} = 10^{-10}$ and the Brent's method tolerance for finding the intercept is $\varepsilon_{intercept} = 10^{-12}$. If the material within the computed cell is of more than two types, nested dissection algorithm

is applied to perform the proper MOF reconstruction [57], where the centroid for the subsequently reconstructed material is selected to be the farthest to the centroid of the un-captured volume.

Moment of Fluid Interface Advection

Once the interface is reconstructed using appropriate error minimization, the advection becomes the next step. The interface position is integrated using the direction splitting method as proposed by Jemison et al. [7]. We will present the direction splitting method of advection on a single computation cell and towards the x-direction in this reference:

As depicted in the Figure 6 .The departing computation cell in this case can be described as:

$$\Omega_i^{\text{Depart}} = [x_{i-0.5} - u_{i-0.5}\Delta t, x_{i+0.5} - u_{i+0.5}\Delta t] \tag{28}$$

where $u_{i-0.5}$ and $u_{i+0.5}$ are horizontal velocities in the MAC grid.
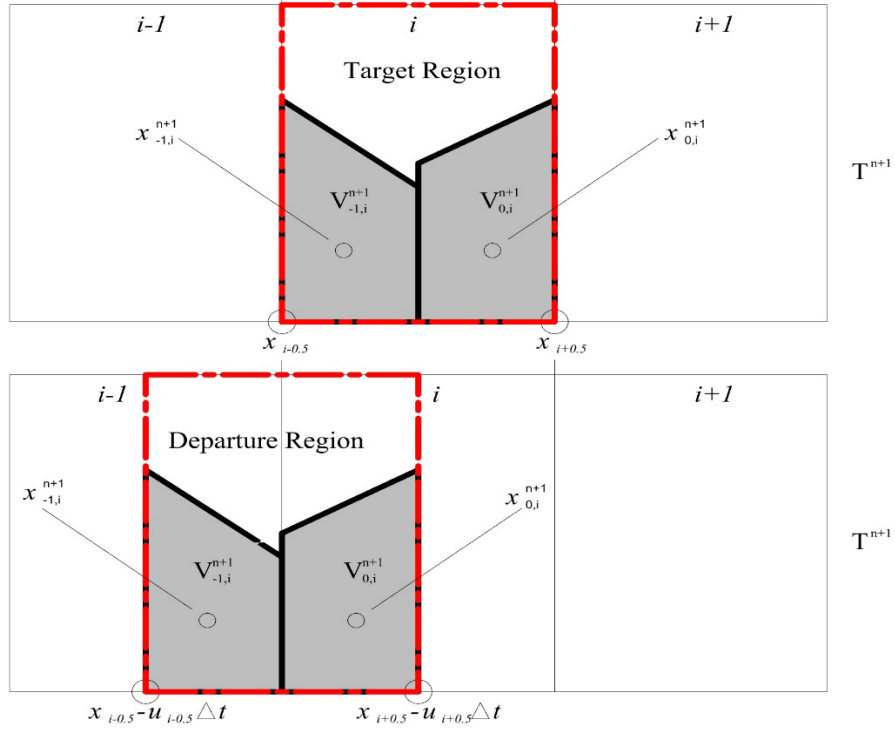
Figure 6: Transitioning from Departing Cell to Target Cell

The target computation cell, in regard to the departing cell, could therefore be written as:

$$\Omega_{i,Target}^{Depart} = [x_{i-0.5}, x_{i+0.5}] \tag{29}$$

Due to the departure to the target transition, the mapping could be described as,

$$\chi' = \alpha\chi + \beta = \frac{\Delta x\left(x - (x_{i-0.5} - u_{i-0.5}\Delta t)\right)}{(x_{i+0.5} - u_{i+0.5}\Delta t) - (x_{i-0.5} - u_{i-0.5}\Delta t)} + x_{i-0.5} \tag{30}$$

$$[x_{i-0.5} - u_{i-0.5}\Delta t, x_{i+0.5} - u_{i+0.5}\Delta t] \rightarrow [x_{i-0.5}, y_{i+0.5}] \tag{31}$$

The new centroids and the mapped volumes are calculated as follows,

$$V_{i,target}^{Dark} = \sum_{i'=-1}^{+1} \int H(n_{i+i'} \cdot \frac{x' - x'_{i+i'}}{\alpha} + b)dx' \tag{32}$$

$$V_{i,target}^{total} = \sum_{i'=-1}^{+1} \int 1dx' = V_i \tag{33}$$

$$x_i^{dark} = \frac{\sum_{i'=-1}^{+1} \int x' H \left(n_{i+i'} \cdot \frac{x' - x'_{i+i'}}{\alpha} + b \right) dx'}{V_{i,target}^{dark}} \tag{34}$$

x_i^{light} follows the same correction with H being $1 - H$ and thus the updated volume fraction therefore becomes,

$$F_i^* = \frac{V_{i,target}^{dark}}{V_i} \tag{35}$$

16

Special Computational Treatment: When material/phase is more than two

These special steps are presented because they are required for contact angle modelling, surface tension and curvature estimation while number of materials present in the computation is more than >2. Before presenting the surface tension force calculation scheme for more than two materials, the case for two materials only is presented here.

The surface tension force for any given material is generally termed as:

$$F_m^{tension} = -\Delta t \frac{\sum_{m=1}^{M} \gamma_m \kappa_m \nabla H(\phi_m)}{\rho} \tag{36}$$

Ghost fluid method is applied to calculate the surface tension force in a given discretized form

At the cell face:

$$F_{i+\frac{1}{2},j,m}^{MAC} = -\Delta t \frac{\gamma_m \kappa_{i+\frac{1}{2},j,m} \left(H(\phi_{i+1,j,m}) - H(\phi_{i,j,m}) \right)}{\rho_{i+\frac{1}{2},j,m}^{n+1} \Delta x} \tag{37}$$

At the cell centers:

$$F_{i,j,m}^{tension} = \frac{\rho_{i+\frac{1}{2},R} F_{i+\frac{1}{2},j,m}^{MAC,tension} + \rho_{i-\frac{1}{2},L} F_{i-\frac{1}{2},j,m}^{MAC,tension}}{2\rho_{i+\frac{1}{2},j,m}^{n+1}} \tag{38}$$

Level Set Height Function method[58-60] is used to calculate the approximate curvature $\kappa_{i+\frac{1}{2},j,m}$ same way it is calculated at $\kappa_{i,j,m}$:

$$\kappa_{i,j,m} = \frac{\dfrac{h_{i+1} - 2h_i + h_{i-1}}{\Delta x^2}}{\left(1 + \left(\dfrac{(h_{i+1} - h_{i-1})}{2\Delta x}\right)^2\right)^{\frac{3}{2}}} \tag{39}$$

where the heights $h_{i-1}, h_i, h_{(i+1)}$ are calculated of a given cell using the zero-crossing level set function ϕ for a given cell:

$$h_{i'} = (1 - \alpha_{i'})y_{i',j} + \alpha_{i'}y_{i',j} \tag{40}$$

where,

$$\alpha_{i'} = \frac{\left|\phi_{i',j}\right|}{\left|\phi_{i',j}\right| + \left|\phi_{i',j+1}\right|} \quad \text{with } i' = i - 1, i, i + 1 \tag{41}$$

Now that we have presented the estimation of surface tension force for two materials, we present the case where the material number is equal to or more than three.

For $m \geq 3$, the height function technique is not usable, and therefore finite difference scheme is employed in conjunction with the ghost fluid method.

There are two different scenarios when considering multi-material case:

1) Two fluids with one solid, as shown in Figure 7 (left)

2) Three fluids at an intersection, as shown in Figure 7 (right)

Using the level set functions that are stored in the cell centers, we calculate the curvature,

$$\kappa_{i,j} = \nabla \cdot \left(\frac{\nabla \phi}{|\nabla \phi|}\right) \tag{42}$$

Consider the case of the cell and the corresponding corners denoted as n^1, n^2, n^3, n^4. Using

the central differencing method, the normal level set function $\frac{\phi}{|\phi|}$ for n^1 can be calculated

as:

$$n^1 = \frac{\left(\dfrac{\phi_{i,j+1} - \phi_{i-1,j+1}}{\Delta x}, \dfrac{\phi_{i,j+1} - \phi_{i,j}}{\Delta y}\right)}{\left\|\dfrac{\phi_{i,j+1} - \phi_{i-1,j+1}}{\Delta x}, \dfrac{\phi_{i,j+1} - \phi_{i,j}}{\Delta y}\right\|} \tag{43}$$

and notice that $n^4 = n^{ghost}$ because it is in relation to the solid material and the ghost

normal replaces the unit normal. The preset contact angle, and the ghost interface provides

us the ghost normal that points from material 2 to material 1.

After interpolating the four normal at the four corners, the curvature can be calculated using

the following method:

$$\kappa_{i,j} = \frac{1}{(\Delta x)(\Delta y)} \sum_{l=1}^{4} \frac{\nabla \phi_l}{|\nabla \phi_l|} \vec{n_l} \tag{44}$$

Once the curvature is calculated, the same method using the ghost fluid method shown in

eq. (41) is used to calculate the surface tension force.
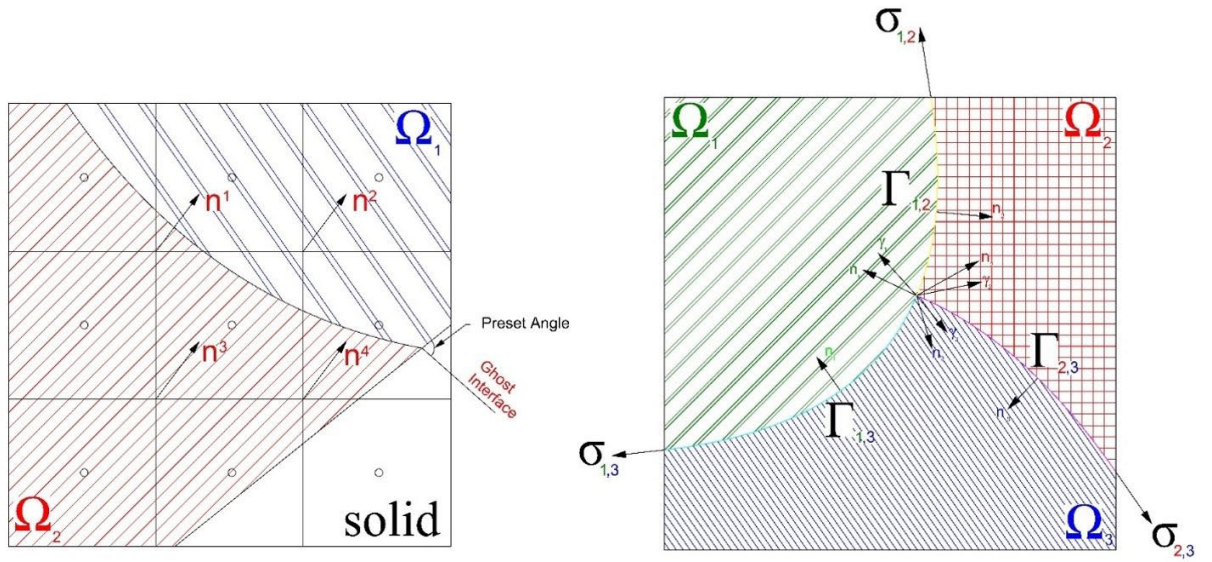
Figure 7: Surface Tension Force Calculation for: a) two fluid and a solid (left) b) three fluid forming triple point (right)

CODE VALIDATION

Code Validation - 1

We first simulate a well-document experimental study to show the capability of the numerical method. The experiment was conducted by Kim et al. [61]. They studied a water drop impacting a flat substrate at a speed of 0.77 m/s. The radius of the water drop is 1.8 mm with liquid density of $998 \frac{\text{kg}}{\text{m}^3}$, and viscosity of $8.67 \times 10^{-4} \frac{\text{kg}}{\text{m-s}}$. In the simulation the dynamic contact angle model by Jiang et al.[62] shown below is used:

$$\frac{\cos(\theta_e) - \cos(\theta_d)}{\cos(\theta_e) + 1} = \tanh(4.96 Ca^{0.702}) \tag{1}$$

where θ_e θ_a, and θ_r are the equilibrium, advancing and receding contact angles, and their values are 87.4°, 114° and 52°, respectively. Ca is the capillary number defined as $Ca = \frac{\mu_l U_0}{\sigma}$, with μ_l being the viscosity of the liquid. The surface tensions between liquid and gas, liquid and solid, and solid and gas are 0.0728, 0.0695 and 0.0728 N/m, respectively. Figure 8 compares drop spreading and recoiling after impact between the experiment and simulation. Our simulation shows excellent agreement with the experiment. A comparison of base diameter between experiment and simulation is shown in Figure 9. The agreement is also good. Note, Figure 5 shows nondimensionalized based dimeter defined in Eq. 17. The code has been used to study other drop impact cases and the results are reported Yan et al.[63, 64]
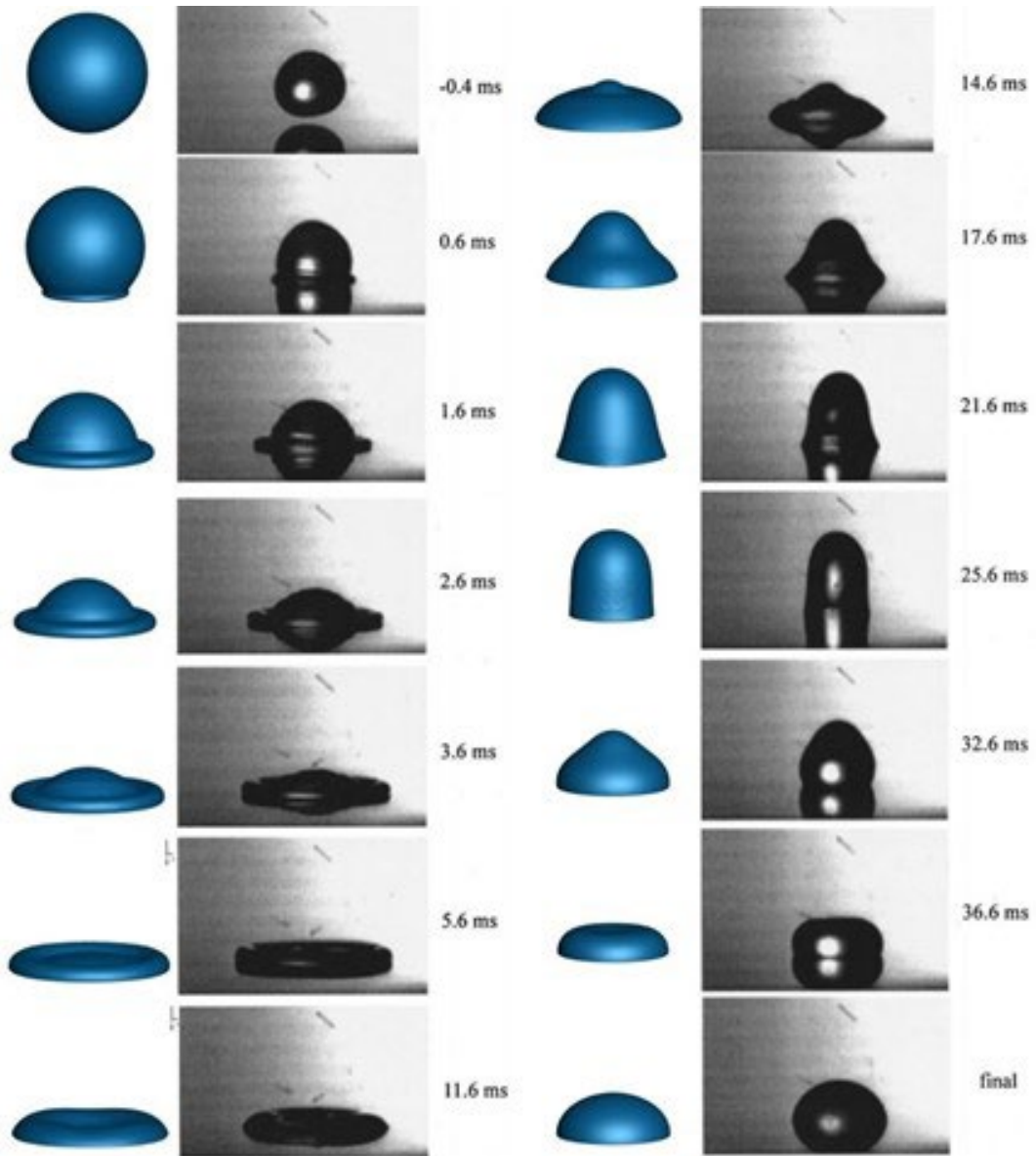
Figure 8: Comparison between simulation (blue) and experiment (black) from Kim et al.[61]
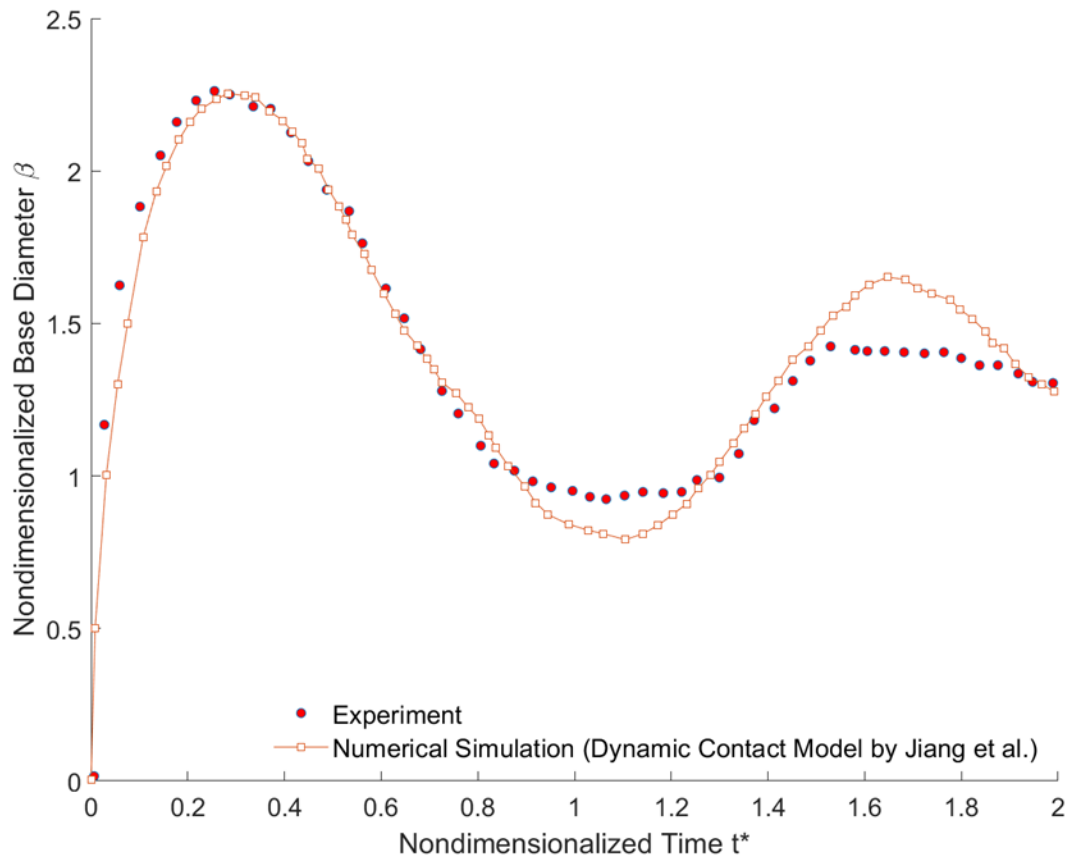
Figure 9: Comparison of non-dimensional base diameter between experiment [61] and simulation. In the simulation, Jiang et al. [62] dynamic contact angle model is used.

Code Validation - 2

For the purpose of code verification, a coalescence induced case on a single fiber is reproduced and presented here. Two water droplets, each having an average radius of 249 μm, were placed next to a Teflon-coated copper fiber, having a constant radius of 46μm. The coating provides an advancing and receding contact angles of $\theta_A = 121 \pm 3°$ and $\theta_R = 108 \pm 2°$. The coalescence process, as will be discussed later, is governed by the capillary inertial velocity and time having the following relationship: $u_{ci} = \sqrt{\dfrac{\sigma}{\rho r_d}}$ and $t_{ci} = \sqrt{\dfrac{\rho r_d^3}{\sigma}}$, where ρ, σ and r_d are the density, surface tension and the radius of the water droplet, respectively. The coalescence around the fiber is well matched as can been seen in the given Figure 10.
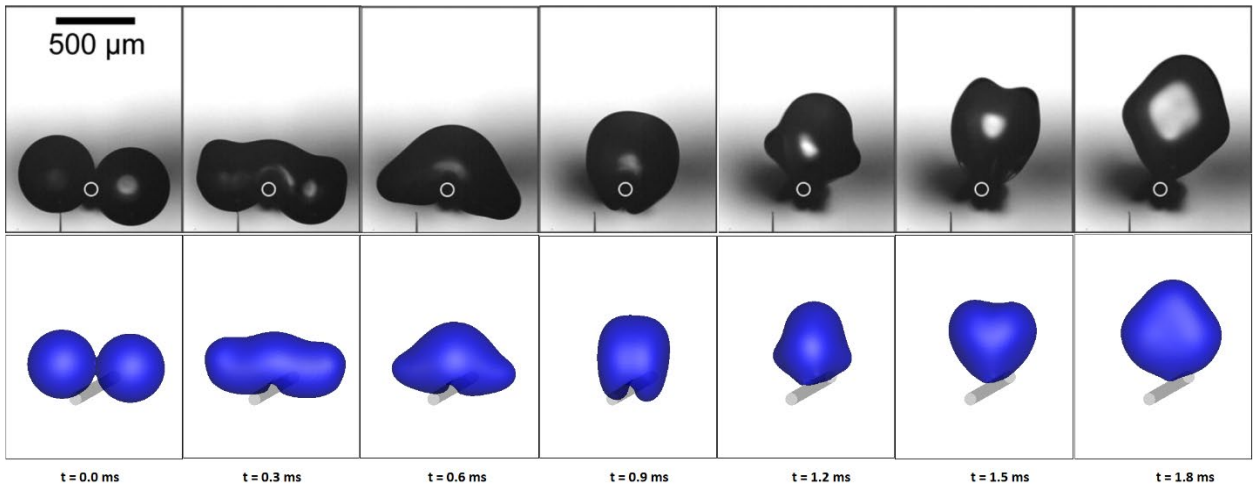
Figure 10: Coalescence Around a Fiber: Experiment (top) and Simulation (bottom)

CHAPTER III

DROP COALESCENCE ON A CURVED SUBSTRATE*

Self-propelling droplet jumping due to coalescence has earned a great deal of interest in recent times due to its inherent benefit in dropwise condensation, release of heat energy, shorter liquid-substrate contact time and conversion of excess surface energy into kinetic energy. Heat exchangers using dropwise condensation has greater degree of benefit over film-wise condensation[65-67]. Anti-icing surfaces with micropores can help achieve enhanced removal of condensed microdroplets[68, 69]. Dewing and condensate collection through modifying wettability and substrate geometry also uses the benefit of dropwise condensation[70, 71].

Spontaneous jumping on Leidenfrost surfaces due to the insulating vapor layer results in perfect super hydrophobicity with a contact angle of 180°, and thus enables greater control on the drop size by re-adjusting the contact line, while eliminating the drop-surface interaction [72]. Their study also observed the non-dimensional jumping velocity of approximately 0.2, following the capillary-inertial velocity with superhydrophobic surfaces. Boreyko et al. [67] reaffirmed this relationship of capillary inertial velocity, and found that the coalescence-induced velocity varies with the size of the coalescing droplets.

Non-wettability of the substrate on merging drops and the only contribution from the surface energy towards the self-propelling droplets were found by Wang et al [73] and Liu et al.[74]. Patterned surfaces with superhydrophobic behaviors are inspired by natural elements, like lotus leaf and insect wings[75-81]. Low adhesivity to water drops off of micro-nano patterned surface shows the positive effect on self-propelled jumping drops[2, 65, 77-79, 82]. Curved surfaces have positive effect on the bouncing liquids, and Hao et al.[83] found that bouncing occurred on spherical surfaces, whereas failed on other surfaces with varying arrays. Liu et al. [84] reported a 30% reduction of the contact time of bouncing drop on a curved surface compared to flat surfaces[85-87]. Zhang et al. [88] reported a critical impact on self-propelled behavior due to the curvature of the fiber. The self-bouncing process upon drop coalescence happened on a fiber at contact angles of $\frac{\theta_A}{\theta_R} =$ 120°/110° (where θ_A and θ_R are the advancing and receding contact angles, respectively). The effect of curved surface was believed to accelerate the merged drop orthogonal to the fiber and obey the capillary-inertial law[72, 74]. A greater extent of useful translational energy could be extracted due to the lesser area of contact between the drops and the fiber and consequently less substrate-drop adhesion.

Theory: The Self-Propelled Jumping Upon Coalescence
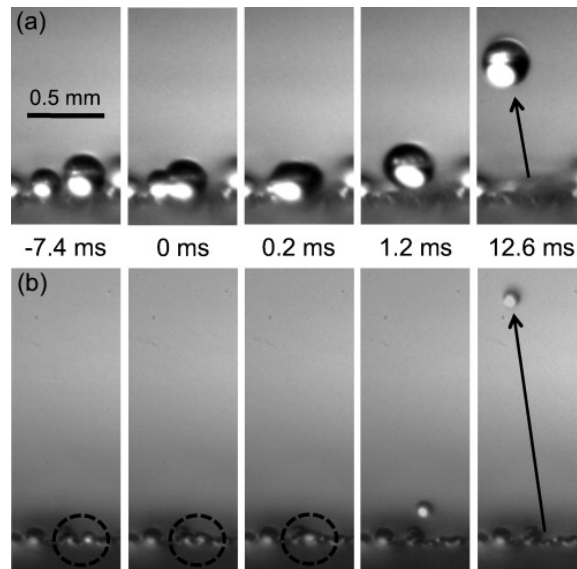
Figure 11: Coalescing Drops D=200µm to 270µm Jumping Reproduced with permission from Boreyko et al., Phys. of Fluids 22, 9 (2010) Copyright 2002 AIP Publishing LLC [67]

Different models have been used to analyze the jumping capability[72, 89, 90]. The theoretical jumping velocity can be obtained when supposing all excessive surface energy is transferred into kinetic energy in the jumping direction and therefore an empirical model is obtained based on the experimental data [72, 89, 90]. Consider two drop model shown in Figure 12.
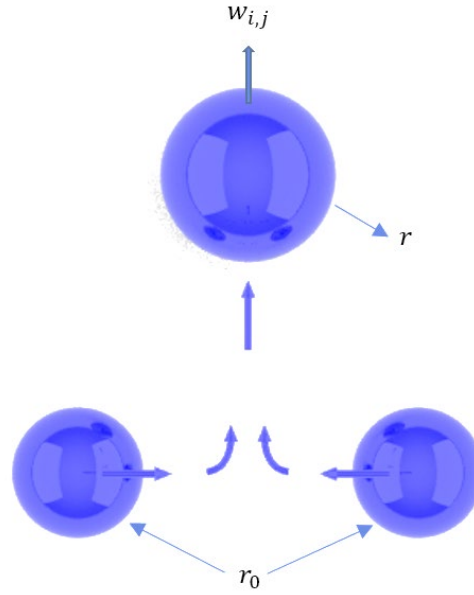
Figure 12: Drop Coalescence and Jumping

The energy conversion could be explained in terms of the capillary inertial velocity law and by means of non-dimensionality can be explained as,

$$w_{i,j} \sim u_{ci} = \sqrt{\frac{\sigma}{\rho_l r_0}} \tag{45}$$

Both the drops have identical radius, r_0 and upon coalescence the equivalent radius becomes,

$$r = 2^{\frac{1}{3}} r_0 \tag{46}$$

with the combined drop having a mass,

$$m = \frac{8}{3} \rho_l \pi r_0^3 \tag{47}$$

Upon coalescence, energy conversions between several different types occur, namely between surface energy, kinetic energy, potential energy and viscous dissipation energy.

The total surface energy of a stationary droplet on a superhydrophobic surface can be written as,

$$E_S = \sigma_{LV}A_{LV} + \sigma_{LS}A_{LS} + \sigma_{SV}A_{SV} \qquad (48)$$

where, A is the interfacial area, σ is the surface tension and the subscript LV, LS, and SV represents interfaces between liquid-vapor, liquid-solid, and solid-vapor, respectively.

The expression of the kinetic energy of the droplet upon coalescence is defined as,

$$E_K = \frac{1}{2}\rho V(u^2 + v^2 + w^2) \qquad (49)$$

with ρ being the density, V the drop volume, and u, v, and w are the velocity components in x, y and z directions, respectively.

The viscous dissipation energy for the droplet can be written as,

$$E_{VISC} = \int_0^t \int (\Phi dV)\, dt \qquad (50)$$

where Φ is the dissipation function defined as,

$$\Phi = \mu\left(2\left(\left(\frac{\partial u}{\partial x}\right)^2 + \left(\frac{\partial v}{\partial y}\right)^2 + \left(\frac{\partial w}{\partial z}\right)^2\right) + \left(\frac{\partial u}{\partial y} + \frac{\partial v}{\partial x}\right)^2 + \left(\frac{\partial u}{\partial z} + \frac{\partial w}{\partial x}\right)^2\right.$$
$$\left. + \left(\frac{\partial v}{\partial z} + \frac{\partial w}{\partial y}\right)^2\right) \qquad (51)$$

with μ being the viscosity of the liquid and t as the time.

Upon coalescence, the surface area reduces, and consequently there is a release of excess surface energy which could be written as,

$$\Delta E_S = 4\sigma\pi r_0^2 (2 - 2^{\frac{2}{3}})$$ (52)

If the entire surface energy is converted into kinetic energy, then the maximum jumping velocity could be deduced as,

$$w_{j,max} \approx 1.11 \sqrt{\frac{\sigma}{\rho_L r_0}}$$ (53)

This maximum jumping velocity could therefore be scaled to capillary inertial velocity, u_{ci}.

There is still some disagreement as to how much surface energy could be converted to kinetic energy upon coalescence. Below are some of the recent studies that reported different energy conversion rates:

Table 1: Energy Comparison : From Surface to Kinetic Energy Upon Coalescence

Enright et al. [91]	6% of excess surface energy is converted
Peng et al. [92]	25% of energy released is found to be converted
Nam et al. [90]	Approximately 50% of energy is found to be converted

Surface Wettability: The Importance of Contact Angle
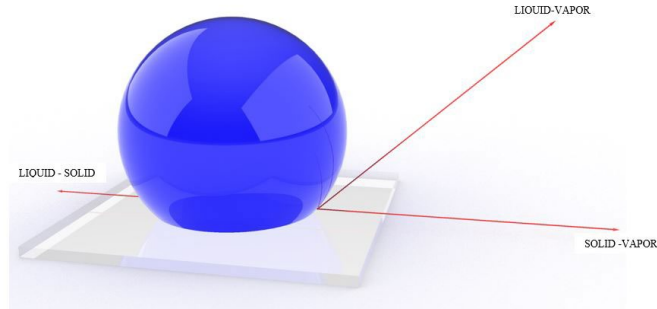
Figure 13: Contact Angle of a Drop on Substrate with Surrounding Air

Drop impact, rebound, and splashing is very much affected by the contact angle that is stipulated in between the surface and the droplet. Similarly, for coalescence and the subsequent jumping, the contact angle plays a critical role.

Due to interfacial forces coming into equilibrium, the droplet adjusts its form to an equilibrium contact angle known as the Young's Contact Angle. This angle also establishes the contact line where the three phases liquid, gas and solid forms the interfaces, namely Liquid-Vapor, Liquid-Solid and the Solid-Vapor. Young [93] introduced the equilibrium model with the following surface tension relationship,

$$\cos\theta = \frac{\sigma_{SOLID-VAPOR} - \sigma_{SOLID-LIQUID}}{\sigma_{LIQUID-VAPOR}} \tag{54}$$

To understand wettability, when $\theta < 90°$ the substrate could be represented as hydrophilic or wettable (surface tends to adhere more to the surface). When $\theta > 90°$ the surface could be said to be hydrophobic or more favorable to wettability. With droplet-surface having $\theta \approx 180°$, these surfaces are known as extremely non-wetting and the substrate (surface) is called superhydrophobic.

Without the presence of the substrate, the coalescence of drops does not produce self-propulsion as reported by many studies [94, 95]. Similarly, hydrophilic and super-hydrophilic surfaces do not produce in self-propulsive droplets [96-99]. Contact angles giving a range of non-wetting characteristics to the surface causes self-induced jumping. Boreyko and Chen [67] reported the out-of-plane motion of the jumping drop due to coalescence on superhydrophobic surface. Therefore, we propose a series of new type of hydrophobic substrates that has been designed to eject coalescing drops with vert high energy. To make the substrates superhydrophobic, protruding wedges with varying curvatures are placed on the flat surface, as shown in Figure 14. Our study reveals that with an increase in wedge curvature, the jumping capability of the coalesced drop also increases. For each of the simulations, the radii of the drops are set to 380 µm and the properties of liquid and air at 100°C are used. The contact angle is set at 180°.

$$\kappa = 5/r_0 \qquad \kappa = 5/2r_0 \qquad \kappa = 1/r_0 \qquad \kappa = 0$$
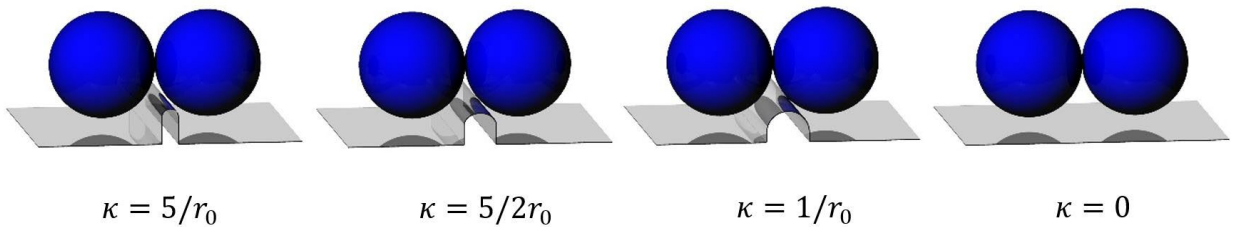
Figure 14: Drop Coalescence Setup on Substrates with Different Curvatures

The drops coalesce in the horizontal, i.e. the y-axis direction and the self-propelled behavior happens in the vertical or z-axis direction.

The dimensionless z-axis velocity histories of the four cases during the coalescence processes are plotted in Figure 16.
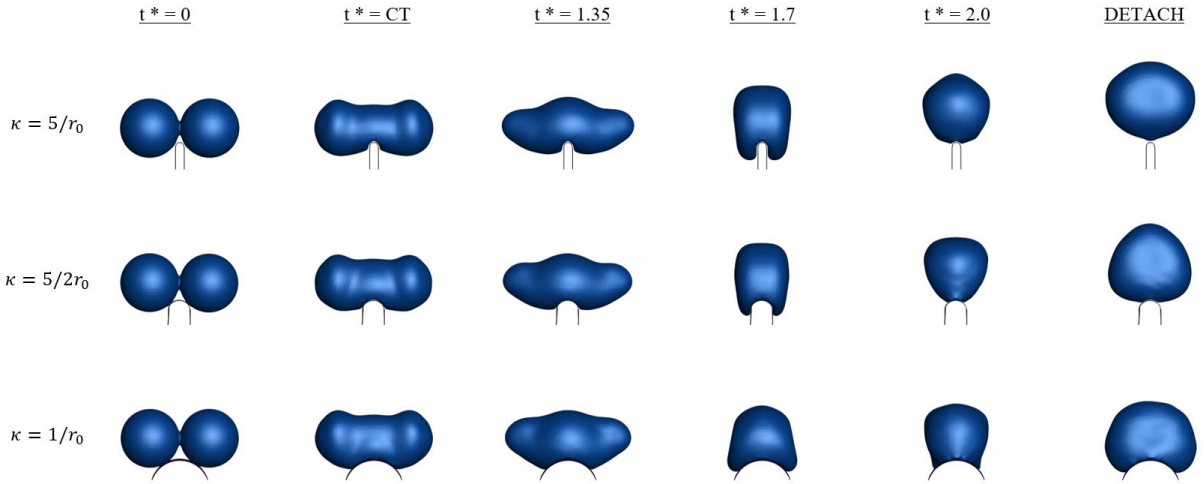
Figure 15: The process of drop coalescence on different curvatures
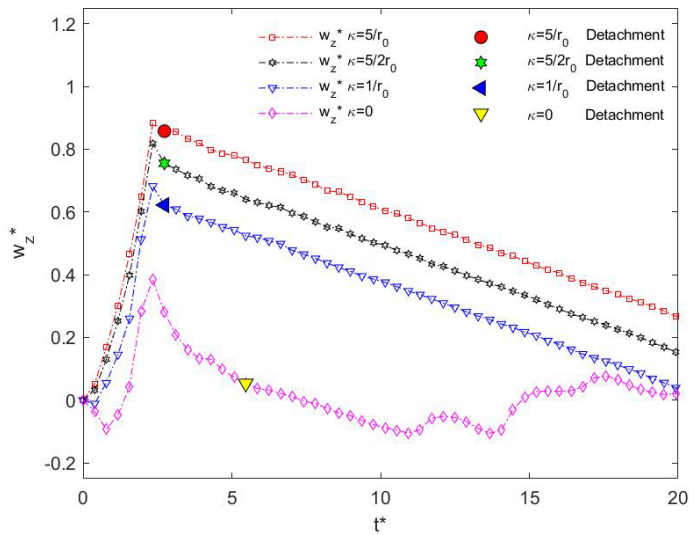
Figure 16: Velocity in the jumping direction (z-upwards)

Overall, the wedges have enabled drops with higher z-axis velocities than the flat surface. The jumping speed at the moment of detachment increases with the increase in curvature. The drop on the wedge with larger curvatures accelerates earlier in positive z-axis direction. As curvature increase the moment of detachment decrease too. Drop on the surface with curvature of   detaches the first and drop detaches the last on the flat surface.

Velocity plots also reveal that the maximum velocity attained by the $\kappa = 5/r_0$, is approximately 90% of the capillary inertial velocity, compared to 82%, 67% and only 38% in the cases of $\kappa = 5/2r_0$, $\kappa = 1/r_0$ and the flat substrate $\kappa = 0$.

The final height achieved through our investigation of different substrates shows the clear advantage of having substrate curvatures. The wedge curvature enables the coalescing drops to come into less contact with the substrate.

shows that the $\kappa = 5/r_0$, achieves a max height of $h_z = 0.435\mu m$, followed by $\kappa = 5/2r_0$ reaching $h_z = 0.36\mu m$ and $\kappa = 1/r_0$ reaching $h_z = 0.290$ μm.
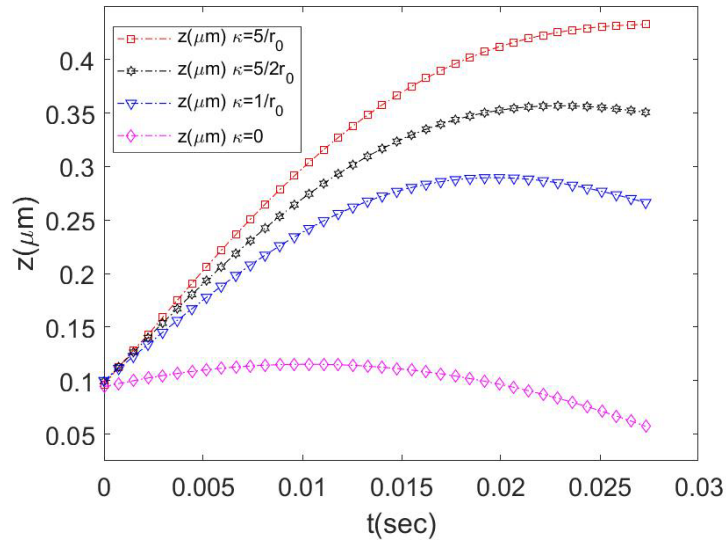
Figure 17: Drops travelling in z-axis direction due to coalescence on substrates with different curvatures $\kappa = 5/r_0$, $\kappa = 5/2r_0$, $\kappa = 1/r_0$ and $\kappa = 0$
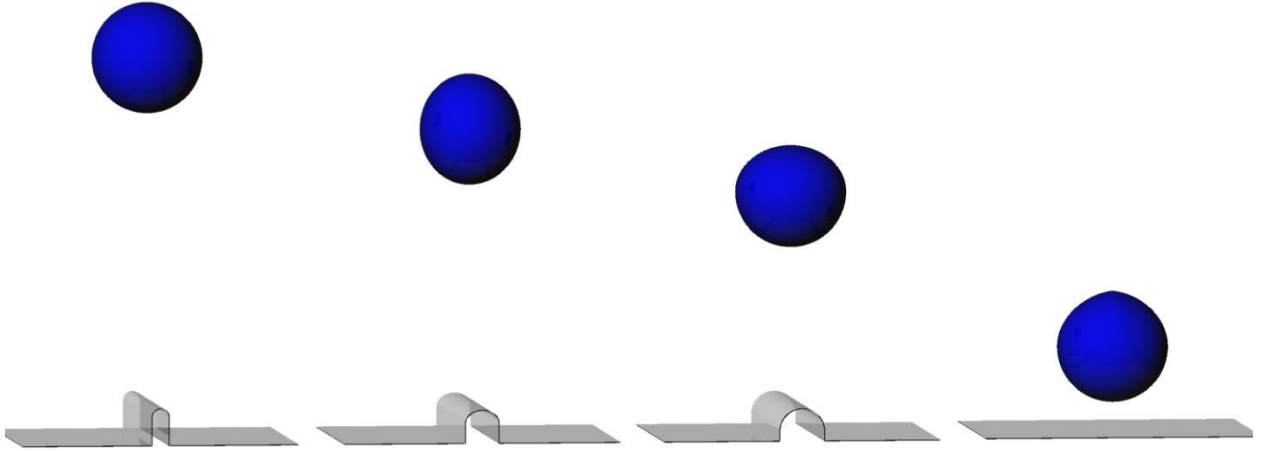
Figure 18: Final Height Depiction of Drops on Different Substrates with Curvature and Flatness

With the increase in curvature, the coalesced drop can stay suspended in the air for a longer period of time, with $\kappa = 5/r_0$, $\kappa = 5/2r_0$, and $\kappa = 1/r_0$ taking 27.3ms, 24.4ms and 21.03ms, respectively, to reach the maximum height. The evidence of curvature substrate enhancing the final jumping height is prominent when compared to the flat substrate $\kappa = 0$, which could only achieve a jumping height of $h_z = 0.1025$ μm and much shorter travelling time of 7.74ms to reach the maximum height.

We propose the following correlation between surface curvature and the achievable jumping height based on our findings.

$$H_{TRAJECTORY} = 0.0894 \ln(\kappa) + 0.2864 \qquad (55)$$

Figure 19 shows the correlation.
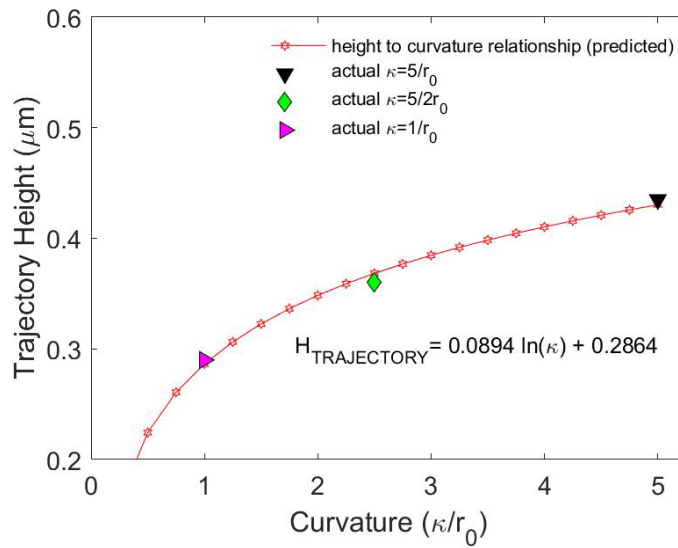
Figure 19: Relationship between achievable trajectory height and curvature

of wedged substrate

Thus, the substrates with curvature enables drops to detach faster than flat substrates do. Our simulations show drops have 40% less contact time on a curved surface than on a flat surface during the impact and rebound study. Second, the substrate curvature affects drop jumping velocity and jumping height. Our simulation shows the jumping velocity and jumping height increase with the substrate curvature. The shape and characteristics of the drop deformation varies due to the underlying substrate and thus the substrate curvature plays a critical role in coalescence induced jumping.

CHAPTER IV
DROP IMPACT ON A MICRO-WELL*

Numerous studies have been done over decades to understand the liquid-solid interactions with different substrate properties and solid surface hydrophilicity. In many cases surface hydrophobicity is very much sought after because liquid repellant properties can become useful in reducing contact times of liquid-solid interaction[100]. The complex dynamics of contact time, which is generally described as the duration of the droplet contact and consequently the spreading and the retracting phase, depends on the surface-liquid interactions[101]. Many researchers have deemed the spreading phase after drop impact to be particularly most important [102-104] and others have pointed out the importance of the retraction phase immediately after the spreading phase[105]. In some applications, it is desired to prolong the contact time such as inkjet printing[7, 8], pesticide transferring on crops[106-108] , spray cooling[1]. In other cases it is desired to reduce the contact time such as anti-corrosion and self-cleaning[5, 109-111] application, spray cooling[112-114], de-icing and anti-icing methods in aviation/aircraft industries[115-117].

In the nature there are many materials that exhibit superhydrophobicity with advancing contact angles ranging between 150° to 160° [118-121]and generally classified as features due to following: 1) lubricated films, such like epicuticular wax, providing a layer between the solid and liquid phases 2) roughness that can effectively entrap air and provide a barrier or a type of insulation medium and lastly 3) secondary texture with superimposing morphological surfaces. Focusing on the roughness of substrates, an idea coined from the nature, researchers have shown that an excellent non-wetting property could be achieved by micro-structures that encapsulates air or in general has additional gas or liquid phase[122, 123]. The underneath air entrapment dictates if a droplet would undergo Cassie state that demonstrates partial wetting or non-wetting or Wenzel state that shows complete wetting due to the liquid contacting the substrate while displacing the cushioning air[124]. Researchers focusing on fabricating superhydrophobic surfaces typically modify the surface property to provide certain degrees of roughness and use methods like abrasive polishing, plasma nano-texturing, etching, lithography, nano-coating and grit roughening, 3D printing etc[125-130]. All these certain methods allow researchers to entrap air within the micro- and nano structures by roughening the surface, such that the droplets can exhibit a Cassie-Baxter state of non-wettability instead of Wenzel state of fully wettability as shown in Figure 20. Micro-and macro-structures of many different kinds were researched in the past; such like substrates featuring triangular ridges[131], small spherical feature[132], short conical structure[133], different sizes of half spheres[134], large tubes[135] and curved surfaces[136], but most importantly micro-pillars or micro-posts[101, 137-140] that enhances faster wicking or pancake bouncing are of great interest. Anistropically wetting substrates, such like stripes with chemically alternating hydrophilic

and hydrophobic properties, are also sometimes considered more benefitting than isotropic substrates, like micro-pillars or micro-posts[141].
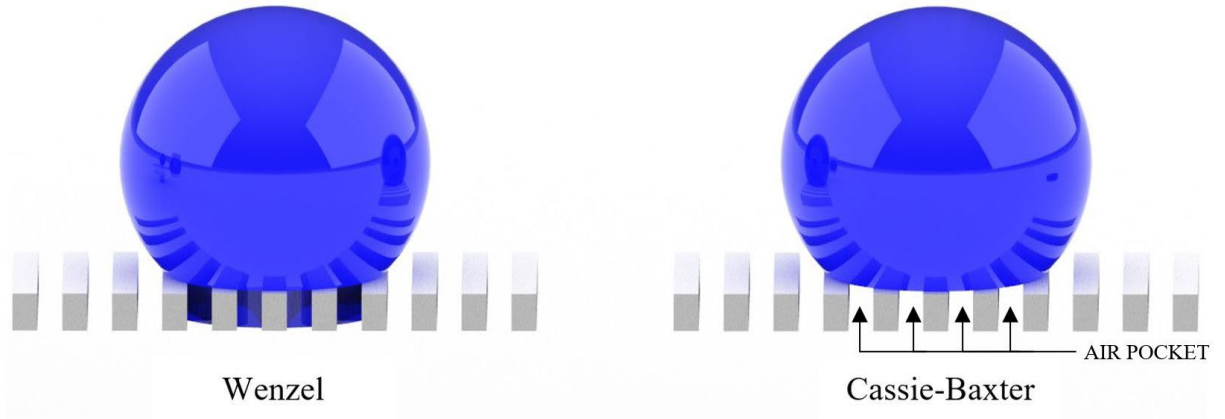
Figure 20: Wenzel State (left) vs Cassie-Baxter State (right)

While the air pocket entrainment or encapsulation needed for superhydrophobic surfaces is thoroughly understood and widely recognized by the scientific community, most of the studies have continued to focus on the drop shape evolution, the aspect of velocity and pressure changes within the drop or the volume of liquid, and possible reductions in contact times. It is conveniently understood that all superhydrophobic surfaces are textured or rough surfaces that entraps air pockets[45, 142-148], and droplets impacting on rough surfaces exhibit quick non-wetting and reduced contact times[149]. Similarly, with increased superhydrophobicity of rough surfaces, bulk kinetic energy is spent on spreading and retraction, and less into useful transformational energy harnessed for out of plane jumping, and therefore may lead to splashing and/or drop breakups into smaller satellite droplets[150, 151]. A very effective water repellency has been observed by Shen et al.[115] due to the rough surface where the water droplet bounced off before

freezing, resulting in reduction in icing strength because of low efficiency in thermal conduction between the water droplet and the cold solid surface. Bird et al[100, 152] discussed that with microtextured surfaces, controlling the extent of contact time can essentially dictate the mass, momentum and energy exchange and therefore it should be minimized. They experimented drop impacting on macroscopic structure/ridge to make axisymmetric recoil resulting in minimum contact timing. It is also theoretically suggested that thin spread textures are indispensable to trap air that results in reducing contact time[100, 153, 154]. Quan et al. [155] studied micro-pillars of different types and shapes, including triangular, square, crisscross and spherical cylinders, with crisscross showing the best bouncing ability, and such ability is attributed to large capillary pressure and the ability of capturing air in the gaps compared to other types of pillar shapes. Other researchers also discussed about the toroidal rim instability[156], development of rotational velocities within the rim and therefore resulting in partial or complete rebound, prompt, corona or receding breakup of droplets recoiling on superhydrophobic substrates that can entrap air pockets[157, 158].

In this chapter, we numerically investigated liquid water drop impact on a micro-well substrate and demonstrated how air inside a micro-well can prevent water droplet from wetting the bottom of the substrate. At first, we describe the numerical approach to the problem using the moment of fluid (MOF) algorithm, then we present the setup for the problem and demonstrate our accuracy and mesh sensitivity used in this study. Secondly, we use a single micro-well and show that drop impact at various speeds and contact angles can both benefit from reduced liquid-solid interaction and air acting as a barrier. Using the concept of a single micro-well, we further demonstrate drop impact cases on a substrate

with arrays of micro-wells and discuss the improved non-wettability compared to a substrate with arrays of micro-pillars.

Drop impact on a single micro-well
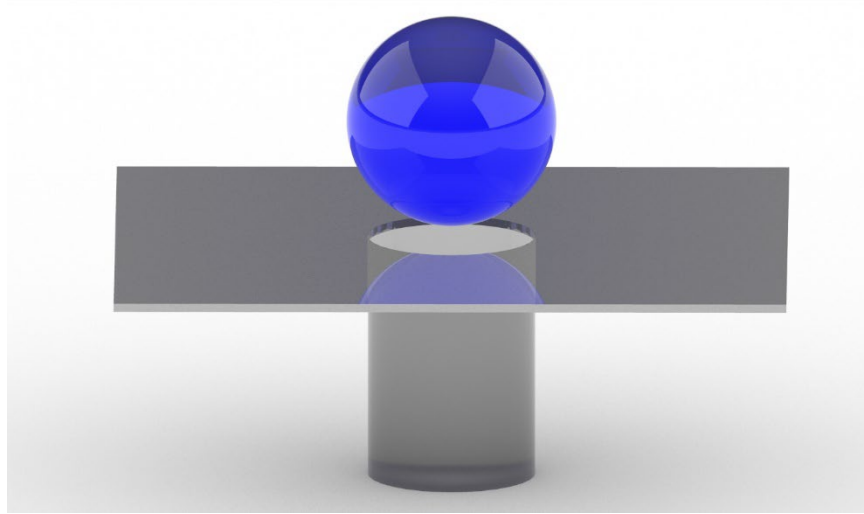
Figure 21: Drop impact on a single micro-well

The setup of drop impact on a single micro-well is shown in Figure 21. The drop has a diameter of 250 μm and the micro-well has a diameter of 200 μm and depth of 180 μm. The equilibrium contact angle is 120°. A drop is initially positioned 1 μm above the micro-well with an initial velocity of 2 m/s. Table 2 shows the liquid and gas properties used. To show the pertinent features of micro-well we also simulate drop impact on a flat surface under the same conditions.

Table 2: Liquid and gas properties used in this study

	σ (mN m^{-1})	μ_l (mPa s)	μ_g (mPa s)	ρ_l (kg m^{-3})	ρ_g (kg m^{-3})
10˚C	72.7	1.308	0.02	999.7	1.25
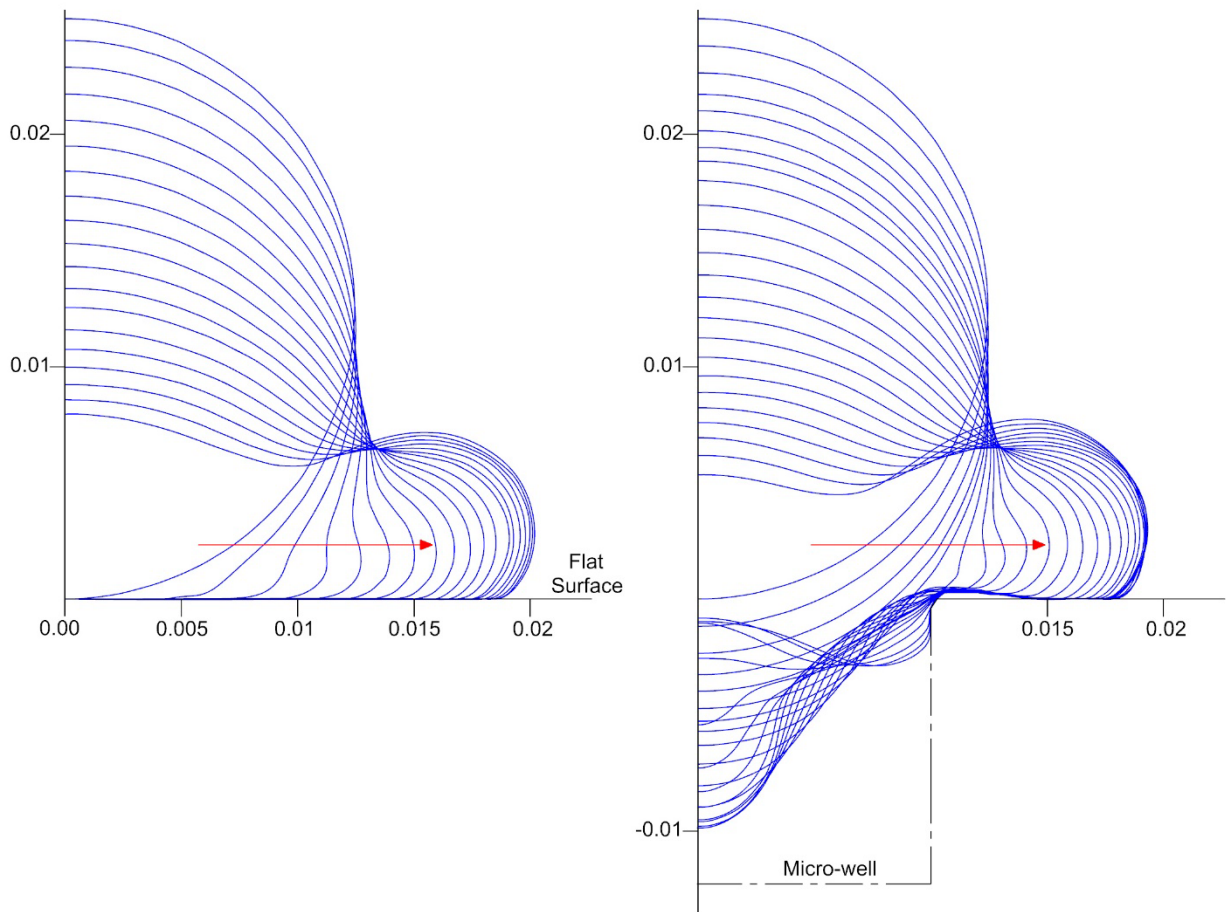
Figure 22: Simulation of drop spreading on (a) Flat surface (left) and (b) Micro-well (right)

Figure 22 shows the simulated drop spreading after impact on flat substrate and micro-well. In both cases drop spreads laterally but there is a noticeable difference between the two. As the bulk of drop enters the micro-well, the drop remains suspended in the air without ever touching the well bottom, resulting in a much smaller wetted substrate in the case of micro-well. Here we use spreading ratio and the wetted area ratio to explain the differences between these two cases. Spreading ratio is the ratio of the maximum projected diameter of the deformed drop to the diameter of the initially undeformed drop; the wetted

area ratio denotes the ratio of the actual contact area between the solid and the liquid phase over the projected area of the drop. The maximum projected diameter is illustrated in Figure 23 and the spreading ratio is defined in Eq. 17. The time variation against spreading ratio is plotted in Figure 24.
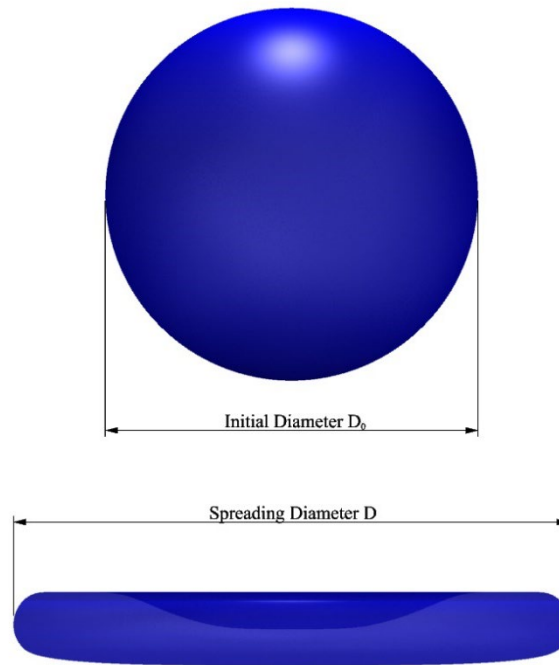
Figure 23: Illustration of the drop initial diameter and the spreading diameter. The spreading diameter is the maximum width of the drop when it is projected on a 2D plane.

The red line is the spreading ratio of the micro-well case, and the blue is the flat surface. Note that the drop takes longer to touch the micro-well surface than to touch the flat surface. As the droplet closes the orifice of the micro-well, it remains suspended inside the cylindrical cavity and the entrapped air in the micro-well prevents the drop from wetting the bottom of the micro-well. The micro-well case has a smaller spreading ratio, hence a quicker drop retraction and jump off, than the flat surface case. The jump off time for the micro-well is $t^* = 2.33$ and is $t^* = 4.76$ for the flat surface case.
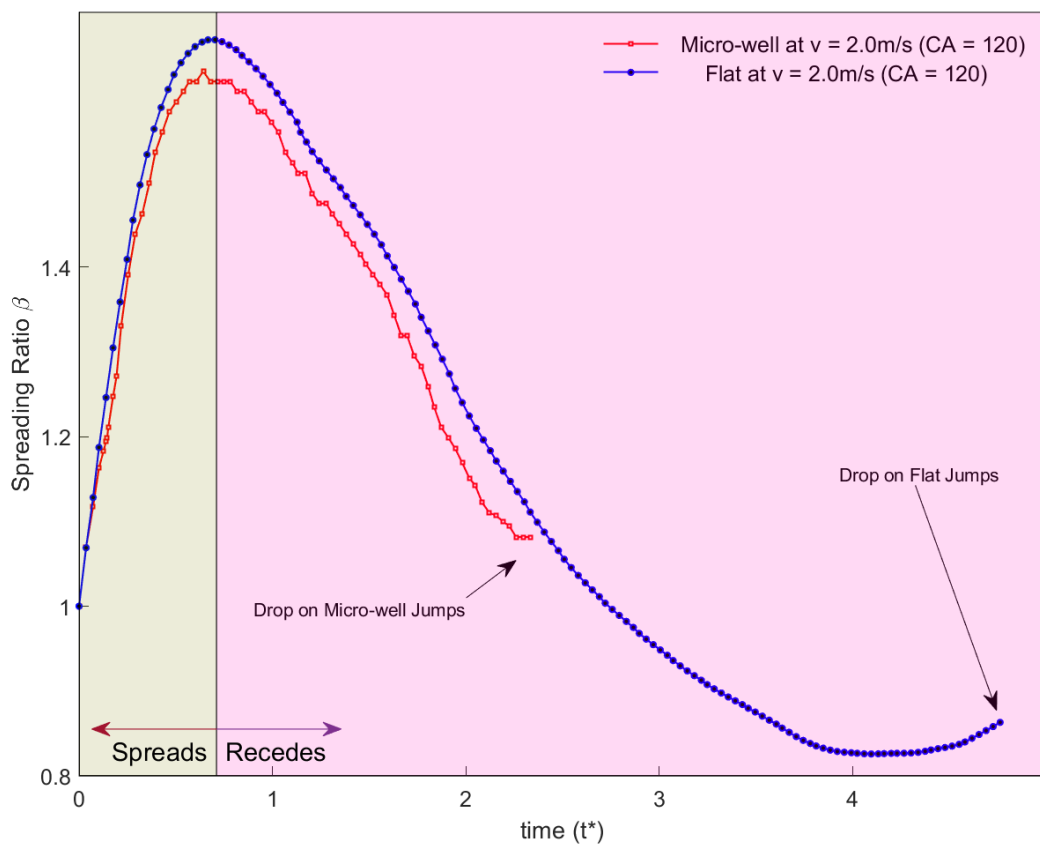
Figure 24: Time variation of spreading ratio of drop impacting on flat substrate vs micro-well substrate

To further illustrate the pertinent features of drop impact on micro-well, we present the wetting region which represents the liquid-substrate contact over time. When the drop impacts on the micro-well, it wets a small surface area than when it hits a flat surface. While the spreading ratio showed the lateral distance travelled by the droplet, the effective wetted area ratio, presented in the highlighted region in Figure 25, shows contact area between drop and substrate.

Smaller
Wetted Area

Smaller
Wetted Area

Wider Wetted Area
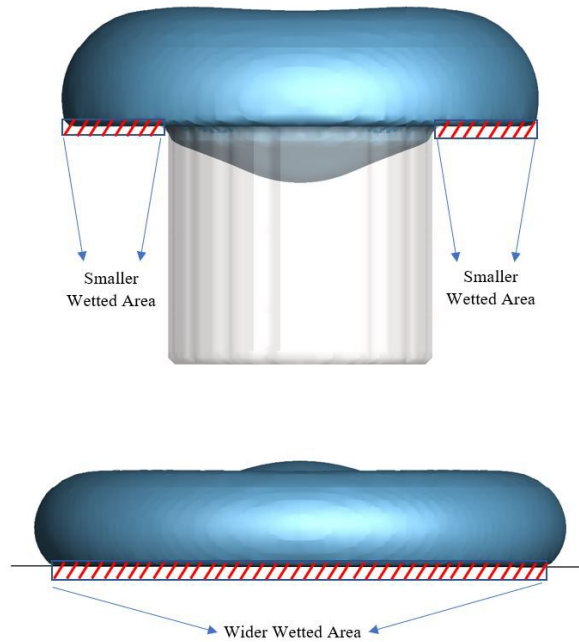
Figure 25: Comparison of wetted area: (a) Micro-well (top) vs (b) Flat surface (bottom)

The change of wetted over time is plotted in Figure 26. The drop has a 47% less wetted area in the micro-well case than in the flat surface case. Also note that the drop departs from the micro-well substrate much earlier than from the flat surface, as pointed out in the spreading ratio comparison depicted in Figure 24.
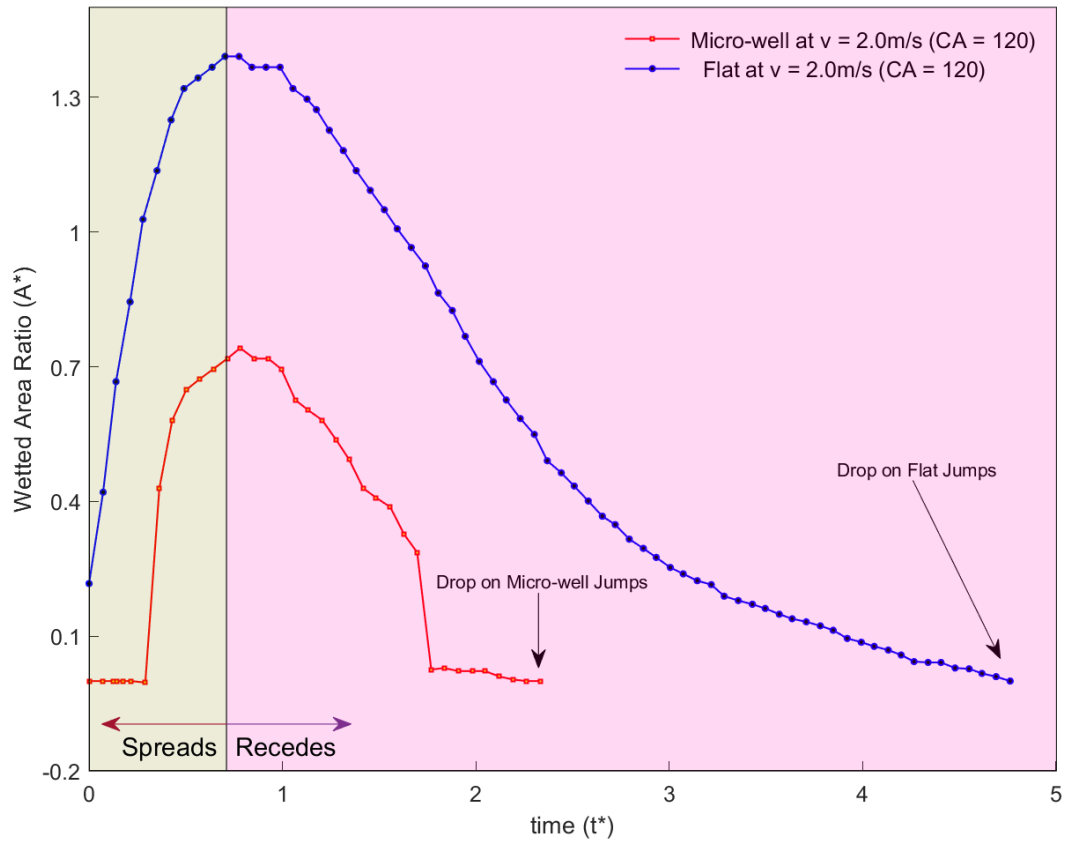
Figure 26: Resulting wetted area ratio over time

Shown in Figure 27 is the time variation of the nondimensionalized drop kinetic energy. The impact speed is 2.0 m/s and contact angle is 120°. After contacting the substrate, the kinetic energy quickly decreases to zero when the drop reaches the maximum liquid-substrate contact. As the drop starts to recede, surface energy is converted to kinetic energy and the kinetic energy starts to increase. In Figure 27, the zoom-in plot from t*=1 to t*=2 is shown as Inset A-A shows the gain in kinetic energy while the drop occurs during the drop recoiling phase. In contrast, as shown in the Inset B-B, the drop on the micro-well has already detached at t*~2.5 and jumped-off with a higher kinetic energy and the kinetic energy for the drop on the flat substrate continues to decrease, making it very difficult to

detach from the surface. The drop on the flat substrate continues to retract and the kinetic

energy starts to diminish while remaining in contact with the surface.
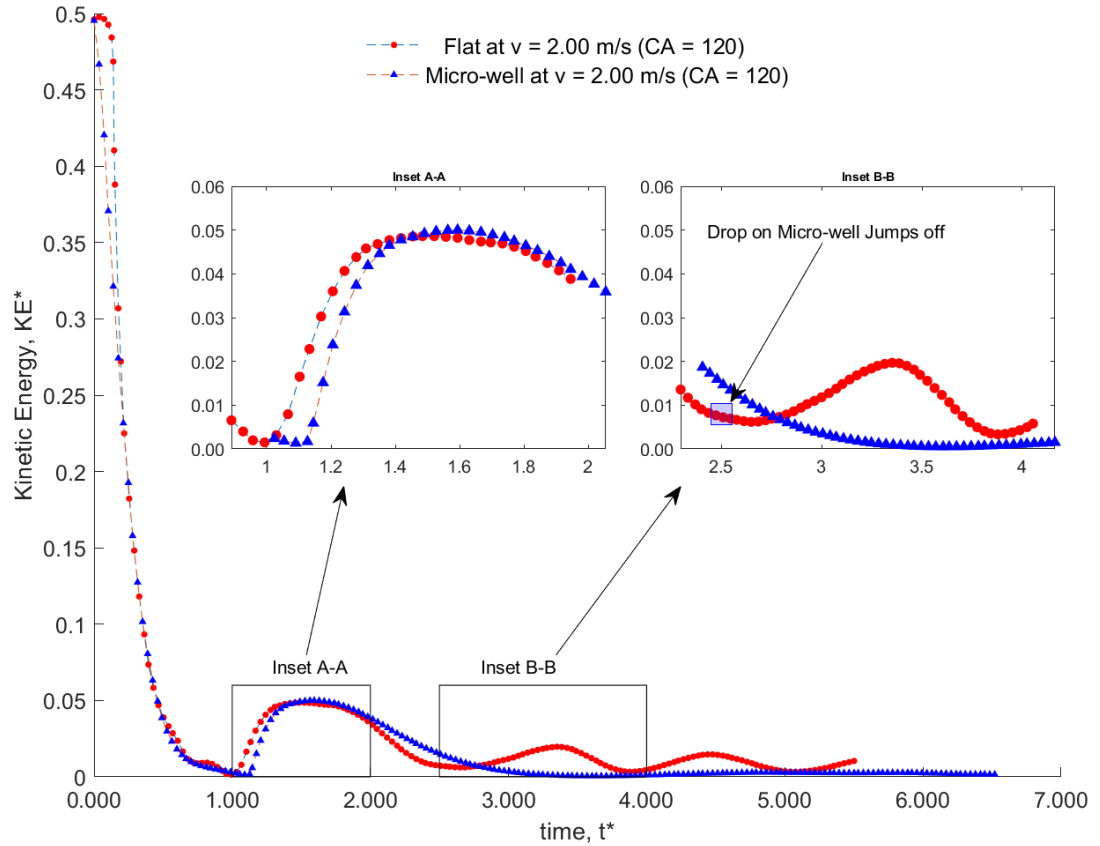
Figure 27: Kinetic Energy (KE*) in the z-direction over time for drops impacting at various speeds at contact angle of 120 degrees.

We further compare drop impact on a micro-well with drop impact on a flat substrate over

two other impact speeds of 1.7 m/s and 1.4 m/s. The results, along with that of 2.0 m/s, are

presented in Figure 28. For all the considered speeds, the micro-well case has small drop-

substrate contact areas than the flat substrate case.
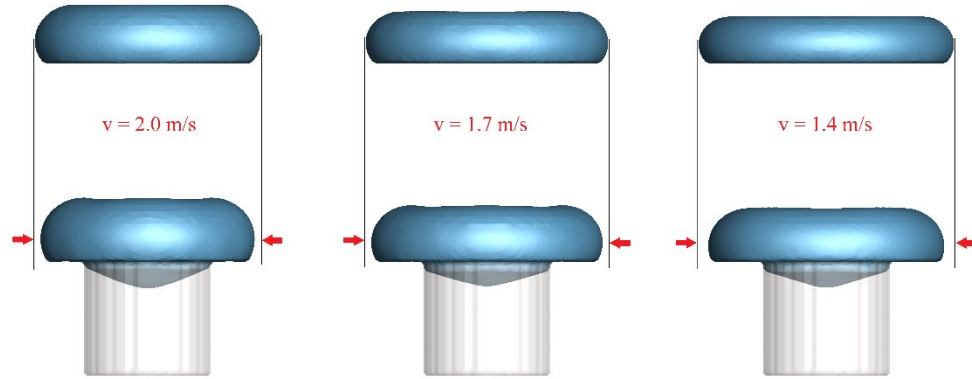
Figure 28: Comparison of the maximum spreading of drop impacting on a flat substrate (top) and a micro-well substrate (bottom) at speeds: a) 2.0 m/s b) 1.7 m/s and c) 1.4 m/s

Because the drop has smaller contact area, it is easier to jump off from the micro-well substrate than from the flat surface, as shown in Figure 29. At the impact speed of 2.0 m/s, the drop barely jumps from the flat substrate, and it does not detach from the substrate at 1.7 m/s and 1.4 m/s. In contrast, the drop jumps off from the micro-well substrate at the impact speeds of 2.0 m/s and 1.7 m/s.
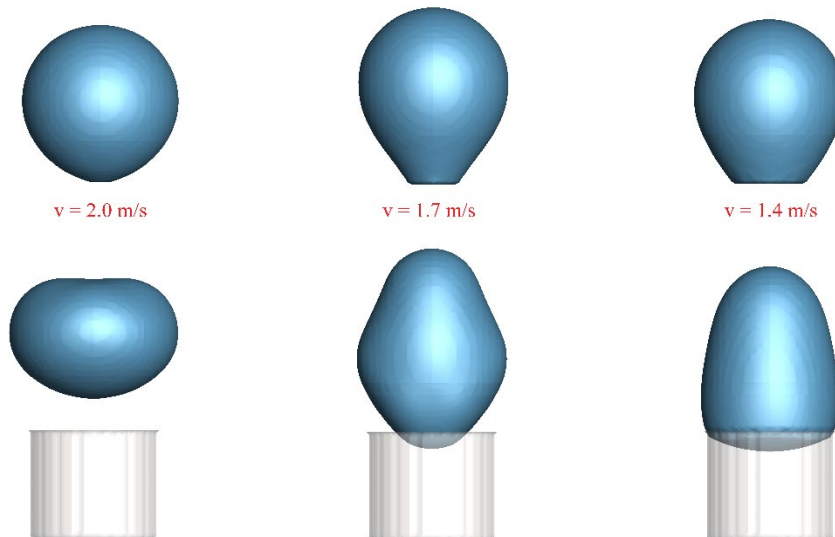
Figure 29: Drop fails to detach from a flat surface (top) but can jump off from a micro-well substrate (bottom) at impact speed of 2.0 m/s and 1.7 m/s.

Effect of Contact Angle

We simulated the effect of contact angle and the results at impact speed of 0.75 m/s. The time variation of wetted area ratio, as defined in Equation 18, is presented in Figure 30. It is very apparent that the wet area decreases with the increase of contact angle: the smallest contact angle 120° case has the largest wetted area (drop-substrate contact area), and the largest contact angle 140° case has the smallest wetted area.
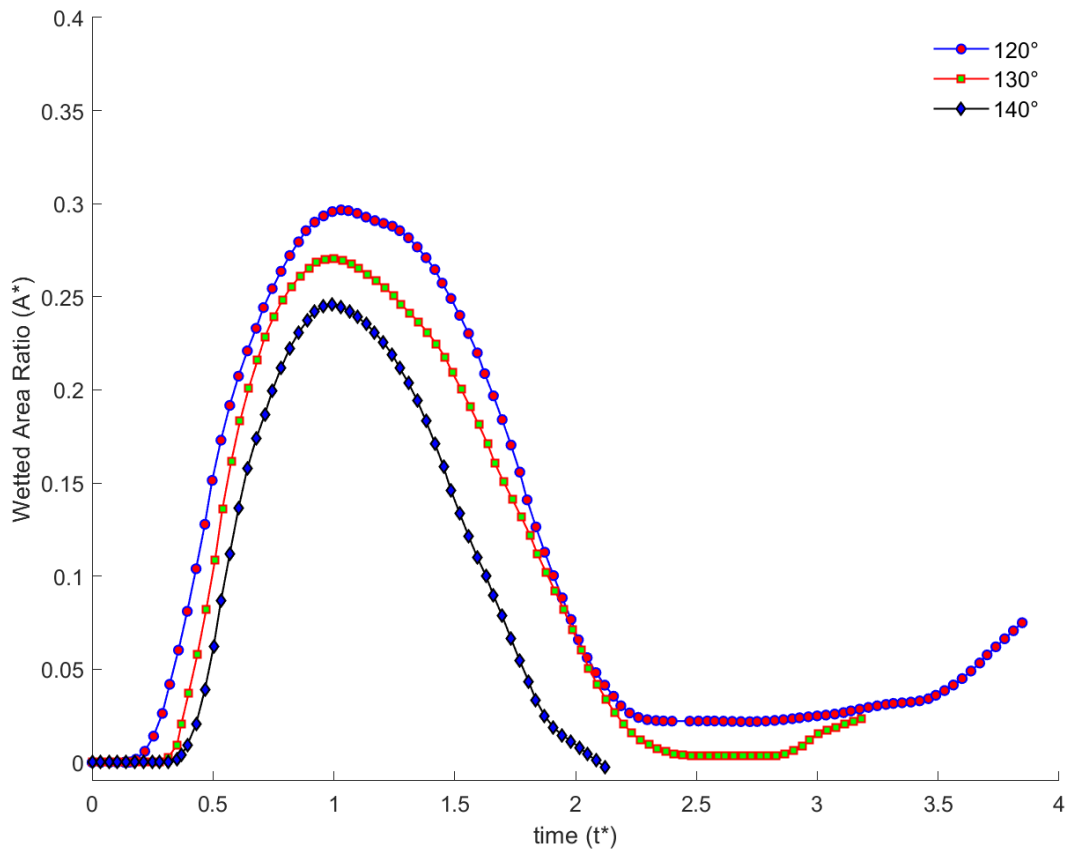
Figure 30: Impact of contact angle on wetted area for drop impact on micro-well substrate. Wetted area decreases with the increase of contact angle

The contact angle influences the degree of adhesion which in turn controls the outcome of the kinetic energy, as presented in Figure 31. At t^*= 1.25, the drop reaches the maximum spreading extent and therefore the surface tension and the viscous forces overcame the liquid inertia, it starts to recede, and this is the instance where the surface energy begins to slowly convert into kinetic energy. The largest contact angle (140°) case has the smallest contact area, and less energy is used to detach from the surface which eventually results in a reserve of higher kinetic energy. On the other hand, the smallest contact angle case (120°) has the largest contact area with the substrate and hence has the lowest kinetic energy gain. Hence, liquid-substrate adhesion dictates the kinetic energy for the drop jumping behavior on the micro-well substrate. With more drop-substrate contact, as in the case of 120°, results in less kinetic energy and the drop fails to jump and starts to spread after the initial retraction as shown in Figure 30. With smaller contact liquid-solid contact, the drop at 140°, easily detaches from the substrate and able to propel itself from the surface of the micro-well substrate.
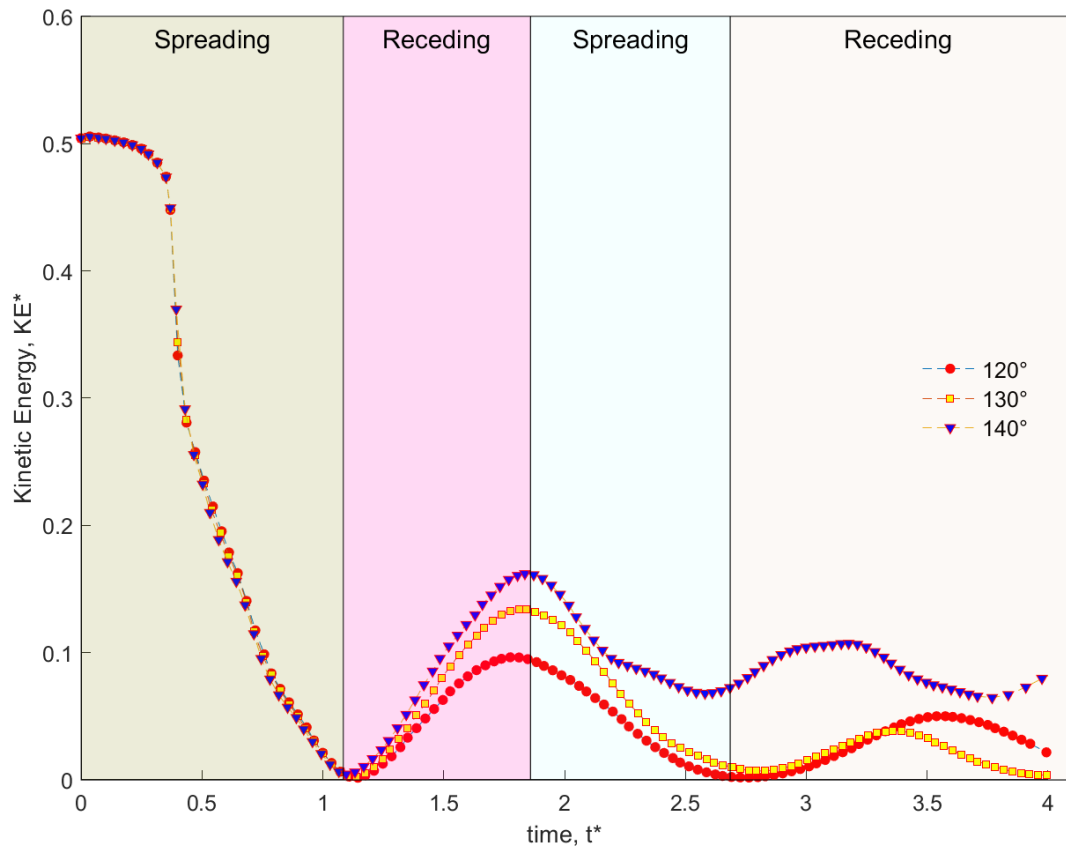
Figure 31: Kinetic Energy (KE*) in z-direction over time for drops impacting at a speed of v =0.75 m/s at a contact angle of 120°, 130°, and 140°

Drop Jumping Regime-Map

Using the simulation results from different contact angles and impact speeds, we can qualitatively construct an impact velocity-contact angle jumping regime map, which entails the advantage of micro-well over a flat surface substrate and is presented in Figure 32. It is evident that the micro-well jumping boundary is larger than the jumping boundary of flat substrate.
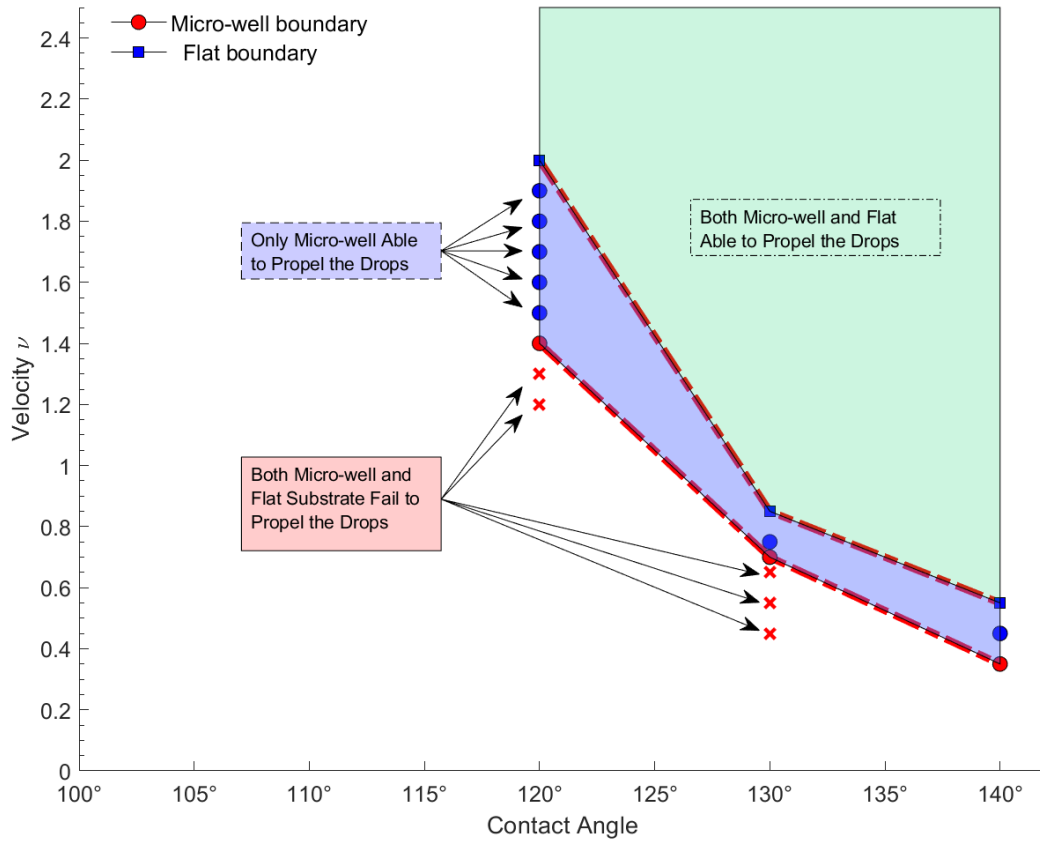
Figure 32: Regime map showing the ability to propel drops on micro-well and flat substrate.

We will further rationalize the ranges of the drop impacting and rebounding for all three contact angles presented in Figure 32. For the contact angle of 120°, when the impact speed is lower than 1.4 m/s the drop fails to detach from the flat surface and micro-well surface. When the impact speed is between 1.4 m/s and 2.0 m/s, the drops can propel away from the micro-well substrate but not the flat substrate. When impact speed is larger than 2.0 m/s the drop can detach from both the flat and micro-well substrates. In the case of 130°, when the impact speed is between 0.7 m/s to 0.85 m/s the drop jumped from the micro-well substrate but not from the flat substrate. When impact speed is smaller than 0.7 m/s,

the kinetic energy does overcome the inter-surface adhesion forces in either case and the drop does not detach from the substrate. At the contact angle of 140°, the jumping threshold on the micro-well substrate is more skewed than in the case of 130°. At speed of 0.35 m/s to 0.55 m/s drop is able to propel out of micro-well surface but fail to detach from the flat substrate. At the impact speed is 0.55 m/s the drop can jump off from both the micro-well and flat substrates.

Finally, we present three different cases of speeds at which the drop either a) jumps from both substrates, b) jumps off from the micro-well but not from the flat substrate, or c) fails to propel from both substrates. Figure 33 presents the case of 120° contact angle where impact speed of i) 2.0m/s, ii) 1.7 m/s, and iii) 1.3m/s shows the overall advantage of the micro-well substrate over the flat substrate encompassing a wider range of impact velocity scenarios.
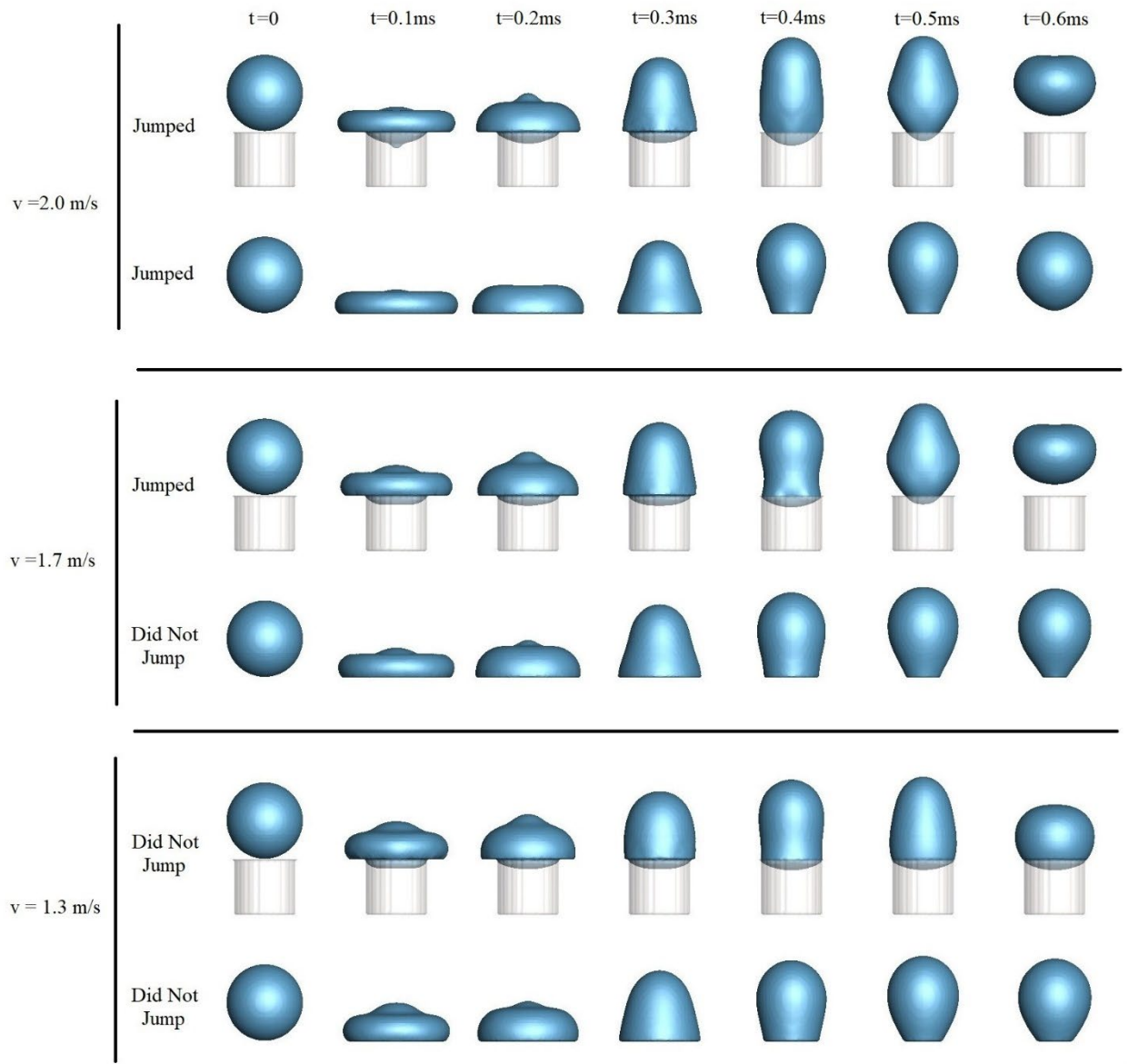
Figure 33: Drop impact on micro-well vs flat at a contact angle of 120°: Different instances of jumping and non-jumping off the substrate

Drop impact on a substrate with patterned micro-wells

Substrates with cylindrical or square micro-pillars are often used to represent rough surfaces. As discussed earlier, air pockets within the pillars can prevent the drop from reaching the bottom of the substrate and thus reduces the solid-liquid contact area[147, 159, 160]. However, air can escape through the gaps of the micro-pillars (illustrated in Figure 34) and a complete state of non-wettability is hard to achieve[148]. In this section we demonstrate that a non-wettability can be achieved on a surface with an array of multiple micro-wells.
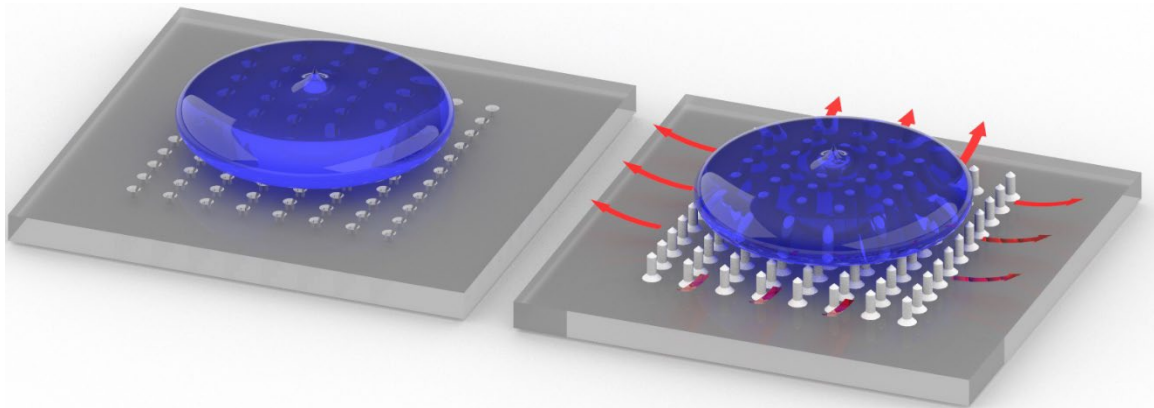
Figure 34: Difference between micro-well substrate (left) and micro-pillar substrate (right). Air is trapped in the micro-wells under the drop but air escapes in the micro pillar configuration

Figure 35 shows the simulated results of drop impingement on a surface with micro pillars. The drop is released at an initial speed of 1.57 m/s, resulting a Weber number of 50. Almost half of the drop volume sips through the micro-pillars at 0.6 ms.
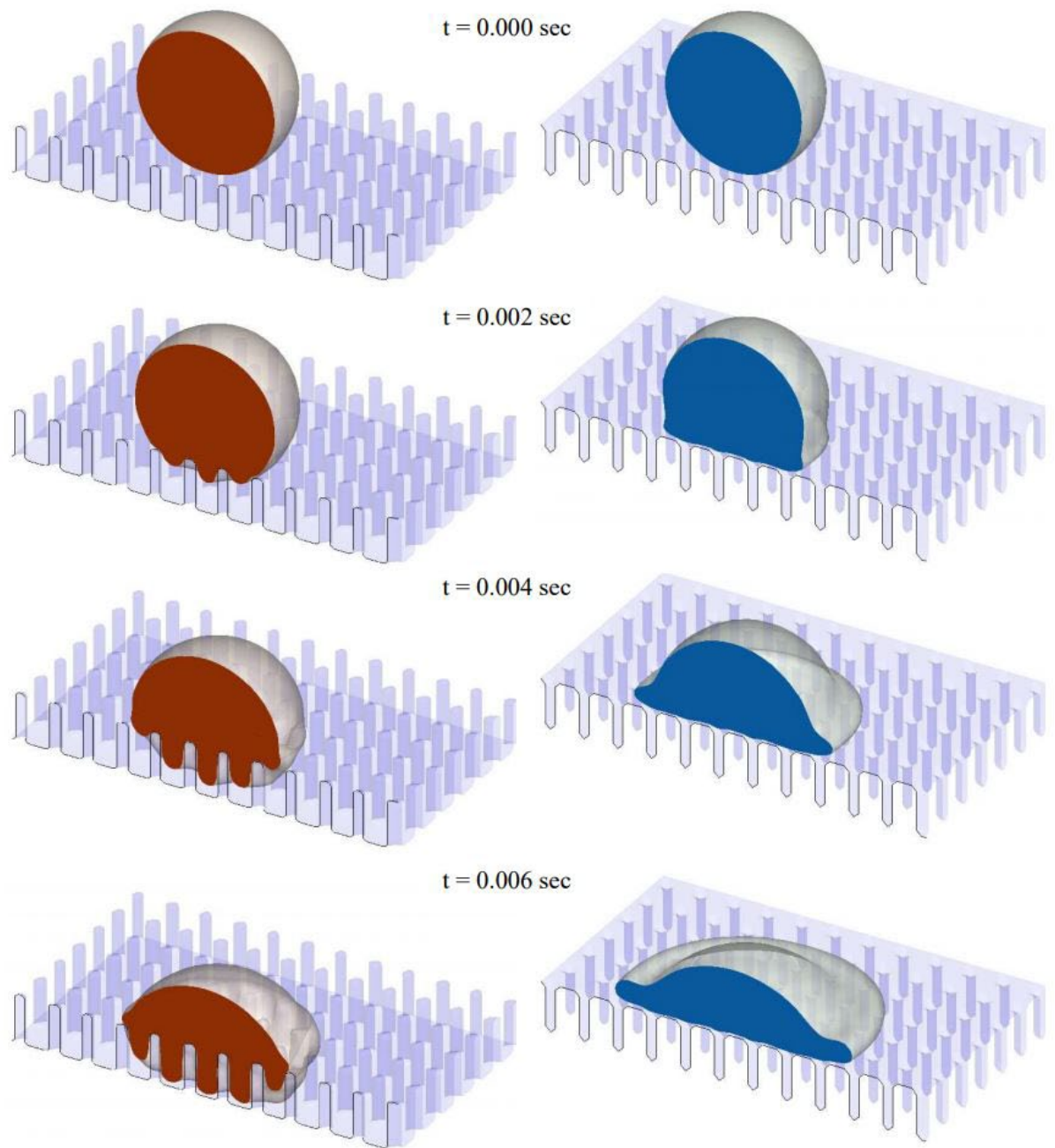
Figure 35: Drop impact on a micro-pillar surface (left) and on a micro-well surface (right). The drop completely wets the pillar surface but only partially wets the micro-well surface .

Velocity streamline drawn in Figure 36 shows that the air escapes through the gaps

of the micro-pillars whereas the streamlines do not pass through the pores of the micro-

wells. The micro-well substrate remains almost dry with a very minimal liquid-substrate contact and a complete wetting scenario is thus prevented.
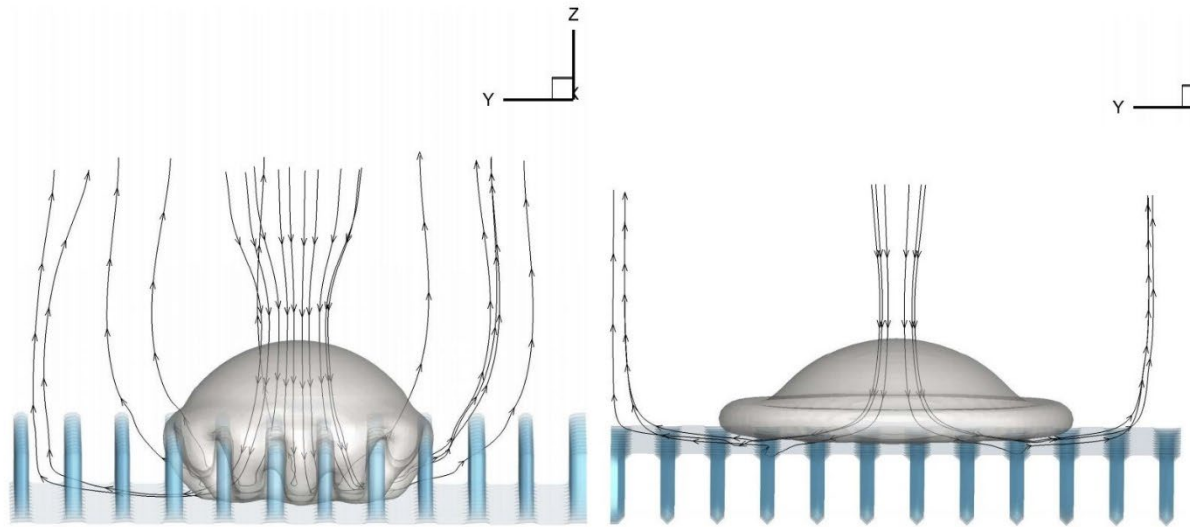
Figure 36: Streamlines showing the air escaping through the substrate: micro-pillars (left) vs micro-wells (right)

CHAPTER V
DROP IMPACT ON LIQUID-INFUSED MICRO-WELL SUBSTRATE*

Ice accumulation on aircrafts[20, 161-163], power lines[164, 165], wind and gas turbines[166, 167] and many types of other infrastructures[168] have been long studied because of the associated complexity that arises due to the growing cost and the time consumed to solve such a problem. In the natural environment, ice formation is largely contributed by impingement of supercooled large droplets (SLD) and such water droplets are at temperatures below the freeing point. And since the impinging drops have different impact dynamics, studies[169] point out to two critical approaches to deal with these scenarios: 1) reducing contact time and promote quick removal/repelling of contacting drops and 2) delaying post impact nucleation by combining surface chemistry and topographical features which may involve the use of additional high performance measures, such like infusing lubricants known as LIS/SLIPS.

The use of chemical compounds as an icephobic treatment are generally of two types: 1) sacrificial, where treatments may consist of lubricants such like oil/grease, gel that can slowly deplete over time and 2) permanent, where special type of icephobic coating may be used and would not degrade over time. Besides water and ice repellency, LIS/SLIP substrates have shown to have anti-fouling characterization[170-172], pronounced heat transfer ability due to dropwise condensation stemming from extremely low contact angle hysteresis and high mobility[38, 173-176].

As discussed before in the earlier chapters, the key in designing of superhydrophobic structures is to design substrates with air-entrapping porosity that utilizes the concept of Laplace pressure which in turn dictates the reduced surface wetting property. Reduced snow and ice accumulation/nucleation, delayed ice formation and weakened ice adhesion[33, 34, 177-180] at very low temperatures of -25C to -30C[181, 182], on one hand have made superhydrophobic substrates to be very appealing for icing researchers. On the other hand, many other studies have argued and discredited superhydrophobic surfaces to be practically ice-phobic[183]. While some researchers have raised issues with scalability arising from high temperature and high-speed impingement, others pointed out that the propensity to form condensate eventually closes the pores containing air pockets, and therefore readily degrades icephobic property[184, 185]. Regardless of the climatic and design limitations of the superhydrophobic substrates for icing conditions, the Laplace pressure still holds the key in designing substrates with ice accretion, formation and locking capability. In the case of oil-infused surfaces, the design of the substrate texture is vital for holding lubricant via increment of the Laplace pressure and, therefore, boosting the pressure resistance of the surface[186]. SLIP/LIS can retain

their water repellency properties at a significant pressure (~ 676atm) stability[187] and remains frost free with an order of magnitude lower ice adhesion and proven to have excellent performance on adverse icing conditions[32, 188-194]. Ice-phobicity can be classified as substrates that characterizes in repelling supercooled droplets at temperatures that are below freezing point[195], delayed formation of heterogenous ice nucleation[196], and with reduced shear strength within the range of 150kPa to 500kPa [197]. When it comes to the surface roughness that inhibits wetting and icing, surfaces are generally classified as regularly ordered patterned, or irregularly distributed surface texture. Ice adhesion on square micro-posts having varying periodicity and covered with lubricant film was experimentally studied by Subramanyam et al[198]. They predicted that ice adhesion strength reduces with increased surface hydrophobicity which in turn increases with stable lubricant layer trapped within surface texture density. Nanorods[199], and nanostructures of butterfly wings[200] are also examples of roughness induced superhydrophobic (SH) substrates that are found to be water repellent and efficient at retarding ice formation.

Drop pinning, shedding, viscous dissipation and sliding velocity are also found to be highly dependent on the contact line dynamics of four phase system of a lubricant-impregnated substrate that has patterned micro-post arrays[174]. Highly dense textures have found to be able to reduce droplet pinning, and thus achieve roll-off angles of fully wetting lubricants, synonymous to the Cassie state of a superhydrophobic substrates. Some other studies wanted to increase friction with the liquid drop and a stabilized layer of lubricant, and has successfully utilized the use of micro-pillars coated with hydrophobic nanobeads[201]. It was also found oil infused micro-textured flexible polydimethylsiloxane(PDMS) substrate does significantly influence the water repellency

and ice adhesion strength over smooth micro-texture substrate with no oil-infused lubricant, as demonstrated by Yeong et al[202]. Some other examples of excellent liquid repellant and reduced wettability of SLIP induced with silicon dioxide SiO_2, PMMA and THF nanoparticle surfaces was produced by Wang et al[203]. Droplet sizes of 5+0.2 µL impacting at approximately 1m/s of different types of liquid, including hexane, kerosene, diesel oil, water and milk showed superior non-wettability compared to superhydrophobic substrates. Lubricant infused surfaces are also discovered to be able to manipulate impacting droplets, control sliding behavior and directional rebound[204], and produce inelastic collision of impacting water flow[205].

Lubricant infused regular and semi-random textures and the drop mobility study were performed by Schellenberger et al[206], where micro-pillars were made by spin coating hydrophobic dye and photolithography and randomly distributed opal textures were hydrophobised by chemical vapor deposition. Their study has produced critical insights regarding the height and range of wetting ridge formation[173], and the evolution of cloaking layer of deposited drops on different lubricant types. Due to limitation of field view, this particular study failed to measure the exact cloaking height, and suggested van der Walls estimation (using the Hamaker constant, A_H = 6e-21J) to estimate the thickness to be ~20nm forming on the drop having a radius of 1mm. Cloaking behavior is seen to be controlling the size and distribution of condensate droplets, and also contributes in accelerating the oil depletion from porous substrates[173, 207]. Similar to cloaking, thin lubricant layer of microscopic oil film between two drops can momentarily prevent coalescences[208].

Lubricant properties, such like surface tension[39, 173, 174, 198, 206], and viscosity[196, 209, 210] needs careful attention when designing LIS/SLIP substrates, because such factors play crucial role in droplet cloaking which can accentuate the lubricant depletion, and possible contamination. An important contribution to understand the nature of the cloaking behavior is to understand the implication of spreading co-efficient due to interfacial tensions of different fluid-lubricant combinations. Sett et al. exploited the idea of the statistical thermodynamic model[211-213] and utilized the shape of a pendant drop[214] to create a combination of a large dataset of possible working fluids (such like water, alcohols, alkanes, etc.) and the lubricants (Krytox, silicone oil, etc.) that are critically immiscible and possibly prevents cloaking. A similar study performed by Preston et al.[215] successfully produced a comprehensive design guideline for a lubricant-substrate combination that would avoid cloaking phenomena and could repel very low surface tension liquids such like butane (surface tension ~13 mN/m). As pointed out by Weisensee et al. [38], besides cloaking, shear-induced drainage of low-viscosity lubricant is much quicker and less stable than high-viscosity lubricants. Also, using superhydrophobic nanoparticles, nanowires and microposts, researchers found that lubricant drainage into growing network of nanoicicles reduced the anti-icing capability during repeated frosting-defrosting cycles[216]. Oil migration due to capillary forces occurred from the wetting ridge and the substrates surface to the frozen drops, and it was suggested that a better liquid-texture combination needed to design a sustainable LIS/SLIPS substrate that can prevent frost growth.

Contact Angle Modelling: Capturing Cloaking and Wetting Ridge Formation

Due to the presence of 4 different materials in the domain, namely water, lubricant, vapor and the solid, a special treatment is needed to correctly construct the contact line dynamics for the drop impact studies. But before we delve into four phase/material case, we highlight and explain the general wettability relationship of three-phase state below.
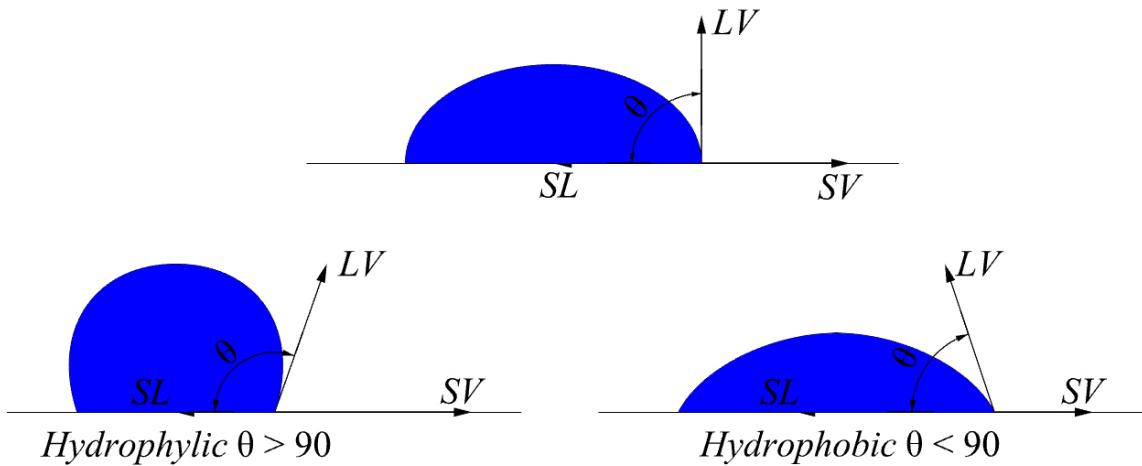
Figure 37: Drop Deposition showing the difference between Hydrophilic and Hydrophobic States

For a typical contact line where only three material is present (water droplet (L), the solid substrate(S), and the surrounding air phase(V)), the general Young's equation can be written,

$$\sigma_{LV} \cos(\theta) + \sigma_{SL} = \sigma_{SV} \tag{56}$$

This equation typically denotes the equilibrium state which is where the surface tension of the three phases forms a junction of the three-phases, and the droplet comes to rest after oscillation. The wetting behavior of a substrate, based on Young's equilibria equation, thus

defines that a drop on a high surface energy state would stick to the surface (hydrophilic, $\theta < 90$) and a low surface energy state would repel the water droplet from the surface (hydrophobic, $\theta > 90$).

In the nature and many experimental studies inspired by the nature, where a drop may jump or splash, depending on the impact energy, the kinetic to surface energy exchange, and various other factors, the Young's model does not represent the correct morphology of the drop dynamics (spreading, retraction, jumping, etc) and hence there are contact line models that are proposed to compensate such difference. A common approach needed to describe the droplet dynamics is by further utilizing the concept of the advancing angle, θ_A and the receding angle, θ_R. As it could be easily understood by the terminology, the advancing angle is the formation of the angle at the three-phase triple point while the droplet is in spreading motion, and the receding angle is formation of the angle while the droplet is in receding motion, as shown in the following Figure 38.
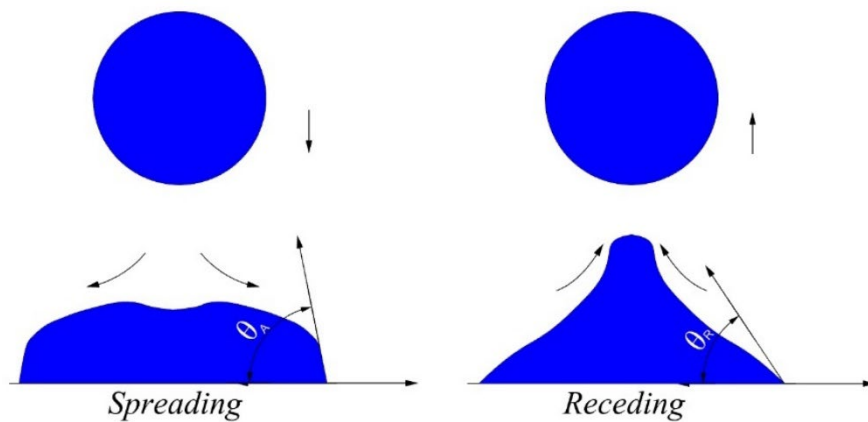
Figure 38: Spreading showing the Advancing Contact Angle (left) Receding showing the Receding Contact Angle (right)

The advancing angle is higher than the receding contact angle, and this is due to the adhesion and the involvement of capillary forces caused by the interfacial tensions between

the liquid and the solid phase. Again, in the nature, the difference between the advancing and the receding contact angles is very much existent, and such difference is known as the contact angle hysteresis, $\Delta\theta = \theta_A - \theta_R$. Researchers and scientists therefore coin the concept of hydrophobicity or liquid repellant properties from the idea of air-entrapment at microscopic level. It is commonly understood that roughness characteristics are the key design parameter that can entrap air, and thus provide a barrier between the liquid-solid phases and this leads to the hydrophobicity of a designed surface. Contact angle hysteresis (CAH) can explain a droplet's mobility and accounts for the dynamics of the events of spreading and retracting which happens due to the entrapment of air in rough substrate. In other words, rough substrate that can entrap air (also known as Cassie-Baxter state) or impalement where the liquid replaces the air pockets (also known as Wenzel state), can therefore be directly accounted due to the roughness factor, R_f of the substrate. The roughness factor is the ratio of an actual surface area to the projected area and defines the coarseness of a given substrate. For impalement the Young's relationship of the Wenzel State could be written as,

$$\cos \theta_W = R_f \cos \theta_E \tag{57}$$

where the θ_E is the Young's equilibrium angle. The relationship of the Cassie-Baxter state is written as,

$$\cos \theta_{CB} = R_f \cos \theta_E * \phi - (1 - \phi) \tag{58}$$

where ϕ is the solid fraction of the substrate that is in contact with the liquid and $(1 - \phi)$ is the air fraction of the substrate.

Now that we have explained the drop repelling mechanism of a rough substrate that entraps air resulting in a superhydrophobic nature of a substrate, we use the same mechanism but replace air-pockets inside the pores of the surface with lubricants.
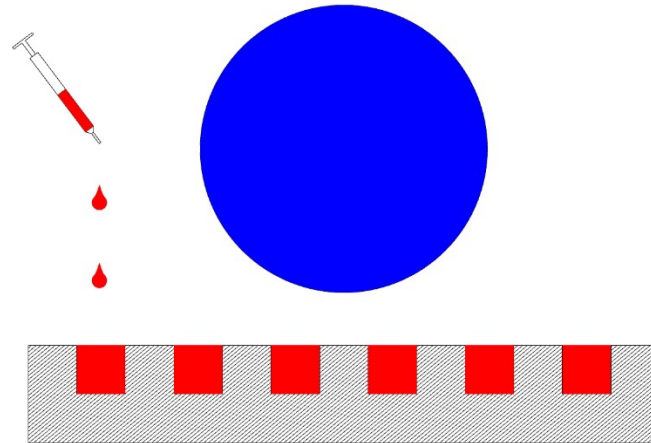
Figure 39: Lubricant Infused Micro-well

There lies a significant difference in the interaction mechanism of water droplet with air and water droplet with lubricant. This difference becomes crucial when the liquid water droplet is in a dynamical system (such like a drop impact, splashing, sliding, etc) or in an equilibrium resting position (such like a condensation or SLD freezing-recalescence).

In the ideal sense of lubricant impregnated surfaces for droplet repulsion and anti-icing capability, the two liquids must be immiscible. And in the case of immiscible liquids, there lies another problem, which is the cloaking, as described earlier in the literature survey. Cloaking is dependent on the interplay between the surface tensions of different liquids, and therefore occurs when low surface energy lubricant spreads and covers a high-surface-energy liquid, such as a water droplet. Wetting ridge or skirting is another factor that readily occurs in the presence of the three immiscible liquid forms and is also highly dependent on the interfacial tensions of each phases/material.

66

To account for such mechanism in a quantitative manner, researchers have proposed what is known as spreading factor (sometimes also known as spreading co-efficient) for with and without lubricant impregnated substrate (L_1 indicating water, and L_2 indicating lubricant/oil) as follows,
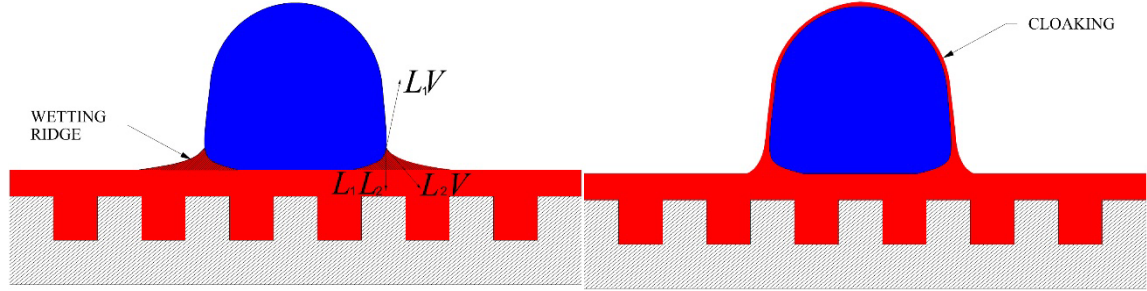
Figure 40: Wetting Ridge (left) and Cloaking (right)

Without Lubricant:

$$S_{L_1S} = \sigma_{SV} - \sigma_{SL_1} - \sigma_{L_1V} \tag{59}$$

With Lubricant:

$$S_{L_1L_2} = \sigma_{L_1V} - \sigma_{L_2L_1} - \sigma_{L_2V} \tag{60}$$

A positive spreading factor indicates that the low surface energy lubricant will cloak and cover the high surface energy water droplet with a thin layer of lubricant. Smith et al. [174] constructed the interfacial and energy based relationship of a liquid droplet and lubricant impregnated substrate of six different configurations. In case of drop impact and mobility, *our interest lies* on three of the configurations that are underneath and right next to the droplet and having an interfacial relationship with the lubricant, namely: 1) Impaled 2) Impregnated, emerged 3) encapsulated.

 Smith et al. proposes the following energy exegesis based on the three configurations:

Table 3: The Interfacial energies per unit area for three configurations

	Configuration	Total interfacial energy per unit area
W1	Impaled	$E = R_f \cdot \sigma_{L_1S}$
W2	Impregnated, emerged	$E = (R_f - \phi) \cdot \sigma_{L_2S} + f\sigma_{L_1S} + (1 - \phi)\sigma_{L_1L_2}$
W3	Encapsulated	$E = \sigma_{L_1L_2} + R_f \cdot \sigma_{L_2S}$

And the spreading co-efficient could be related in the following manner:

Table 4: Spreading Coefficient Relationship of the three configurations

	Configuration	Spreading Coefficient Relationship
W1	Impaled	$S_{L_2S} < -\sigma_{L_1L_2} \cdot \dfrac{R_f - 1}{R_f - \phi}$
W2	Impregnated, emerged	$-\sigma_{L_1L_2} \cdot \dfrac{R_f - 1}{R_f - \phi} < S_{L_2S} < 0$
W3	Encapsulated	$S_{L_2S} \geq 0$

W1-Impaled

W2-Impregnated-Emerged
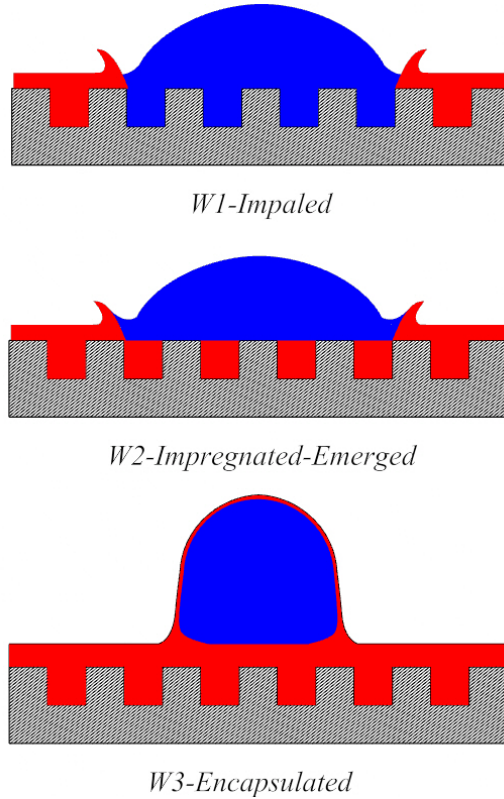
W3-Encapsulated

Figure 41: From to Bottom: Possible Configurations of Liquid Drops on SLIPS: W1 - Impaled; W2 - Impregnated-Emerged; W3 - Encapsulated

As shown through the three configuration settings, that surface (interfacial) tension, roughness factor, and the liquid(L_1)-lubricant(L_2)-surface(S) contact are all the factors that can dictate the dynamics of the droplet, and equilibrium state after the droplet settles onto the SLIP/LIS surface. In terms of SLD involving the aircraft icing physics, the droplet are eventually shed at different operating conditions, and the lubricant attached via means of cloaking or formation of wetting ridge is therefore lost in the process. Therefore, an appropriate modelling of contact angle is needed to 1) reconstruct the cloaking behavior 2) reconstruct the wetting ridge that also involves a moving triple-point, and 3) understand the reasoning and differences in cloaking behavior and wetting ridge heights and lengths

in the case of a droplet dynamics (impact, retraction, possible jump off, or oscillatory behavior of the droplet, etc).

In case when the solid is in contact with either of the liquid, that is the lubricant or the water droplet, we apply the following conditional equation in the computation cell (i,j),

if

$$\phi_{solid}(i, j) \geq 0$$

$\rightarrow$ do nothing

else if

$$\phi_{solid}(i, j) < 0$$

$\rightarrow$ let m_1 be the primary fluid material

$\rightarrow$ let m_2 be the next closest fluid material

$\rightarrow$ determine 3rd ranking material:

If m_3 is the solid $\rightarrow$ use static contact angle calculation as described earlier

If m_3 is a fluid $\rightarrow$ use triple point method .For the definition of the triple phase (without the solid fraction) similar to the Neumann triangle method, the following relationship can be constructed,

$$\cos \theta_{L_1 L_2 \angle L_1 V} = \frac{\sigma_{L_2 V}^2 - \sigma_{L_1 V}^2 - \sigma_{L_1 L_2}^2}{2\sigma_{L_1 L_2} \sigma_{L_1 V}} \tag{61}$$

$$\cos \theta_{L_1 L_2 \angle L_2 V} = \frac{\sigma_{L_1 V}^2 - \sigma_{L_2 V}^2 - \sigma_{L_1 L_2}^2}{2\sigma_{L_1 L_2} \sigma_{L_2 V}} \tag{62}$$

$$\cos \theta_{L_2 V \angle L_1 V} = \frac{\sigma_{L_2 L_1}^2 - \sigma_{L_1 V}^2 - \sigma_{L_1 V}^2}{2\sigma_{L_1 V} \sigma_{L_2 V}} \tag{63}$$

A detail discussion on how to calculate the surface tension forces for cases involving more than two materials are presented earlier in the numerical section.

Computational Domain Setup for four materials (air, water, lubricant and solid)
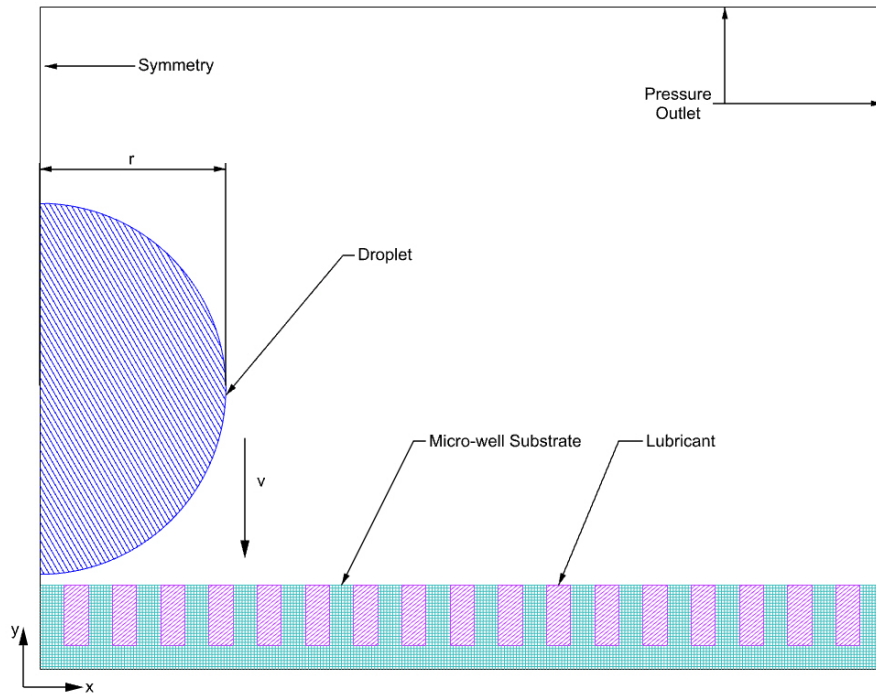
Figure 42: Computational Domain for Drop on SLIP Substrate
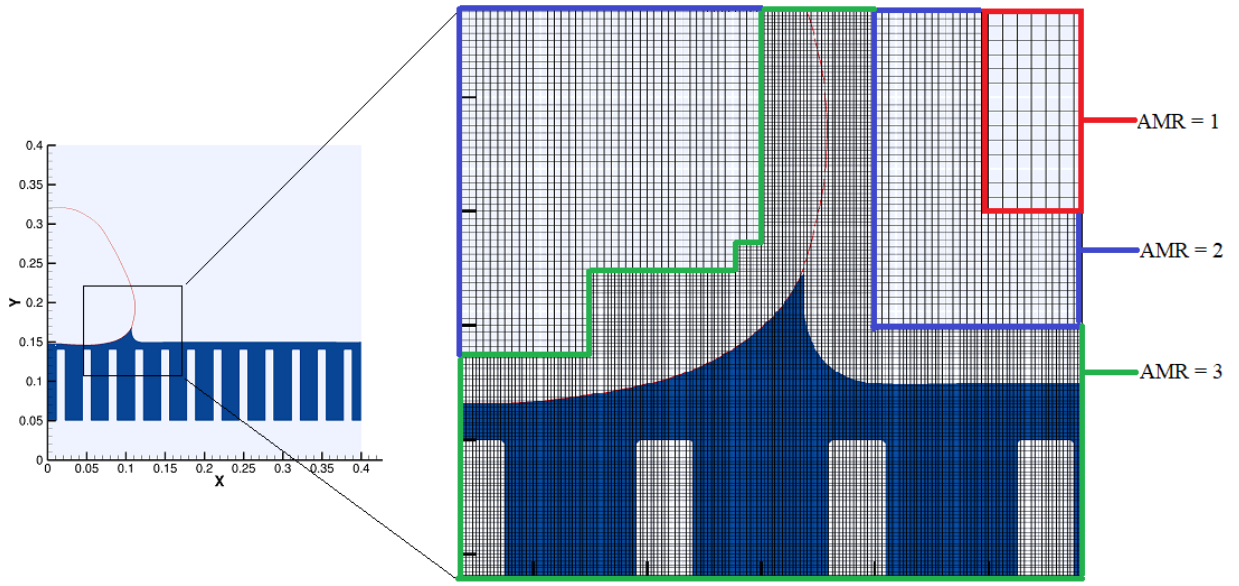
Figure 43: Drop Impact on a SLIP/LIS Substrate: Showing AMR=1, AMR=2, and AMR=3

For the droplet impact on lubricant-infused case, we at first systematically vary the surface tension values, while holding the viscosity and density values constant. For the purpose of initial droplet-lubricant interaction bench studies, we consider Krytox GPL 101. Krytox oil is based on perfluoropolyether (PFPE) and is considered as long lasting non-reactive lubricant type. Typically, the temperature range for Krytox GPL 101 is between -70C to 105C, sometimes considered for their effective anti-icing properties. For the two-dimensional simulation study, as shown in the Figure 42, the domain has symmetrical boundary on the left, which therefore divides the droplet into half, and thus reduces computation time and resources. The top and the right side of the boundary uses pressure outlet, and the bottom is set as a wall boundary condition. The grid refinement uses the adaptive mesh refinement with three levels (AMR = 3) where any moving fluid interface and liquid-solid interface has the highest refinement region, as shown in Figure 43.

For the next part of study, we intend to completely capture the cloaking phenomena of the entire droplet but relate them to the impact speed of the droplet. We limit the cases to three particular cases where are varying the interfacial tension forces of lubricant-air, L_2V, to achieve a diminishing interfacial tension between lubricant-water, L_1L_2, that gives us the spreading coefficient, $S_{L_1L_2}$, required to capture the cloaking phenomena of a water droplet. Spreading coefficient is defined as $S_{L_1L_2} = \gamma_{L_1V} - \gamma_{L_2V} - \gamma_{L_1L_2}$ and should be positive for cloaking or encapsulation of water droplet by the lubricant medium. The following interfacial tensions between the lubricant and water are simulated in our study:

Case no.	$\gamma_{L_1L_2}$ (mN/m)	γ_{L_2V}m (mN/m)	γ_{L_1V}m (mN/m)	$S_{L_1L_2}$	Cloaking
Case 1	51.32	28	72.7	< 0	No
Case 2	31.79	23	72.7	> 0	Yes
Case 3	21.73	18	72.7	> 0	Yes

Slow Speed Cases to Capture Cloaking and Variation in Spreading

For initial cases of varying interfacial tensions, we consider two impact speeds for the water drops, namely impact speed of v = 0.25m/s and v = 0.5m/s.
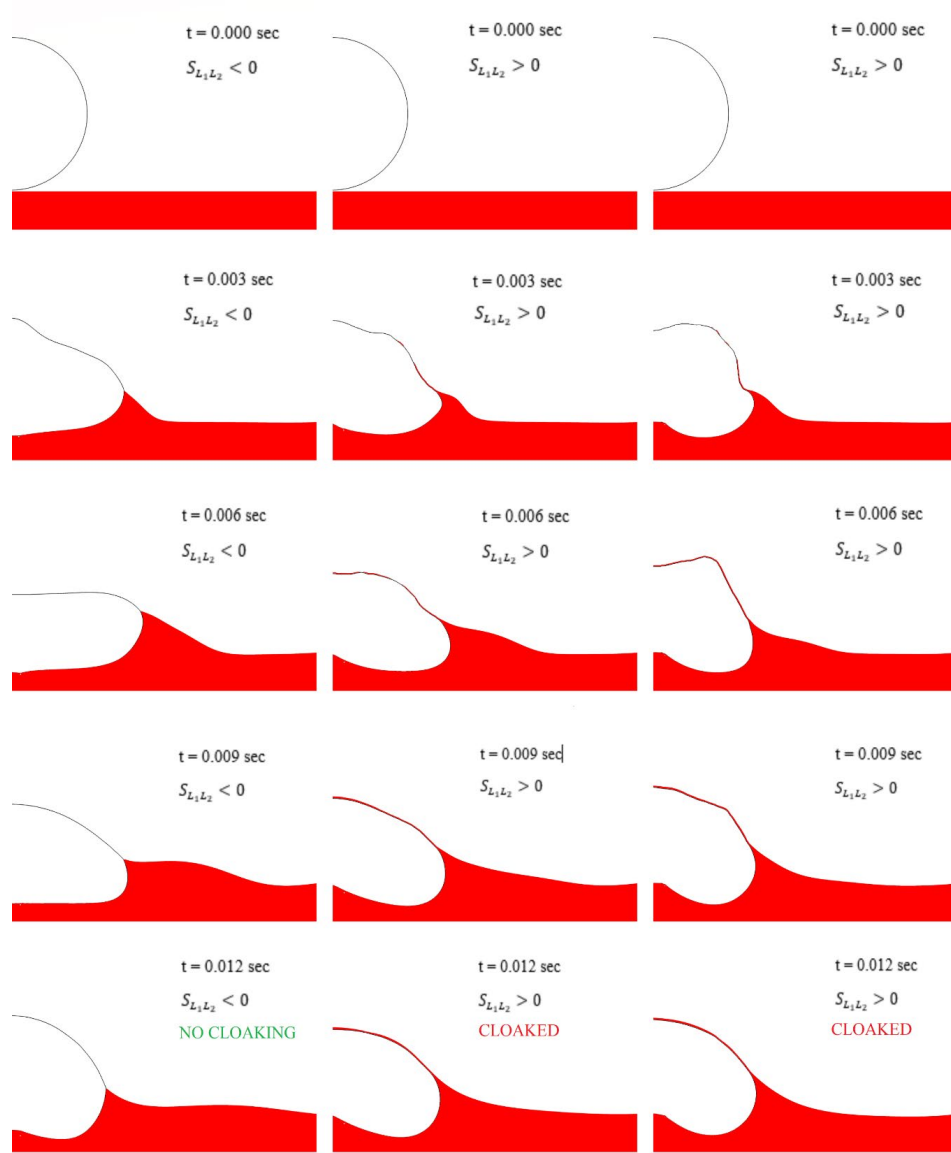
Figure 44: Drop impact speed of v = 0.25m/s on varying interfacial tensions and cloaking phenomena: from left to right: a) Case 1 - $\gamma_{L_1L_2} = 51.32 \, mN/m$; b) Case 2 - $\gamma_{L_1L_2} = 31.79 \, mN/m$; c) Case 3 - $\gamma_{L_1L_2} = 21.73 \, mN/m$;

Figure *44* shows the impact cases for v = 0.25 m/s and Figure *45* shows the impact case for v = 0.5 m/s. For all three cases the drop spreads and retracts and there remains a variation of spreading width or the maximum travel of the outer edge of the drop based on different interfacial tension cases.
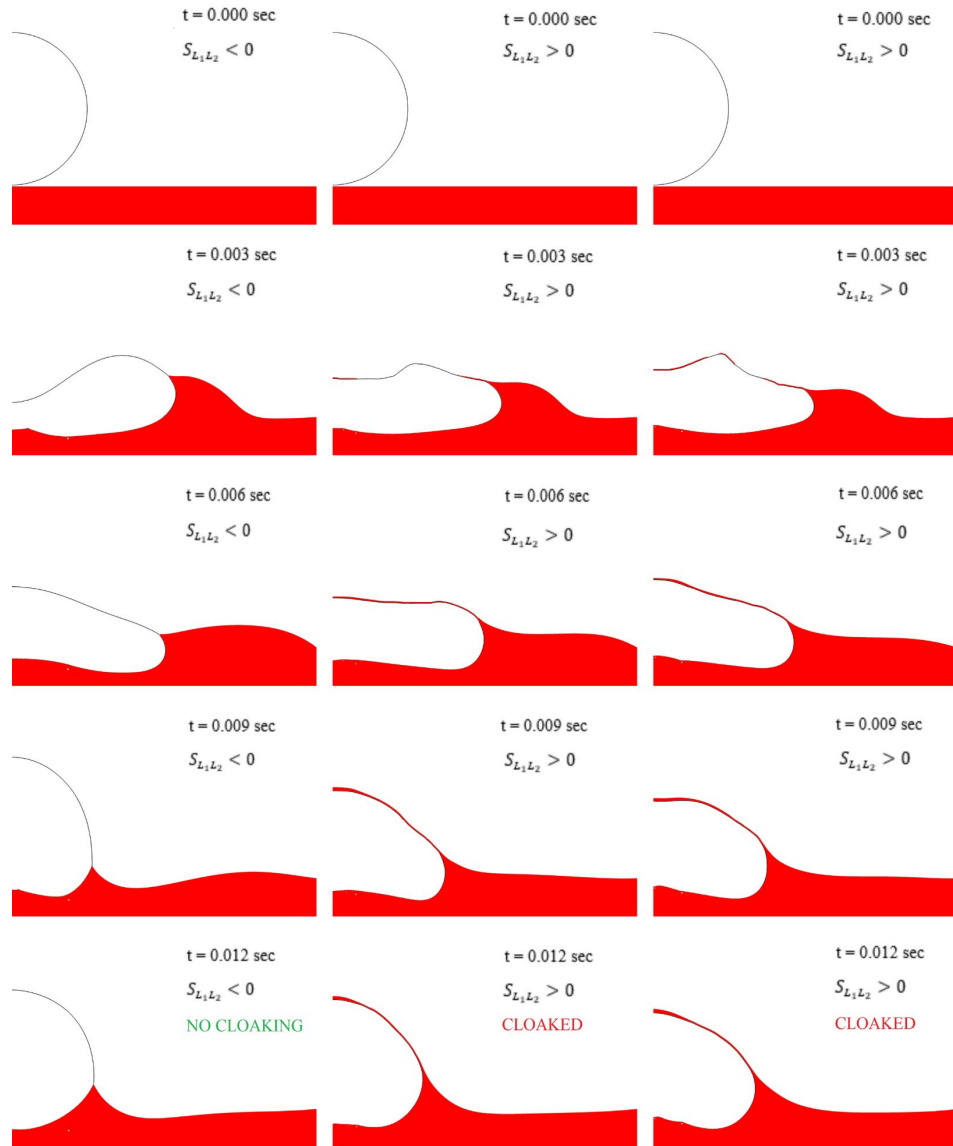
Figure 45: Drop impact speed of v = 0.5m/s on varying interfacial tensions and cloaking phenomena: from left to right: a) Case 1 - $\gamma_{L_1L_2} = 51.32\ mN/m$; b) Case 2 - $\gamma_{L_1L_2} = 31.79\ mN/m$; c) Case 3 - $\gamma_{L_1L_2} = 21.73\ mN/m$;

For instance, the Case 1 with negative spreading coefficient of $S_{L_1L_2} = $ -6.6, the maximum spreading width of the drop for impact speed of v = 0.25m/s and v = 0.5m/s is 0.3536cm and 0.4574cm, respectively. For Case 2 with positive spreading coefficient of $S_{L_1L_2} = $ 17.97mN/m, the maximum spreading width of the drop is 0.3174cm and 0.4522cm for v = 0.25m/s and v = 0.5m/s, respectively. For Case 3, with positive spreading coefficient of $S_{L_1L_2} = $ 32.97mN/m, the maximum spreading width for drop impacting at v = 0.25m/s is 0.28cm and for v = 0.5m/s is 0.4294cm.
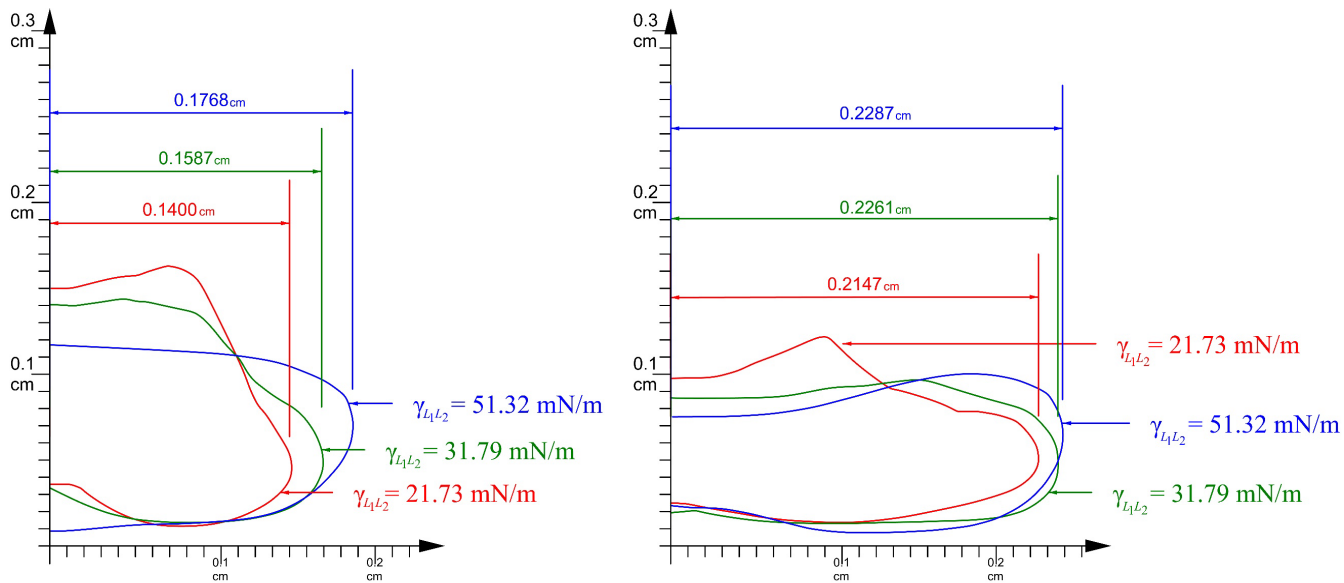
Figure 46: Maximum Spreading for drop impact cases for two different speeds, v = 0.25m/s (left) and v = 0.5 m/s (right) for different interfacial tensions

Thus, it can be deduced that with the increase in impact speed, the interfacial tension tends have less influence on the spreading behavior of the droplet, even though cloaking always occurs for the positive spreading coefficient cases.

Next, we present the impact cases of v = 5 m/s and v = 30 m/s to understand the interaction of the water drop with the underlying lubricant. The lubricant-water interfacial relationship is still held at $\gamma_{L_1 L_2} = 53$mN/m for both the impact cases. It is noticeable that at v = 5m/s, the lubricant spreads sidewise with smaller satellite drops fragmented and detached at the trail of the thick lamella jet. With the progression of time, the lubricant and the water drop travels together as the lamella starts to grow thicker and thicker. During the entire simulation time of more than t = 0.0008sec+, the droplet-lubricant jet travels sidewise and the width and the height of the lamella increases. Throughout this simulation, the lubricant acts as a protective film and the water phase never touches the bottom surface.
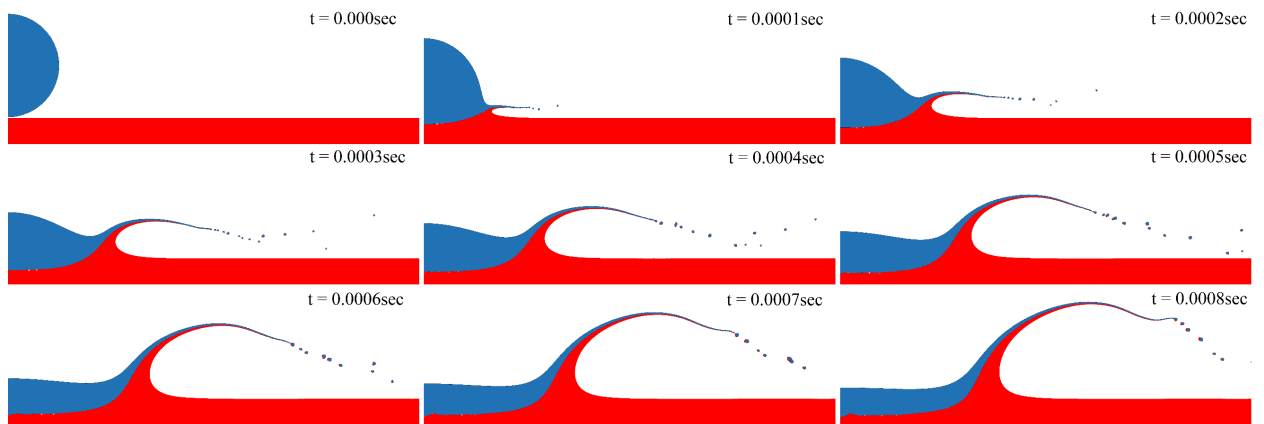
Figure 47: Drop Impact on Lubricant at v = 5 m/s

In contrast, for the case of impact speed at v = 30m/s, the drop impact and jetting is much different than that of at v = 5m/s. At time t = 0.00004sec, a secondary impingement can be observed, with the water-lubricant lamella starting to displace the far-right volume of the lubricant while the droplet submerges into the lubricant near the impact region. The secondary lamella impingement starts to form a very large circulation region and starts to

displace the lubricant film while exposing the bottom surface. After t = 0.00008sec, a large displacement can already be observed, and the mixture of water phase and the lubricant phase clearly touches the beneath surface. At t = 0.00012sec, two distinct recirculating disturbances can be observed within the lubricant film, and much of the lubricant is displaced while a large underneath surface remains exposed. The recirculation causes significant amount of lubricant displacement, allowing water phase to reach the surface beneath the lubricant and while cloaking occurs at low impacting speed water drops, secondary impingement at relatively high impact speed cases is therefore a primary concern of such drainage.
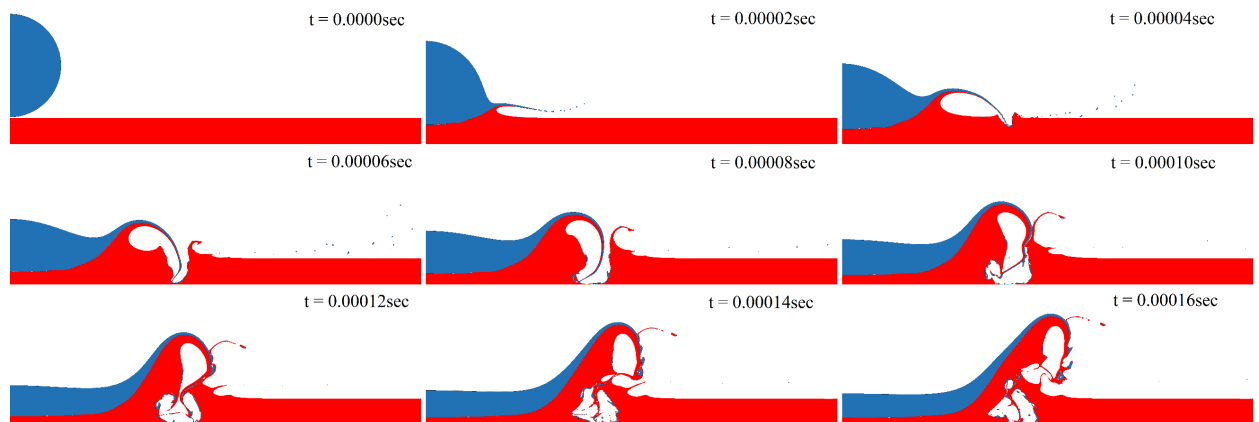
Figure 48: Drop Impact on Lubricant at v = 30 m/s, showing secondary impingement from t = 0.00004sec and onwards.

Array Spacing

We present our study of the concept of micro-well structure to hold lubricant while a drop impacts at varying speeds. The micro-well could be deemed to be especially useful and highly advantageous for cases with droplets impacting at a very high speed. As shown in Figure *49*, the micro-wells could potentially be used to hold lubricants in place and small

injecting nozzles could be used to inject/push the lubricant from an underneath source/reservoir at even at high pressure/altitude situations such like aircraft wings.
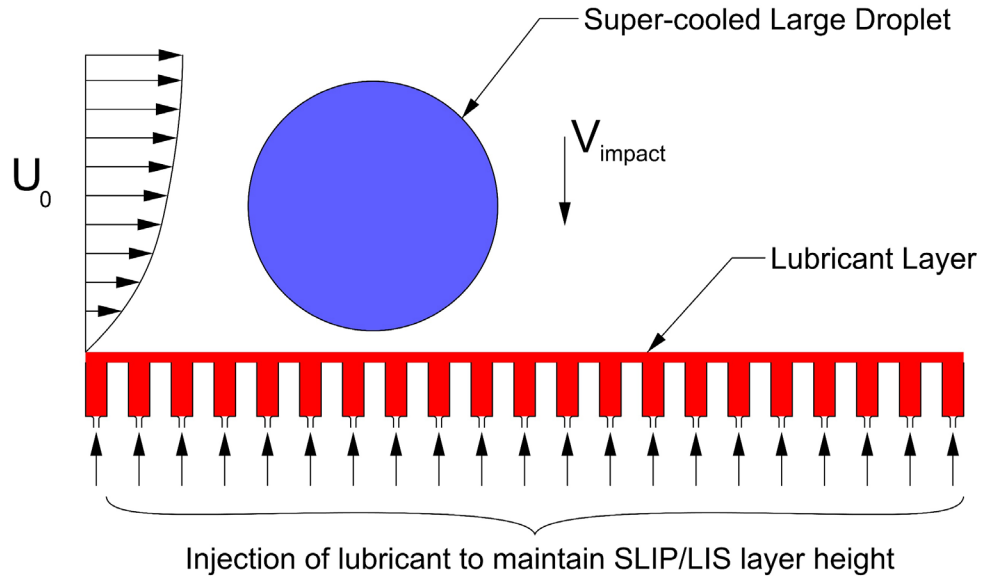
Figure 49: Schematic of Micro-well that could be used to inject and hold lubricant.

For the slow speed cases, two different micro-well array spacing arrangement of pitch distance = 0.033cm and 0.068cm, are compared with the no-array arrangement. The no-array arrangement has no micro-wells, and the lubricant sits on top of the solid substrate at a resting position. The impact speeds for these cases are set to 0.5m/s. The diameter of the drop is 2mm, and the lubricant is Krytox GPL 101 having an $\sigma_{L_2V} = 17.1 \, mN/m$ and $\sigma_{L_1L_2} = 53 \, mN/m$. The drop on the lubricant pool (without any micro-well array) completely submerges the drop with thick layer of cloaking being observed. On the other hand, the array arrangement shows very small amount of partial cloaking appearing on the

surface of the liquid droplet from t=10ms and onward. The drop-lubricant also forms a wetting ridge for the cases on the micro-wells and grows bigger over time.
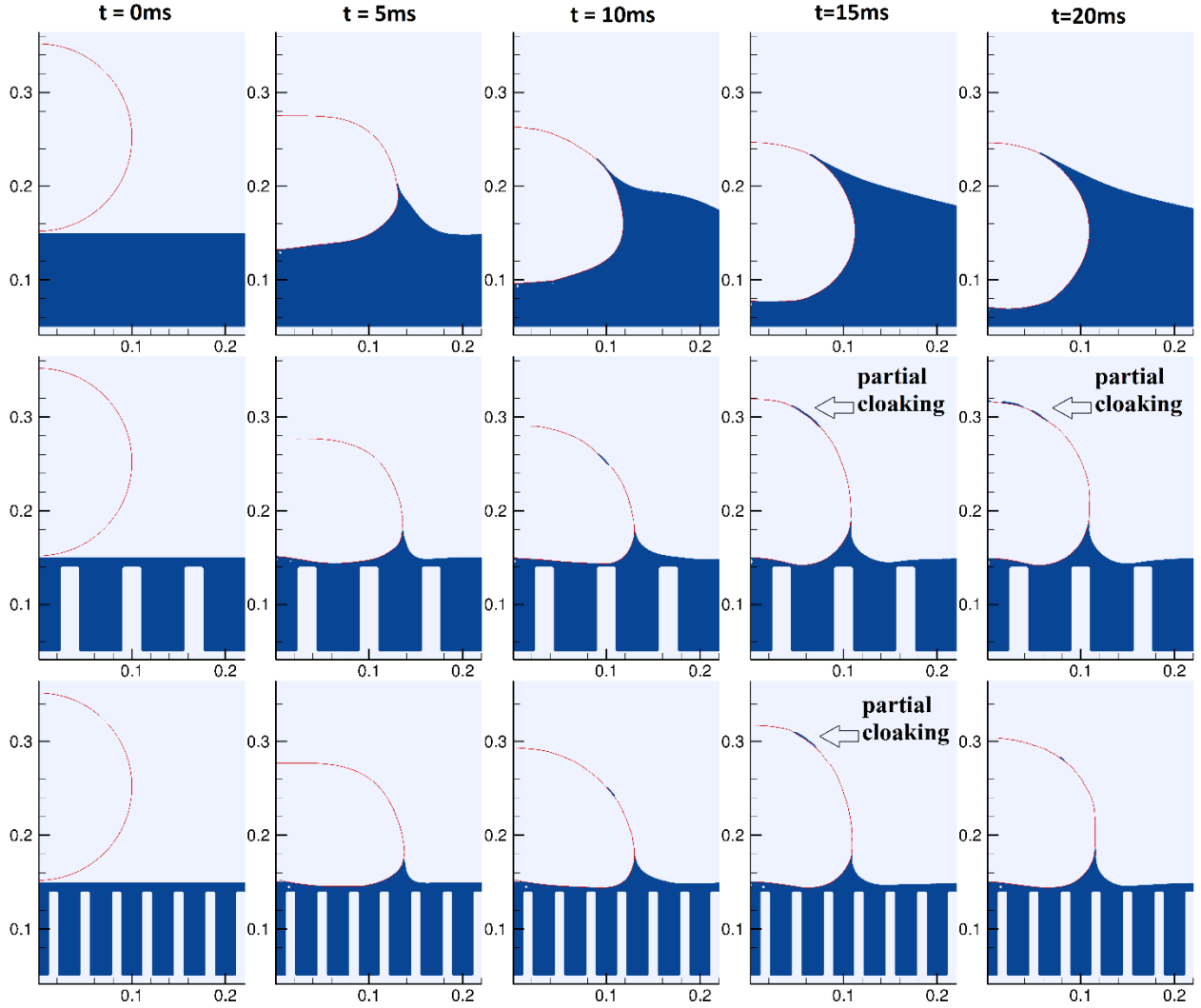
Figure 50: Drop impact timestamp on the Liquid Pool of Lubricant (top), on a micro-well with array spacing of 0.068cm (middle) and micro-well with array spacing of 0.033cm.

The drop on the lubricant pool has high impact induced kinetic energy, as shown in the Figure 51. The drops on the micro-well arrangement oscillates and therefore several crests and troughs are observed. The closes pitch distance (0.033cm) is highly absorbent of

kinetic energy, whereas the fluctuations in the case of array spacing of 0.068cm is considerably higher than 0.033cm.
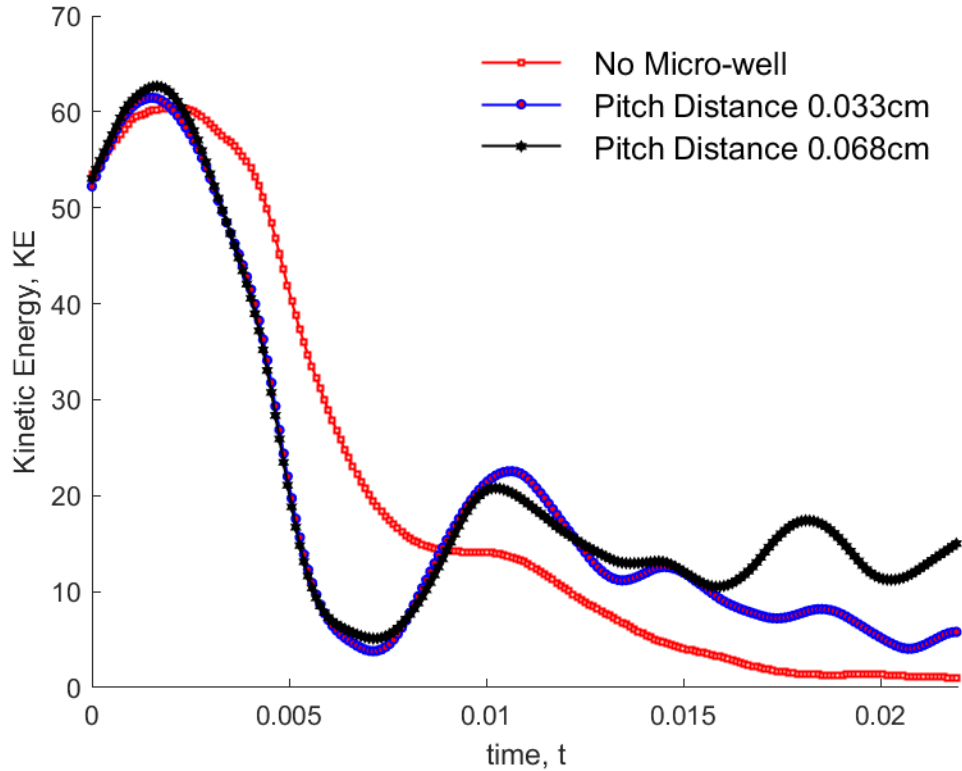
Figure 51: Kinetic Energy of Drops on Lubricant Pool, Micro-well with two different pitch distance(array spacing) =0.033cm and 0.068cm

Next, we present the high-speed case to correlate the impact speed of SLDs, which typically impacts at a range of 30m/s to 100m/s. The micro-well structures with different array distances can be examined from the Figure *52* and therefore can be compared with the flat surface. The flat surface has lubricant with a uniform depth of $100\mu m$ and is at rest prior to the impact. For the micro-well cases, the free-surface of the lubricant to the top of the micro-well pillar is also set to $100\mu m$. The three micro-well cases at high speed case requires a very finer array spacing and therefore, we have different pitch distances, namely

Case 1 = $660\mu m$, Case 2 = $330\mu m$ and Case 3 = $160\mu m$. The droplet impact speed is v = 30m/s and the drop diameter is still held at 2mm.
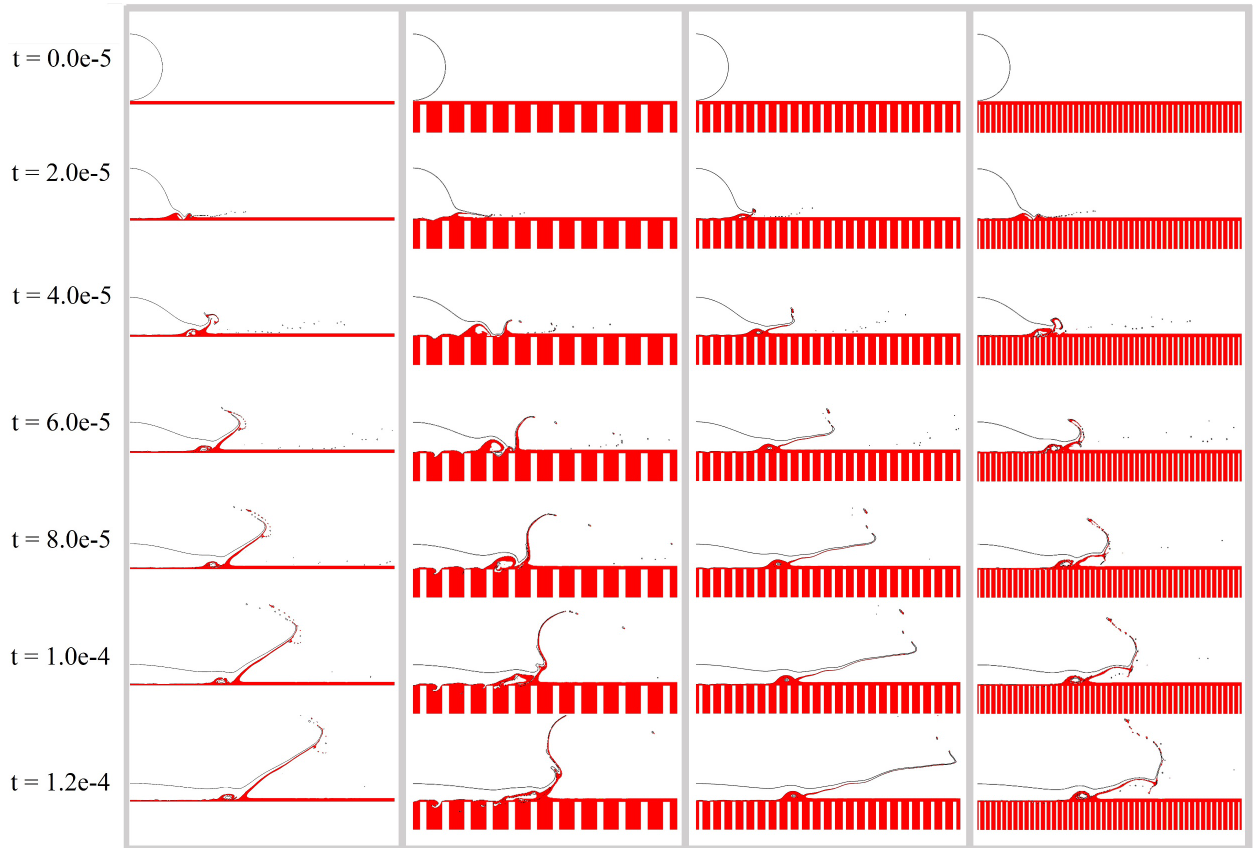
Figure 52: High Speed Impact at v = 30 m/s, from left to right: a) Flat Substrate; vs Micro-well w/ Pitch Distance b) pitch = $660\mu m$ c) pitch = $330\mu m$ and c) $160\mu m$

For the impact of the droplet on plane surface without a micro-well, the Kelvin-Helmholtz instability starts to generate after t = 4.0e-5sec. The Kelvin-Helmholtz instability arises due to the perturbation resulted from the velocity difference between the spreading water droplet and the initially stable lubricant. The instability causes recirculation regions within the lubricant and thus the lubricant-water mixture potentially would reach either the flat bottom of the non-micro-well case or near the vicinity of the micro-well surface. The

recirculation therefore poses the risk of ice accretion due to the exposure of nucleation site when drops at high-speed impact displaces significant amount of lubricant through means of such perturbation. We therefore estimated the length and height for recirculatory region for the time instance of t = 8.0e-5sec.
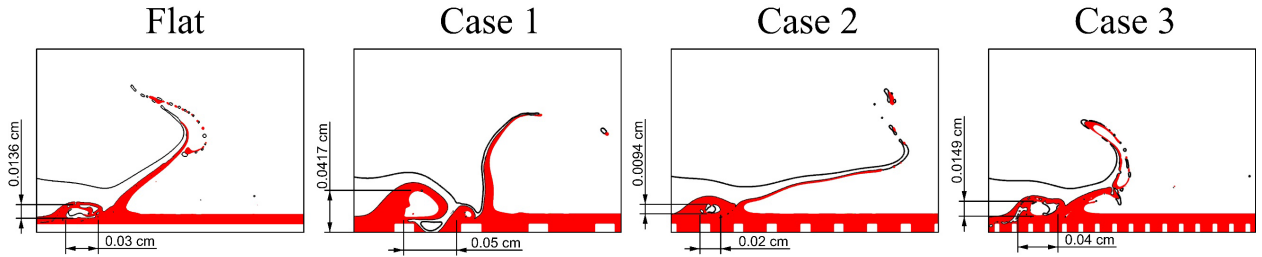
Figure 53: Recirculation due to Kelvin-Helmholtz Instability and the differences in height and width due to underneath substrate types: from left to right: a) Flat Substrate; vs Micro-well w/ Pitch Distance b) pitch = $660\mu m$ c) pitch = $330\mu m$ and c) $160\mu m$

For the flat case and the consequent Cases 1-3, it shows that the height for the recirculatory region follows:

$$h_{Case1} = 0.0417cm > h_{Case3} = 0.0149cm > h_{Case-Flat} = 0.0136cm > h_{Case2}$$
$$= 0.0094cm$$

In case of the width of the recirculatory region, the width is measured to be the following:

$$w_{Case1} = 0.05cm > w_{Case3} = 0.04cm > w_{Case-Flat} = 0.03cm > w_{Case2} = 0.02cm$$

Another finding is the occurrence of the secondary impingement for the Case 1, similar to secondary impingement that was observed for the deep lubricant case presented in Figure *52*. It can be seen from the figure in Case 1 that the secondary impingement causes much larger displacement of lubricant and the droplet scoops inside the micro-well cavity, which is otherwise very much absent for the other cases with shorter pitch distance. We therefore

measure the displaced lubricant using image tracing analysis from our post-processed data and present the area of total lubricant displaced at time t = 1.2e-4 in Figure *54*. The tracked areas are computed based on any red pigment (representing the lubricant) up to certain tolerance and accuracy and small micro and splitted daughter droplets are ignored. A reference line is used above the calm lubricant level and anything above it is traced to represent as the displaced volume and are presented as follows:

Case Flat = 0.001817 sq.cm   Case 1 = 0.003294 sq.cm   Case 2 = 0.001545 sq.cm   Case 3 = 0.002133 sq.cm
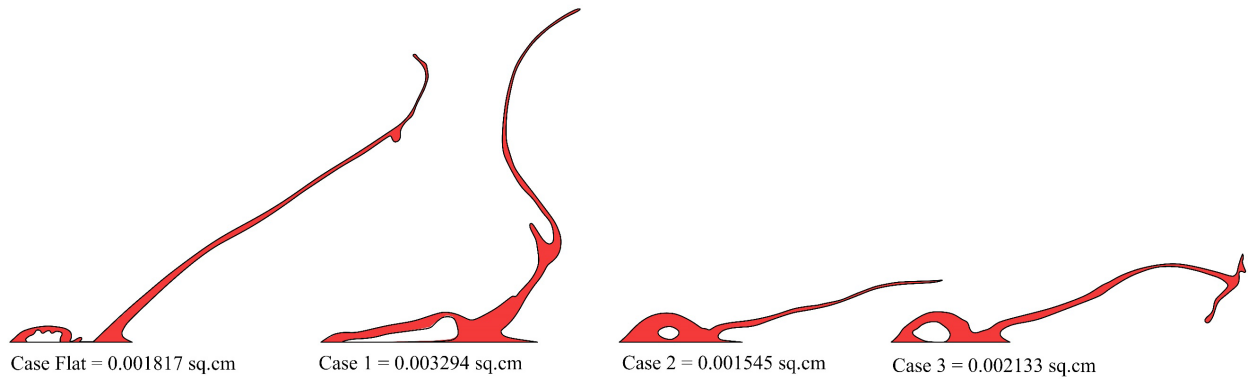
Figure 54: Displaced lubricant at time t = 1.2e-4, from left to right: a) Flat Substrate; vs Micro-well w/ Pitch Distance b) pitch = $660\mu m$ c) pitch = $330\mu m$ and c) $160\mu m$

Thus, the area for displaced lubricant from maximum to minimum shows the following relation:

$$Lubricant_{Case1} = 0.00329346498 \text{ cm}^2 > Lubricant_{Case3} = 0.0021327495 \text{ cm}^2$$

$$> Lubricant_{CaseFlat} = 0.00181623967 \text{ cm}^2 > Lubricant_{Case2}$$

$$= 0.00154514249 \text{ cm}^2$$

It can also be observed that the stem height of the lubricant of flat case and the Case 1 is the highest, and the Case 2 exhibits the least amount. Case 3, which has the closest pitch distance, has the widest spread of the lubricant and the calculated displaced area is very

close to the flat case, indicating that very close pitch distanced micro-well acts as a flat surface in essence.

Therefore, considering the height and width of the recirculatory Kelvin-Helmholtz disturbance, and the area of the displaced lubricant, for high impact speeds of v =30m/s, the best performing micro-well should ideally have a pitch distance of approximately $330\mu m$. While flat substrate has high probability of drainage due to shear flow and thick jetting, larger pitch distance has droplet scooping inside the cavity and also thicker jetting and very close pitch distance essentially behaves like a flat substrate.

Further Varying Surface Tensions and Forming Wetting Ridge

To capture the wetting ridge dependency on the interfacial tensions, we systematically vary the interfacial tension between the lubricant and the water drop, $\sigma_{L_1L_2}$, while holding the surface tension between the lubricant-vapor σ_{L_1V} and lubricant-vapor σ_{L_2V} constant. To minimize the interference of the varying micro-well spacing, for this part of the study we fixed the pitch distance to 0.033cm. The following interfacial tensions between the lubricant and water are simulated in our study:

Case no.	$\sigma_{L_1L_2}$ (mN/m)	σ_{L_2V}m (mN/m)	σ_{L_1V}m (mN/m)
Case 1	23	17.1	72.7
Case 2	33	17.1	72.7
Case 3	43	17.1	72.7
Case 4	63	17.1	72.7
Case 5	73	17.1	72.7

Figure *55* represents the attachment of the lubricant to the impact liquid drop at instance of t= 5ms for the five different cases of lubricants. Figure *56* represents for a later time at t =10ms. For the both the time instances, it is seen that the lower the interfacial tension, the more it attaches and adheres to the drop as it spreads and retracts. Also noticeable is that the drop which is under motion of spreading and retracting, does not necessarily form a fully triangulated ridge (also known as lubricant skirt), as proposed by many other literatures, but rather a continually evolving thin film that is an offset from the drop surface.
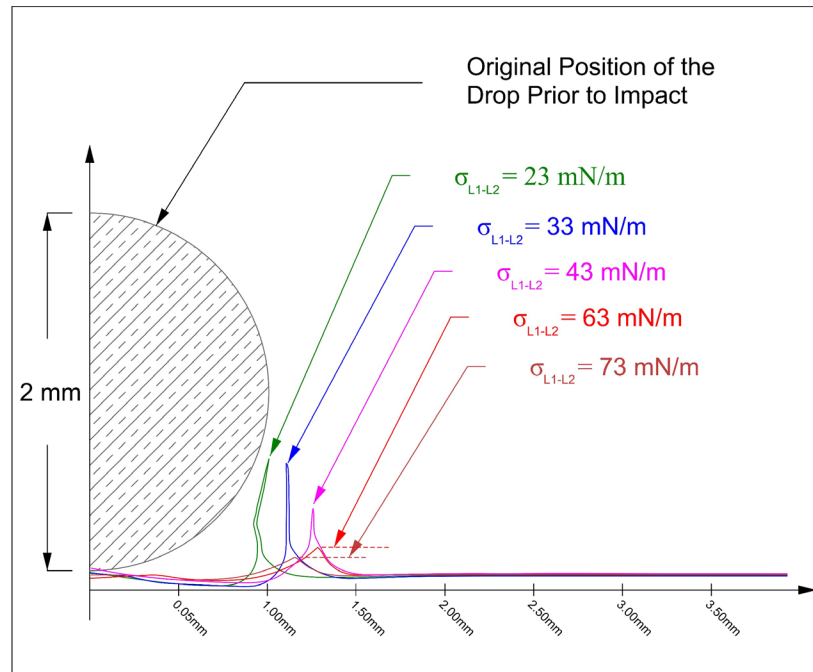
Figure 55: Thin layer of lubricant forming wetting ridge at the bottom vicinity of the drop, shown at t=5ms.
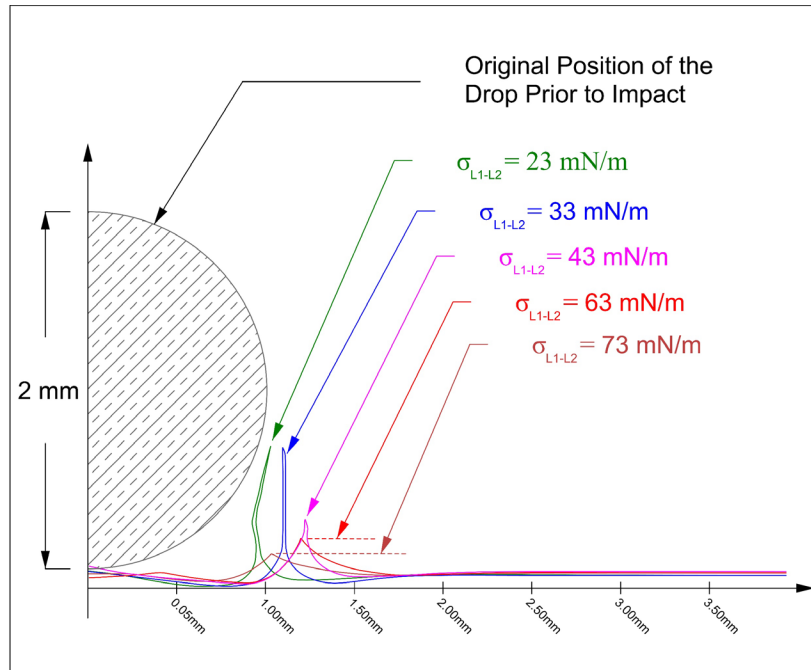
Figure 56: Thin layer of lubricant forming wetting ridge at the bottom vicinity of the drop, shown at t=10ms.
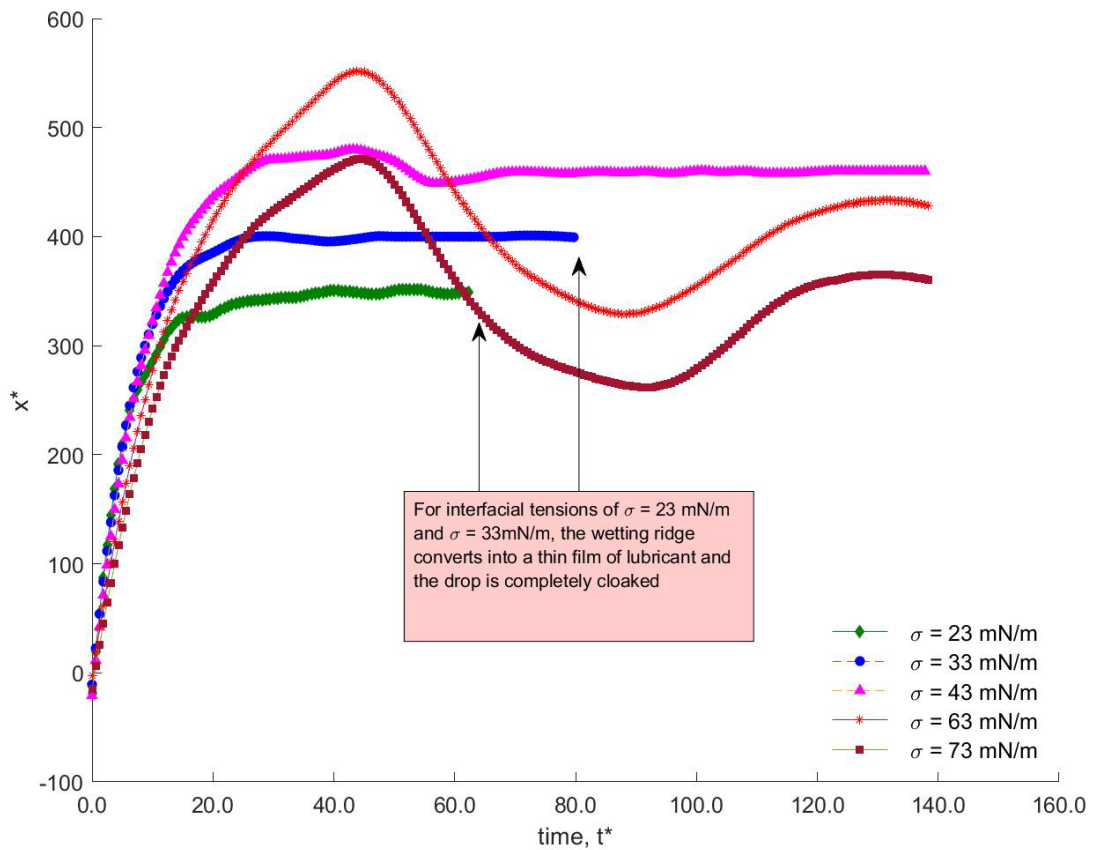
Figure 57: Horizontal Shift of the wetting ridge peak (triple point) over time for five different cases

The horizontal shift of the triple point (the wetting ridge peak) is shown in Figure *57*. It is important to note that at higher interfacial tensions, namely $\sigma_{L_1 L_2} = 63\ mN/m$ and $\sigma_{L_1 L_2} = 73\ mN/m$, the drop dynamics resembles the behavior of a drop spreading and retracting on a semi-solid surface. Considering the total simulation period of $t = 2ms$, the lower interfacial cases of $\sigma_{L_1 L_2} = 23\ mN/m$ and $\sigma_{L_1 L_2} = 33\ mN/m$ has much less horizontal spreading than in the case of higher interfacial cases and therefore the cloaking event takes place much earlier than in the case of higher interfacial cases.
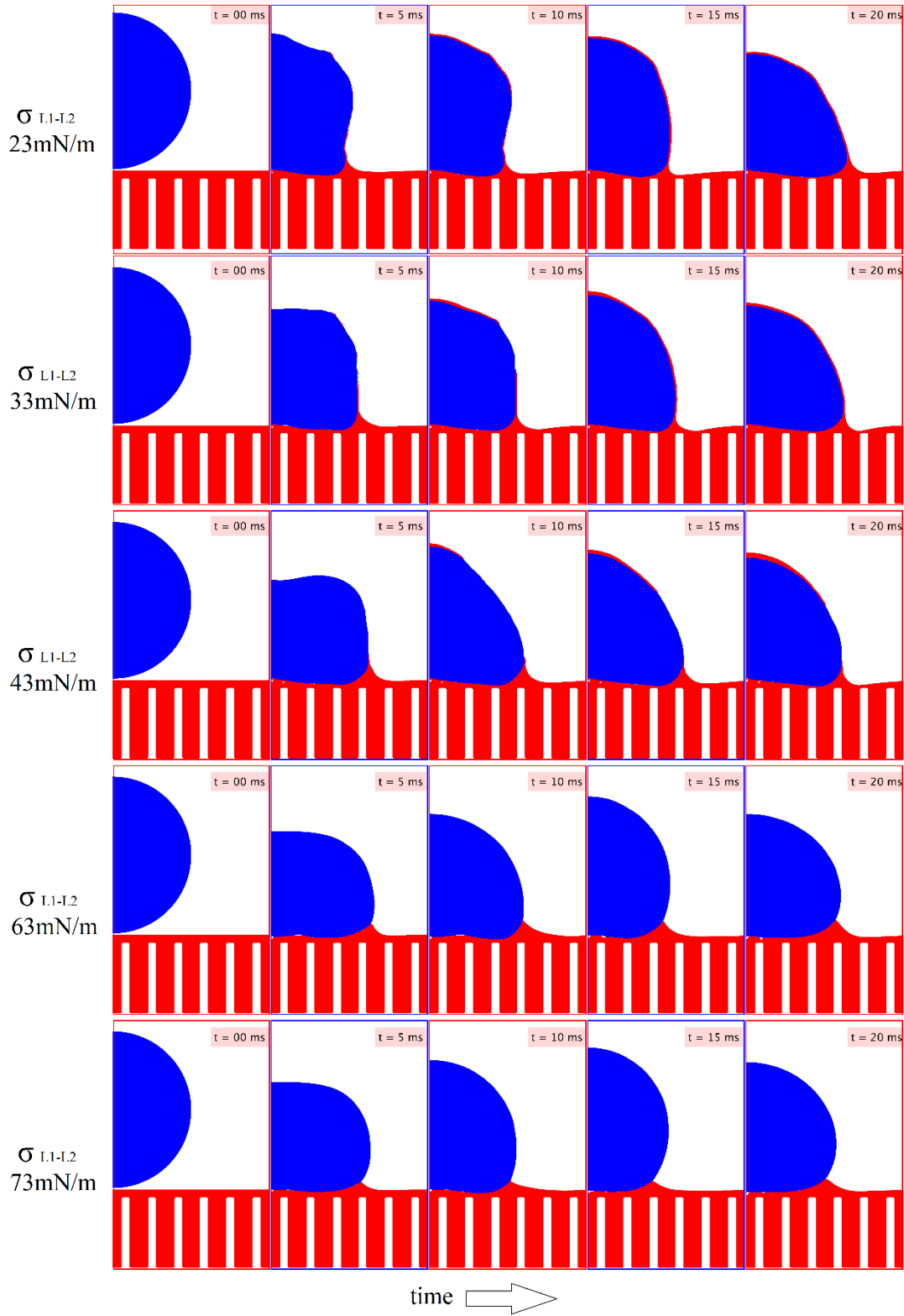
Figure 58: Increasing Interfacial Tension between the water drop and the lubricant reduces cloaking: From top to bottom: a) 23 mN/m b) 33 mN/m c) 43 mN/m d) 63 mN/m e) 73 mN/m .
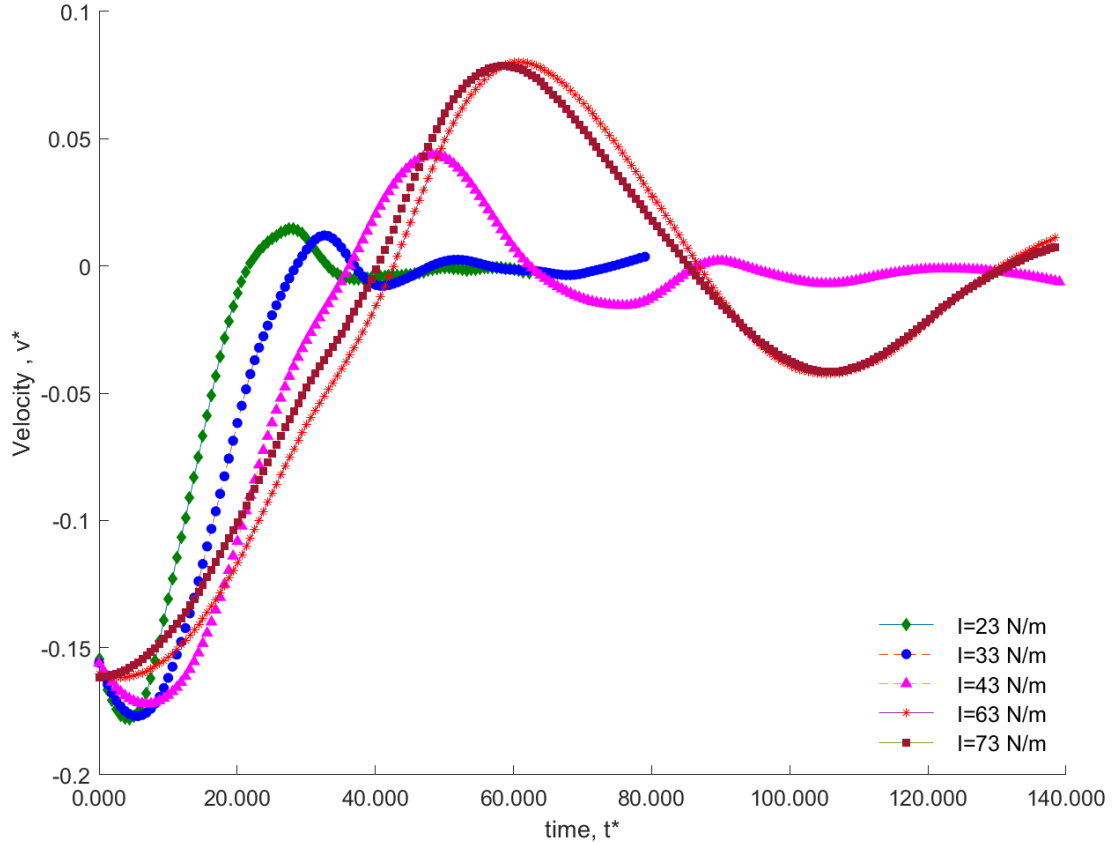
Figure 59: Fluctuation of the vertical velocity of the drop impacting on different lubricant-water interfacial tensions.

The vertical velocity of the drops impacting on different lubricant-water interfacial combinations are tracked and presented in the Figure *59*. Similar to a flat solid substrate, there is a lot of fluctuations in the vertical velocity as the drop spreads and retracts, but with lower interfacial tensions, the drop is absorbed and comes to static velocity quickly (plateauing close to the zero-eth line). This inherently stops the drop motion by restricting the movement, and therefore results in a complete and accelerated cloaking behavior.

CHAPTER VI
CONCLUSION

In this study we investigated the impact of water drops on dry and slippery lubricant and a lubricant-infused substrate at varying speeds and varying contact angles. A highly intiricate and accurate interface reconstruction method, known as the Moment-of-Fluid (MOF) has been employed to solve the numerical study involving multiphases/multimaterials. Several degrees of refinement, using Adaptive Mesh Refinement(AMR) were used at the interfaces of different phases/materials to accurately capture the movement and the dynamics of the water droplets that impacted the solid and the lubricant infused surfaces. It was found that drops on the dry micro-well had a smaller wetting area and spreading ratio than those on the flat surface. Furthermore, drops were observed to jump off the micro-well substrate for a range of impact velocities, unlike on the flat surface. Our analysis of the wetted area ratio revealed that the micro-well substrate had less solid-liquid adhesion, leading to more water-repelling behavior than the flat substrate. Additionally, we developed a regime map to investigate drop impact behavior for different velocities and contact angles. Finally, we compared the micro-well and micro-pillar substrates and observed that the micro-well remained unwetted over a wider area. For the droplet impact study on the lubricant layer, cloaking phenomenon was seen, where the lubricant encapsulates slow-moving drops on the slippery lubricant layer. A measurement for the thickness of the lubricant layer has been found to be changing dynamically as the water droplet undergoes spreading and receding motion over time. When the speed of impact is increased, the cloaking effect disappears,

and a water-lubricant mixture of lamella-jetting/ejection is produced. At even higher impact speeds, a secondary impingement occurs, which causes the exposed surface to come in contact with water due to excessive lubricant drainage. To address this issue, micro-well structures with varying pitch distances were introduced and imaging technique is used to compare the performance of the plane surface without micro-wells. This study confirms that certain spacing between micro-well structures is more effective in limiting lubricant drainage and splashing. Furthermore, the potential for enhancing preservation and refilling of lubricant using micro-wells has been demonstrated and such structures in aircraft bodies instead of plain surfaces were found to be highly advantageous.

REFERENCES

1. Bernardin, J.D., C.J. Stebbins, and I. Mudawar, *Effects of surface roughness on water droplet impact history and heat transfer regimes.* International Journal of Heat and Mass Transfer, 1996. **40**(1): p. 73-88.
2. Dietz, C., et al., *Visualization of droplet departure on a superhydrophobic surface and implications to heat transfer enhancement during dropwise condensation.* Applied physics letters, 2010. **97**(3): p. 033104.
3. Liu, Y., et al., *Anti-icing property of bio-inspired micro-structure superhydrophobic surfaces and heat transfer model.* Applied Surface Science, 2017. **400**: p. 498-505.
4. Li, H. and S. Yu, *A robust superhydrophobic surface and origins of its self-cleaning properties.* Applied Surface Science, 2017. **420**: p. 336-345.
5. Li, H., et al., *Modifier-free fabrication of durable superhydrophobic electrodeposited Cu-Zn coating on steel substrate with self-cleaning, anti-corrosion and anti-scaling properties.* Applied Surface Science, 2019. **481**: p. 872-882.
6. Zheng, S., et al., *Fabrication of self-cleaning superhydrophobic surface on aluminum alloys with excellent corrosion resistance.* Surface and Coatings Technology, 2015. **276**: p. 341-348.
7. He, B., et al., *The roles of wettability and surface tension in droplet formation during inkjet printing.* Scientific Reports, 2017. **7**(1): p. 11841.
8. Modak, C.D., et al., *Drop impact printing.* Nature Communications, 2020. **11**(1): p. 4327.
9. Broeren, A., et al. *Characteristics of SLD ice accretions on airfoils and their aerodynamic effects*. in *43rd AIAA aerospace sciences meeting and exhibit*. 2005.
10. Anderson, D. and J.-C. Tsao. *Additional results of ice-accretion scaling at SLD conditions*. in *41st Aerospace Sciences Meeting and Exhibit*. 2003.
11. Papadakis, M., et al. *Water impingement experiments on a NACA 23012 airfoil with simulated glaze ice shapes*. in *42nd AIAA aerospace sciences meeting and exhibit*. 2004.
12. Ashenden, R., W. Lindberg, and J. Marwitz. *Two-dimensional NACA 23012 airfoil performance degradation by super cooled cloud, drizzle, and rain drop icing*. in *34th Aerospace Sciences Meeting and Exhibit*. 1996.
13. Trunov, O. and M. Ingelman-Sundberg, *On the Problem of Horizontal Tail Stall Due to Ice.* Report JR-3, The Swedish Soviet Working Group on Scientific-Technical Cooperation in the Field of Flight Safety, 1985. **1**: p. 15-18.
14. Bragg, M. *Aerodynamics of supercooled-large-droplet ice accretions and the effect on aircraft control*. in *Proceedings of the FAA International Conference on Aircraft Inflight Icing*. 1996.
15. Lynch, F.T. and A. Khodadoust, *Effects of ice accretions on aircraft aerodynamics.* Progress in Aerospace Sciences, 2001. **37**(8): p. 669-767.
16. Whalen, E., et al. *Characteristics of runback ice accretions on airfoils and their aerodynamics effects*. in *43rd AIAA Aerospace Sciences Meeting and Exhibit*. 2005.
17. Cao, Y., G. Zhong, and C. Ma, *Numerical simulation of ice accretion prediction on multiple element airfoil.* Science China Technological Sciences, 2011. **54**(9): p. 2296-2304.

18.   Bragg, M. *Aircraft aerodynamic effects due to large droplet ice accretions*. in *34th Aerospace Sciences Meeting and Exhibit*. 1996.

19.   Cao, Y., W. Tan, and Z. Wu, *Aircraft icing: An ongoing threat to aviation safety.* Aerospace Science and Technology, 2018. **75**: p. 353-385.

20.   Cao, Y., et al., *Aircraft flight characteristics in icing conditions.* Progress in Aerospace Sciences, 2015. **74**: p. 62-80.

21.   Kind, R., et al., *Experimental and computational simulation of in-flight icing phenomena.* Progress in Aerospace Sciences, 1998. **34**(5-6): p. 257-345.

22.   Nascimento, R.M.d., et al., *Water Drop Evaporation on Mushroom-like Superhydrophobic Surfaces: Temperature Effects.* Langmuir, 2016. **32**(8): p. 2005-2009.

23.   Wang, L., et al., *Manufacturing of mushroom-shaped structures and its hydrophobic robustness analysis based on energy minimization approach.* AIP Advances, 2017. **7**(7): p. 075110.

24.   Hu, Z., et al., *Off-centered droplet impact on single-ridge superhydrophobic surfaces.* Experimental Thermal and Fluid Science, 2021. **120**: p. 110245.

25.   Patankar, N.A., *Mimicking the lotus effect: influence of double roughness structures and slender pillars.* Langmuir, 2004. **20**(19): p. 8209-8213.

26.   Graeber, G., et al., *3D-printed surface architecture enhancing superhydrophobicity and viscous droplet repellency.* ACS applied materials & interfaces, 2018. **10**(49): p. 43275-43281.

27.   Song, J., et al., *Large-area fabrication of droplet pancake bouncing surface and control of bouncing state.* ACS nano, 2017. **11**(9): p. 9259-9267.

28.   Song, J., et al., *Robust Superhydrophobic Conical Pillars from Syringe Needle Shape to Straight Conical Pillar Shape for Droplet Pancake Bouncing.* ACS Applied Materials & Interfaces, 2019. **11**(48): p. 45345-45353.

29.   Guo, C., et al., *Droplet impact on anisotropic superhydrophobic surfaces.* Langmuir, 2018. **34**(11): p. 3533-3540.

30.   Varanasi, K.K., et al., *Frost formation and ice adhesion on superhydrophobic surfaces.* Applied Physics Letters, 2010. **97**(23): p. 234102.

31.   Chen, J., et al., *Superhydrophobic surfaces cannot reduce ice adhesion.* Applied Physics Letters, 2012. **101**(11): p. 111603.

32.   Saito, H., K. Takai, and G. Yamauchi, *Water-and ice-repellent coatings.* Surface Coatings International, 1997. **80**(4): p. 168-171.

33.   Kulinich, S. and M. Farzaneh, *How wetting hysteresis influences ice adhesion strength on superhydrophobic surfaces.* Langmuir, 2009. **25**(16): p. 8854-8856.

34.   Sarkar, D.K. and M. Farzaneh, *Superhydrophobic coatings with reduced ice adhesion.* Journal of Adhesion Science and Technology, 2009. **23**(9): p. 1215-1237.

35.   Farhadi, S., M. Farzaneh, and S.A. Kulinich, *Anti-icing performance of superhydrophobic surfaces.* Applied Surface Science, 2011. **257**(14): p. 6264-6269.

36.   Zou, M., et al., *Effects of surface roughness and energy on ice adhesion strength.* Applied Surface Science, 2011. **257**(8): p. 3786-3792.

37.   Hassan, M., H. Lee, and S. Lim, *The variation of ice adhesion strength with substrate surface roughness.* Measurement Science and Technology, 2010. **21**(7): p. 075701.

38.   Weisensee, P.B., et al., *Condensate droplet size distribution on lubricant-infused surfaces.* International Journal of Heat and Mass Transfer, 2017. **109**: p. 187-199.

39.   Sett, S., et al., *Lubricant-Infused Surfaces for Low-Surface-Tension Fluids: Promise versus Reality.* ACS Applied Materials & Interfaces, 2017. **9**(41): p. 36400-36408.

40.   Agarwal, H., et al., *Slippery nanoemulsion-infused porous surfaces (SNIPS): anti-fouling coatings that can host and sustain the release of water-soluble agents.* Chemical Communications, 2021. **57**(94): p. 12691-12694.

41.   Cao, Y., et al., *Antiwetting and Antifouling Performances of Different Lubricant-Infused Slippery Surfaces.* Langmuir, 2020. **36**(45): p. 13396-13407.

42.   Li, Q. and Z. Guo, *Lubricant-infused slippery surfaces: Facile fabrication, unique liquid repellence and antireflective properties.* Journal of Colloid and Interface Science, 2019. **536**: p. 507-515.

43.   Lu, Y., et al., *Robust self-cleaning surfaces that function when exposed to either air or oil.* Science, 2015. **347**(6226): p. 1132-1135.

44.   Lou, X., et al., *External Stimuli Responsive Liquid-Infused Surfaces Switching between Slippery and Nonslippery States: Fabrications and Applications.* Advanced Functional Materials, 2020. **30**(10): p. 1901130.

45.   Meuler, A.J., G.H. McKinley, and R.E. Cohen, *Exploiting Topographical Texture To Impart Icephobicity.* ACS Nano, 2010. **4**(12): p. 7048-7052.

46.   Meuler, A.J., et al., *Relationships between water wettability and ice adhesion.* ACS applied materials & interfaces, 2010. **2**(11): p. 3100-3110.

47.   Van Oss, C., et al., *Surface tension parameters of ice obtained from contact angle data and from positive and negative particle adhesion to advancing freezing fronts.* Journal of adhesion science and technology, 1992. **6**(4): p. 503-516.

48.   Wang, B.L., L. Heng, and L. Jiang, *Temperature-responsive anisotropic slippery surface for smart control of the droplet motion.* ACS applied materials & interfaces, 2018. **10**(8): p. 7442-7450.

49.   Orme, B.V., et al., *Droplet Retention and Shedding on Slippery Substrates.* Langmuir, 2019. **35**(28): p. 9146-9151.

50.   Hospers, J. and H.W.M. Hoeijmakers. *Numerical simulation of SLD ice accretions*. in *SAE International Conference on Aircraft and Engine Icing and Ground Deicing, Chicago, Illinois, SAE2011-38-0071*. 2011.

51.   Bae, J. and K. Yee, *Numerical Investigation of Droplet Breakup Effects on Droplet–Wall Interactions Under SLD Conditions.* International Journal of Aeronautical and Space Sciences, 2021. **22**(5): p. 1005-1018.

52.   Sussman, M., et al., *An Adaptive Level Set Approach for Incompressible Two-Phase Flows.* Journal of Computational Physics, 1999. **148**(1): p. 81-124.

53.   Parker, B.J. and D.L. Youngs, *Two and three dimensional Eulerian simulation of fluid flow with material interfaces*. 1992, UK Atomic Weapons Establishment, Aldermaston, Berkshire.

54.   Yeah, G.H. and J. Tu, *Computational Techniques for Multiphase Flows*. 2010: Butterworth-Heinemann.

55.   Pilliod, J.E. and E.G. Puckett, *Second-order accurate volume-of-fluid algorithms for tracking material interfaces.* Journal of Computational Physics, 2004(199): p. 465-502.

56.   Dyadechko, V. and M. Shashkov, *Reconstruction of multi-material interfaces from moment data.* Journal of Computational Physics, 2008. **227**(11): p. 5361-5384.

57.   Jemison, M., M. Sussman, and M. Shashkov, *Filament capturing with the Multimaterial Moment-of-Fluid method.* Journal of Computational Physics, 2015. **285**: p. 149-172.

58.   Sussman, M. and M. Ohta, *High-order techniques for calculating surface tension forces*, in *Free Boundary Problems*. 2006, Springer. p. 425-434.

59.   Sussman, M. and M. Ohta, *Improvements for calculating two-phase bubble and drop motion using an adaptive sharp interface method.* Fluid Dyn. Mater. Process, 2007. **3**(1): p. 21-36.

60.   Sussman, M. and M. Ohta, *A stable and efficient method for treating surface tension in incompressible two-phase flow.* SIAM Journal on Scientific Computing, 2009. **31**(4): p. 2447-2471.

61.   Kim, H.Y. and J.H. Chun, *The recoiling of liquid droplets upon collision with solid surfaces.* Physics of Fluids, 2001. **13**(3): p. 643-659.

62.   Jiang, T.-S., O.H. Soo-Gun, and J.C. Slattery, *Correlation for dynamic contact angle.* Journal of Colloid and Interface Science, 1979. **69**(1): p. 74-77.

63.   Chen, X., J. Lu, and G. Tryggvason, *Numerical simulation of self-propelled non-equal sized droplets.* Physics of Fluids, 2019. **31**(5): p. 052107.

64.   YanChen, et al., *Numerical investigation of surface curvature effect on the self-propelled capability of coalesced drops.* 2020. **32**(12): p. 122117.

65.   Cheng, Y., J. Xu, and Y. Sui, *Numerical investigation of coalescence-induced droplet jumping on superhydrophobic surfaces for efficient dropwise condensation heat transfer.* International Journal of Heat and Mass Transfer, 2016. **95**: p. 506-516.

66.   Boreyko, J.B. and C.-H. Chen, *Self-propelled jumping drops on superhydrophobic surfaces.* Physics of Fluids, 2010. **22**(9): p. 091110.

67.   Boreyko, J.B. and C.-H. Chen, *Self-Propelled Dropwise Condensate on Superhydrophobic Surfaces.* Physical Review Letters, 2009. **103**(18): p. 184501.

68.   Zhang, Q., et al., *Anti-icing surfaces based on enhanced self-propelled jumping of condensed water microdroplets.* Chemical Communications, 2013. **49**(40): p. 4516-4518.

69.   Zhang, Q., et al., *Condensation mode determines the freezing of condensed water on solid surfaces.* Soft Matter, 2012. **8**(32): p. 8285-8288.

70.   Kim, H., et al., *Water harvesting from air with metal-organic frameworks powered by natural sunlight.* Science, 2017. **356**(6336): p. 430-434.

71.   Lee, A., et al., *Water harvest via dewing.* Langmuir, 2012. **28**(27): p. 10183-10191.

72.   Liu, F., et al., *Self-propelled jumping upon drop coalescence on Leidenfrost surfaces.* Journal of Fluid Mechanics, 2014. **752**: p. 22-38.

73.   Wang, F.-C., F. Yang, and Y.-P. Zhao, *Size effect on the coalescence-induced self-propelled droplet.* Applied Physics Letters, 2011. **98**(5): p. 053112.

74.   Liu, F., et al., *Numerical simulations of self-propelled jumping upon drop coalescence on non-wetting surfaces.* Journal of Fluid Mechanics, 2014. **752**: p. 39-65.

75.   Bhushan, B. and Y.C. Jung, *Natural and biomimetic artificial surfaces for superhydrophobicity, self-cleaning, low adhesion, and drag reduction.* Progress in Materials Science, 2011. **56**(1): p. 1-108.

76.   Burton, Z. and B. Bhushan, *Hydrophobicity, adhesion, and friction properties of nanopatterned polymers and scale dependence for micro-and nanoelectromechanical systems.* Nano letters, 2005. **5**(8): p. 1607-1613.

77.   Koch, K., et al., *Fabrication of artificial Lotus leaves and significance of hierarchical structure for superhydrophobicity and low adhesion.* Soft Matter, 2009. **5**(7): p. 1386-1393.

78.   Gao, L. and T.J. McCarthy, *The "lotus effect" explained: two reasons why two length scales of topography are important.* Langmuir, 2006. **22**(7): p. 2966-2967.

79.   Giacomello, A., et al., *Metastable wetting on superhydrophobic surfaces: continuum and atomistic views of the Cassie-Baxter–Wenzel transition.* Physical review letters, 2012. **109**(22): p. 226102.

80. Wu, D., et al., *Curvature-Driven Reversible In Situ Switching Between Pinned and Roll-Down Superhydrophobic States for Water Droplet Transportation.* Advanced Materials, 2011. **23**(4): p. 545-549.

81. Darmanin, T. and F. Guittard, *Superhydrophobic and superoleophobic properties in nature.* Materials Today, 2015. **18**(5): p. 273-285.

82. Liu, Y., et al., *Pancake bouncing on superhydrophobic surfaces.* Nature physics, 2014. **10**(7): p. 515.

83. Hao, C., et al., *Superhydrophobic-like tunable droplet bouncing on slippery liquid interfaces.* Nature communications, 2015. **6**.

84. Liu, Y., et al., *Symmetry breaking in drop bouncing on curved surfaces.* Nature communications, 2015. **6**.

85. De Ruiter, J., et al., *Wettability-independent bouncing on flat surfaces mediated by thin air films.* Nature physics, 2015. **11**(1): p. 48.

86. Kolinski, J.M., L. Mahadevan, and S. Rubinstein, *Drops can bounce from perfectly hydrophilic surfaces.* EPL (Europhysics Letters), 2014. **108**(2): p. 24001.

87. Richard, D., C. Clanet, and D. Quéré, *Surface phenomena: Contact time of a bouncing drop.* Nature, 2002. **417**(6891): p. 811-811.

88. Zhang, K., et al., *Self-propelled droplet removal from hydrophobic fiber-based coalescers.* Physical review letters, 2015. **115**(7): p. 074502.

89. Enright, R., et al., *Condensation on superhydrophobic copper oxide nanostructures.* Journal of Heat Transfer, 2013. **135**(9): p. 091304.

90. Nam, Y., H. Kim, and S. Shin, *Energy and hydrodynamic analyses of coalescence-induced jumping droplets.* Applied Physics Letters, 2013. **103**(16): p. 161601.

91. Enright, R., et al., *How coalescing droplets jump.* ACS nano, 2014. **8**(10): p. 10352-10362.

92. Peng, B., et al., *Analysis of condensation heat transfer enhancement with dropwise-filmwise hybrid surface: Droplet sizes effect.* International Journal of Heat and Mass Transfer, 2014. **77**: p. 785-794.

93. Young, T., *III. An essay on the cohesion of fluids.* Philosophical Transactions of the Royal Society of London, 1805. **95**: p. 65-87.

94. Orme, M., *Experiments on droplet collisions, bounce, coalescence and disruption.* Progress in Energy and Combustion Science, 1997. **23**(1): p. 65-79.

95. Qian, J. and C.K. Law, *Regimes of coalescence and separation in droplet collision.* Journal of Fluid Mechanics, 1997. **331**: p. 59-80.

96. Andrieu, C., et al., *Coalescence of sessile drops.* Journal of Fluid Mechanics, 2002. **453**: p. 427-438.

97. Ristenpart, W.D., et al., *Coalescence of Spreading Droplets on a Wettable Substrate.* Physical Review Letters, 2006. **97**(6): p. 064501.

98. Lee, M.W., et al., *Coalescence of Two Drops on Partially Wettable Substrates.* Langmuir, 2012. **28**(8): p. 3791-3798.

99. Kapur, N. and P.H. Gaskell, *Morphology and dynamics of droplet coalescence on a surface.* Physical Review E, 2007. **75**(5): p. 056315.

100. Bird, J.C., et al., *Reducing the contact time of a bouncing drop.* Nature, 2013. **503**(7476): p. 385-388.

101. Bartolo, D., C. Josserand, and D. Bonn, *Retraction dynamics of aqueous drops upon impact on non-wetting surfaces.* Journal of Fluid Mechanics, 2005. **545**: p. 329-338.

102. Clanet, C., et al., *Maximal deformation of an impacting drop.* Journal of Fluid Mechanics, 2004. **517**: p. 199-208.

103. Fukai, J., et al., *Modeling of the deformation of a liquid droplet impinging upon a flat surface.* Physics of Fluids A: Fluid Dynamics, 1993. **5**(11): p. 2588-2599.

104. Roisman, I.V., R. Rioboo, and C. Tropea, *Normal impact of a liquid drop on a dry surface: model for spreading and receding.* Proceedings of the Royal Society of London. Series A: Mathematical, Physical and Engineering Sciences, 2002. **458**(2022): p. 1411-1430.

105. Wang, F. and T. Fang, *Retraction dynamics of water droplets after impacting upon solid surfaces from hydrophilic to superhydrophobic.* Physical Review Fluids, 2020. **5**(3): p. 033604.

106. Damak, M., M.N. Hyder, and K.K. Varanasi, *Enhancing droplet deposition through in-situ precipitation.* Nature Communications, 2016. **7**(1): p. 12560.

107. Gaskin, R., K. Steele, and W.J.N.Z.P.P. Forster, *Characterising plant surfaces for spray adhesion and retention.* 2005. **58**: p. 179-183.

108. Dorr, G.J., et al., *Impaction of spray droplets on leaves: influence of formulation and leaf character on shatter, bounce and adhesion.* Experiments in Fluids, 2015. **56**(7): p. 143.

109. Feng, L., et al., *Copper-based superhydrophobic materials with long-term durability, stability, regenerability, and self-cleaning property.* Colloids and Surfaces A: Physicochemical and Engineering Aspects, 2016. **508**: p. 39-47.

110. Wang, N., et al., *Mechanically Robust Superhydrophobic Steel Surface with Anti-Icing, UV-Durability, and Corrosion Resistance Properties.* ACS Applied Materials & Interfaces, 2015. **7**(11): p. 6260-6272.

111. Hasan, F., et al., *Cavitation Induced Damage in Soft Biomaterials.* Multiscale Science and Engineering, 2021. **3**(1): p. 67-87.

112. Selvam, R.P., et al., *Direct simulation of spray cooling: effect of vapor bubble growth and liquid droplet impact on heat transfer.* 2006. **49**(23-24): p. 4265-4278.

113. D BERNARDIN, J., et al., *Effects of surface roughness on water droplet impact history and heat transfer regimes.* 1996. **40**(1): p. 73-88.

114. Healy, W.M., et al., *On the validity of the adiabatic spreading assumption in droplet impact cooling.* 2001. **44**(20): p. 3869-3881.

115. Shen, Y., et al., *Icephobic/anti-icing potential of superhydrophobic Ti6Al4V surfaces with hierarchical textures.* RSC Advances, 2015. **5**(3): p. 1666-1672.

116. Lai, Y., et al., *Multi-functional hybrid protonated titanate nanobelts with tunable wettability.* Soft Matter, 2011. **7**(13): p. 6313-6319.

117. Latthe, S., et al., *Recent developments in air-trapped superhydrophobic and liquid-infused slippery surfaces for anti-icing application.* Progress in Organic Coatings, 2019. **137**: p. 105373.

118. Neinhuis, C. and W.J.A.o.b. Barthlott, *Characterization and distribution of water-repellent, self-cleaning plant surfaces.* 1997. **79**(6): p. 667-677.

119. Barthlott, W. and C.J.P. Neinhuis, *Purity of the sacred lotus, or escape from contamination in biological surfaces.* 1997. **202**(1): p. 1-8.

120. Bernardino, N.R., V. Blickle, and S. Dietrich, *Wetting of surfaces covered by elastic hairs.* Langmuir, 2010. **26**(10): p. 7233-41.

121. Quéré, D., *Non-sticking drops.* Reports on Progress in Physics, 2005. **68**(11): p. 2495-2532.

122. Mazloomi Moqaddam, A., S.S. Chikatamarla, and I.V. Karlin, *Drops bouncing off macro-textured superhydrophobic surfaces.* Journal of Fluid Mechanics, 2017. **824**: p. 866-885.

123. Rykaczewski, K., et al., *Direct Imaging of Complex Nano- to Microscale Interfaces Involving Solid, Liquid, and Gas Phases.* ACS Nano, 2012. **6**(10): p. 9326-9334.

124. Josserand, C. and S.T. Thoroddsen, *Drop Impact on a Solid Surface.* Annual Review of Fluid Mechanics, 2016. **48**(1): p. 365-391.

125. Manoharan, K. and S.J.J.o.M. Bhattacharya, *Superhydrophobic surfaces review: Functional application, fabrication techniques and limitations.* 2019. **2**(1): p. 59-78.

126. Ma, M., R.M.J.C.o.i.c. Hill, and i. science, *Superhydrophobic surfaces.* 2006. **11**(4): p. 193-202.

127. Nilsson, M.A., R.J. Daniello, and J.P. Rothstein, *A novel and inexpensive technique for creating superhydrophobic surfaces using Teflon and sandpaper.* Journal of Physics D: Applied Physics, 2010. **43**(4): p. 045301.

128. Ibekwe, A., Y. Tanino, and D. Pokrajac, *A Low-Cost, Non-hazardous Protocol for Surface Texturing of Glass Particles.* Tribology Letters, 2019. **67**(4): p. 115.

129. Kubiak, K., et al., *Wettability versus roughness of engineering surfaces.* 2011. **271**(3-4): p. 523-528.

130. de Moura, L.F., R.E.J.W.S. Hernández, and Technology, *Effects of abrasive mineral, grit size and feed speed on the quality of sanded surfaces of sugar maple wood.* 2006. **40**(6): p. 517-530.

131. Regulagadda, K., S. Bakshi, and S.K. Das, *Morphology of drop impact on a superhydrophobic surface with macro-structures.* 2017. **29**(8): p. 082104.

132. Chantelot, P., et al., *Water ring-bouncing on repellent singularities.* Soft Matter, 2018. **14**: p. 2227-2233.

133. Shen, Y., et al., *Bouncing dynamics of impact droplets on the convex superhydrophobic surfaces.* Applied Physics Letters, 2017. **110**(22): p. 221601.

134. Khojasteh, D., et al., *Curvature effect on droplet impacting onto hydrophobic and superhydrophobic spheres.* 2017. **31**(6-8): p. 310-323.

135. Liu, X., et al., *Numerical research on the dynamic characteristics of a droplet impacting a hydrophobic tube.* Physics of Fluids, 2017. **29**(6): p. 062105.

136. Liu, Y., et al., *Symmetry breaking in drop bouncing on curved surfaces.* Nature Communications, 2015. **6**(1): p. 10034.

137. Moevius, L., et al., *Pancake bouncing: simulations and theory and experimental verification.* 2014. **30**(43): p. 13021-13032.

138. Bartolo, D., et al., *Bouncing or sticky droplets: Impalement transitions on superhydrophobic micropatterned surfaces.* Europhysics Letters (EPL), 2006. **74**(2): p. 299-305.

139. Hee Kwon, D. and S.J.A.P.L. Joon Lee, *Impact and wetting behaviors of impinging microdroplets on superhydrophobic textured surfaces.* 2012. **100**(17): p. 171601.

140. Reyssat, M., et al., *Bouncing transitions on microtextured materials.* Europhysics Letters (EPL), 2006. **74**(2): p. 306-312.

141. Bliznyuk, O., et al., *Scaling of anisotropic droplet shapes on chemically stripe-patterned surfaces.* 2009. **79**(4): p. 041601.

142. Kulinich, S. and M.J.L. Farzaneh, *How wetting hysteresis influences ice adhesion strength on superhydrophobic surfaces.* 2009. **25**(16): p. 8854-8856.

143. Antonini, C., F. Villa, and M. Marengo, *Oblique impacts of water drops onto hydrophobic and superhydrophobic surfaces: outcomes, timing, and rebound maps.* Experiments in Fluids, 2014. **55**(4): p. 1713.

144. Lafuma, A. and D. Quéré, *Superhydrophobic states.* Nature materials, 2003. **2**(7): p. 457-460.

145. Dorrer, C. and J.J.S.M. Rühe, *Some thoughts on superhydrophobic wetting.* 2009. **5**(1): p. 51-61.

146. Yao, X., Y. Song, and L. Jiang, *Applications of Bio-Inspired Special Wettable Surfaces.* 2011. **23**(6): p. 719-734.
147. Papadopoulos, P., et al., *How superhydrophobicity breaks down.* 2013. **110**(9): p. 3254-3258.
148. Lee, C., et al., *Two types of Cassie-to-Wenzel wetting transitions on superhydrophobic surfaces during drop impact.* 2015. **11**(23): p. 4592-4599.
149. Khojasteh, D., et al., *Droplet impact on superhydrophobic surfaces: A review of recent developments.* Journal of Industrial and Engineering Chemistry, 2016. **42**: p. 1-14.
150. Yarin, A.L., *DROP IMPACT DYNAMICS: Splashing, Spreading, Receding, Bouncing….* Annual Review of Fluid Mechanics, 2005. **38**(1): p. 159-192.
151. Richard, D. and D. Quéré, *Bouncing water drops.* Europhysics Letters (EPL), 2000. **50**(6): p. 769-775.
152. Bird, R.B.J.A.M.R., *Transport phenomena.* 2002. **55**(1): p. R1-R4.
153. Li, X., X. Ma, and Z. Lan, *Dynamic Behavior of the Water Droplet Impact on a Textured Hydrophobic/Superhydrophobic Surface: The Effect of the Remaining Liquid Film Arising on the Pillars' Tops on the Contact Time.* Langmuir, 2010. **26**(7): p. 4831-4838.
154. Reyssat, M., et al., *Dynamical superhydrophobicity.* 2010. **146**: p. 19-33.
155. Quan, Y. and L.-Z. Zhang, *Numerical and Analytical Study of The Impinging and Bouncing Phenomena of Droplets on Superhydrophobic Surfaces with Microtextured Structures.* Langmuir, 2014. **30**(39): p. 11640-11649.
156. Huang, X., K.-T. Wan, and M.E. Taslim, *Axisymmetric rim instability of water droplet impact on a super-hydrophobic surface.* Physics of Fluids, 2018. **30**(9): p. 094101.
157. Castanet, G., et al., *Transient evolution of the heat transfer and the vapor film thickness at the drop impact in the regime of film boiling.* Physics of Fluids, 2018. **30**(12): p. 122109.
158. Rioboo, R., M. Marengo, and C. Tropea, *Outcomes from a Drop Impact on Solid Surfaces.* ATOMIZATION AND SPRAYS, 2001. **11**: p. 155-166.
159. Fang, W., et al., *Revisiting the Critical Condition for the Cassie–Wenzel Transition on Micropillar-Structured Surfaces.* Langmuir, 2018. **34**(13): p. 3838-3844.
160. Shen, Y., et al., *Mechanical Equilibrium Dynamics Controlling Wetting State Transition at Low-Temperature Superhydrophobic Array-Microstructure Surfaces.* 2021. **11**(5): p. 522.
161. Cebeci, T. and F. Kafyeke, *Aircraft icing.* Annual review of fluid mechanics, 2003. **35**(1): p. 11-21.
162. Ma, L., et al., *Bio-Inspired Icephobic Coatings for Aircraft Icing Mitigation: A Critical Review.* Progress in Adhesion and Adhesives, 2021. **6**: p. 171-201.
163. Gent, R.W., N.P. Dart, and J.T. Cansdale, *Aircraft icing.* Philosophical Transactions of the Royal Society of London. Series A: Mathematical, Physical and Engineering Sciences, 2000. **358**(1776): p. 2873-2911.
164. Zarnani, A., et al., *Learning to predict ice accretion on electric power lines.* Engineering Applications of Artificial Intelligence, 2012. **25**(3): p. 609-617.
165. Bauer, D., *Snow accretion on power lines.* Atmosphere, 1973. **11**(3): p. 88-96.
166. Lv, J., et al., *Bio-inspired strategies for anti-icing.* ACS nano, 2014. **8**(4): p. 3152-3169.
167. Parent, O. and A. Ilinca, *Anti-icing and de-icing techniques for wind turbines: Critical review.* Cold regions science and technology, 2011. **65**(1): p. 88-96.
168. Carriveau, R., et al., *Ice adhesion issues in renewable energy infrastructure.* Journal of adhesion science and technology, 2012. **26**(4-5): p. 447-461.
169. Kreder, M.J., et al., *Design of anti-icing surfaces: smooth, textured or slippery?* Nature Reviews Materials, 2016. **1**(1): p. 15003.

170. Yao, X., et al., *Fluorogel Elastomers with Tunable Transparency, Elasticity, Shape-Memory, and Antifouling Properties.* Angewandte Chemie International Edition, 2014. **53**(17): p. 4418-4422.

171. Leslie, D.C., et al., *A bioinspired omniphobic surface coating on medical devices prevents thrombosis and biofouling.* Nature Biotechnology, 2014. **32**(11): p. 1134-1140.

172. Vogel, N., et al., *Transparency and damage tolerance of patternable omniphobic lubricated surfaces based on inverse colloidal monolayers.* Nature Communications, 2013. **4**(1): p. 2176.

173. Anand, S., et al., *Enhanced Condensation on Lubricant-Impregnated Nanotextured Surfaces.* ACS Nano, 2012. **6**(11): p. 10122-10129.

174. Smith, J.D., et al., *Droplet mobility on lubricant-impregnated surfaces.* Soft Matter, 2013. **9**(6): p. 1772-1780.

175. Rykaczewski, K., et al., *Dropwise condensation of low surface tension fluids on omniphobic surfaces.* Scientific reports, 2014. **4**(1): p. 1-8.

176. Xiao, R., et al., *Immersion condensation on oil-infused heterogeneous surfaces for enhanced heat transfer.* Scientific reports, 2013. **3**(1): p. 1-6.

177. Tourkine, P., M. Le Merrer, and D. Quéré, *Delayed Freezing on Water Repellent Materials.* Langmuir, 2009. **25**(13): p. 7214-7216.

178. Boinovich, L., et al., *Effect of Wettability on Sessile Drop Freezing: When Superhydrophobicity Stimulates an Extreme Freezing Delay.* Langmuir, 2014. **30**(6): p. 1659-1668.

179. Boinovich, L.B. and A.M. Emelyanenko, *Anti-icing potential of superhydrophobic coatings.* Mendeleev Communications, 2013. **1**(23): p. 3-10.

180. Boinovich, L.B., et al., *Durable Icephobic Coating for Stainless Steel.* ACS Applied Materials & Interfaces, 2013. **5**(7): p. 2549-2554.

181. Cao, L., et al., *Anti-Icing Superhydrophobic Coatings.* Langmuir, 2009. **25**(21): p. 12444-12448.

182. Mishchenko, L., et al., *Design of Ice-free Nanostructured Surfaces Based on Repulsion of Impacting Water Droplets.* ACS Nano, 2010. **4**(12): p. 7699-7707.

183. Nosonovsky, M. and V. Hejazi, *Why Superhydrophobic Surfaces Are Not Always Icephobic.* ACS Nano, 2012. **6**(10): p. 8488-8491.

184. Maitra, T., et al., *Supercooled Water Drops Impacting Superhydrophobic Textures.* Langmuir, 2014. **30**(36): p. 10855-10861.

185. Wang, Y., et al., *Verification of Icephobic/Anti-icing Properties of a Superhydrophobic Surface.* ACS Applied Materials & Interfaces, 2013. **5**(8): p. 3370-3381.

186. Heydarian, S., R. Jafari, and G. Momen, *Recent progress in the anti-icing performance of slippery liquid-infused surfaces.* Progress in Organic Coatings, 2021. **151**: p. 106096.

187. Wong, T.-S., et al., *Bioinspired self-repairing slippery surfaces with pressure-stable omniphobicity.* Nature, 2011. **477**(7365): p. 443-447.

188. Kim, P., et al., *Liquid-Infused Nanostructured Surfaces with Extreme Anti-Ice and Anti-Frost Performance.* ACS Nano, 2012. **6**(8): p. 6569-6577.

189. Wu, D., et al., *Durable deicing lubricant-infused surface with photothermally switchable hydrophobic/slippery property.* Materials & Design, 2020. **185**: p. 108236.

190. Erbil, H.Y., *Improvement of lubricant-infused surfaces for anti-icing applications.* Surface Innovations, 2016. **4**(4): p. 214-217.

191. Prakash, C.J. and R. Prasanth, *Recent trends in fabrication of Nepenthes inspired SLIPs: Design strategies for self-healing efficient anti-icing surfaces.* Surfaces and Interfaces, 2020: p. 100678.

192. Latthe, S.S., et al., *Recent developments in air-trapped superhydrophobic and liquid-infused slippery surfaces for anti-icing application.* Progress in Organic Coatings, 2019. **137**: p. 105373.

193. Wang, G. and Z. Guo, *Liquid infused surfaces with anti-icing properties.* Nanoscale, 2019. **11**(47): p. 22615-22635.

194. Villegas, M., et al., *Liquid-infused surfaces: a review of theory, design, and applications.* Acs Nano, 2019. **13**(8): p. 8517-8536.

195. Guo, P., et al., *Icephobic/Anti-Icing Properties of Micro/Nanostructured Surfaces.* Advanced Materials, 2012. **24**(19): p. 2642-2648.

196. Nine, M.J., et al., *Facile Adhesion-Tuning of Superhydrophobic Surfaces between "Lotus" and "Petal" Effect and Their Influence on Icing and Deicing Properties.* ACS Applied Materials & Interfaces, 2017. **9**(9): p. 8393-8402.

197. Hejazi, V., K. Sobolev, and M. Nosonovsky, *From superhydrophobicity to icephobicity: forces and interaction analysis.* Scientific Reports, 2013. **3**(1): p. 2194.

198. Subramanyam, S.B., K. Rykaczewski, and K.K. Varanasi, *Ice Adhesion on Lubricant-Impregnated Textured Surfaces.* Langmuir, 2013. **29**(44): p. 13414-13418.

199. He, M., et al., *Super-hydrophobic surfaces to condensed micro-droplets at temperatures below the freezing point retard ice/frost formation.* Soft Matter, 2011. **7**(8): p. 3993-4000.

200. Mei, H., et al., *Multi-level micro-/nanostructures of butterfly wings adapt at low temperature to water repellency.* Soft Matter, 2011. **7**(22): p. 10569-10573.

201. Keiser, A., et al., *Drop friction on liquid-infused materials.* Soft Matter, 2017. **13**(39): p. 6981-6987.

202. Yeong, Y.H., et al., *Oil-Infused Superhydrophobic Silicone Material for Low Ice Adhesion with Long-Term Infusion Stability.* ACS Applied Materials & Interfaces, 2016. **8**(46): p. 32050-32059.

203. Wang, N., et al., *Design and Fabrication of the Lyophobic Slippery Surface and Its Application in Anti-Icing.* The Journal of Physical Chemistry C, 2016. **120**(20): p. 11054-11059.

204. Cao, M., et al., *Water-Repellent Properties of Superhydrophobic and Lubricant-Infused "Slippery" Surfaces: A Brief Study on the Functions and Applications.* ACS Applied Materials & Interfaces, 2016. **8**(6): p. 3615-3623.

205. Yao, X., et al., *Adaptive fluid-infused porous films with tunable transparency and wettability.* Nature Materials, 2013. **12**(6): p. 529-534.

206. Schellenberger, F., et al., *Direct observation of drops on slippery lubricant-infused surfaces.* Soft Matter, 2015. **11**(38): p. 7617-7626.

207. Niemelä-Anttonen, H., *Wettability and anti-icing properties of slippery liquid infused porous surfaces*. 2015.

208. Boreyko, J.B., et al., *Air-stable droplet interface bilayers on oil-infused surfaces.* Proceedings of the National Academy of Sciences, 2014. **111**(21): p. 7588.

209. Wang, Z., L. Heng, and L. Jiang, *Effect of lubricant viscosity on the self-healing properties and electrically driven sliding of droplets on anisotropic slippery surfaces.* Journal of Materials Chemistry A, 2018. **6**(8): p. 3414-3421.

210. Shirtcliffe, N.J., et al., *An introduction to superhydrophobicity.* Advances in Colloid and Interface Science, 2010. **161**(1): p. 124-138.

211. Van Oss, C.J., *Interfacial forces in aqueous media*. 2006: CRC press.

212. Etzler, F., *Determination of the Surface Free Energy of Solids.* Rev. Adhesion and Adhesives, 2013. **1**: p. 3.

213. Good, R.J., *Contact angle, wetting, and adhesion: a critical review.* Journal of adhesion science and technology, 1992. **6**(12): p. 1269-1302.

214. Stauffer, C.E., *The Measurement of Surface Tension by the Pendant Drop Technique.* The Journal of Physical Chemistry, 1965. **69**(6): p. 1933-1938.

215. Preston, D.J., et al., *Design of Lubricant Infused Surfaces.* ACS Applied Materials & Interfaces, 2017. **9**(48): p. 42383-42392.

216. Rykaczewski, K., et al., *Mechanism of Frost Formation on Lubricant-Impregnated Surfaces.* Langmuir, 2013. **29**(17): p. 5230-5238.

CURRICULAM VITAE

Ahmed Nazrul Islam

Education:

PhD.	in Mechanical Engineering, University of Louisville, Louisville, KY.	2023
MS.	in Logistic, Trade and Transportation, University of Southern Mississippi, MS.	2017
MSc.	in Naval Architecture and Marine Engineering, University of New Orleans, LA.	2015
BSc.	in Naval Architecture and Marine Engineering, University of New Orleans, LA.	2014

Professional Career

R&D Engineer – California Lighting Technology Center – UC Davis, CA	(2022 – Present)
Simulation Engineer/ Naval Architect - C. Fly Marine Services, LA	(2013 – 2015)
Engineering Intern – M&R Global, New Orleans, LA	(2011 – 2013)

Peer-Reviewed Publications/Journal Articles:

1. **Islam**, A., & Lian, Y. (2023). Numerical Study of Drop Impact on Slippery Lubricated Surfaces. Physics of Fluids. doi:10.1063/5.0137313

2. **Islam, A.**, Sussman, M. M., Hu. H., & Lian, Y. (2022). "Simulation of Drop Impact on Substrate with Micro-wells". Physics of Fluids. doi:10.1063/5.0093826 [**Funded by NSF: Grant No. 1916114**]

3. **Islam, A.**, Taravella, B. (2022). "A Numerical Investigation of Cambered Wedge Impact Using the Lattice Boltzmann Method", Journal of the Brazilian Society of Mechanical Sciences and Engineering. doi:10.1007/s40430-022-03562-3

4. **Islam, A.**, & Taravella, B. (2021). "Design of a Depth Control Mechanism for an Anguilliform Swimming Robot". Biomimetics, 6(2), 39. doi:10.3390/biomimetics6020039 [**Funded by ONR: Grant No. N00014-11-1-0830**]

5. Faghih, M. M., **Islam, A.**, & Sharp, M. K. (2021). "On the discretization of the power-law hemolysis model". Journal of Biomechanical Engineering, 143(1), 011009. doi:10.1115/1.4048075

6. Chen, Y., **Islam, A.**, Sussman, M. M., & Lian, Y. (2020). "Numerical Investigation of Surface Curvature Effect on the Self-propelled Capability of Coalesced Drops". Physics of Fluids, 32(12). doi:10.1063/5.0026163.